Structure and Conductivity of Lithium Manganese Phosphate Glasses for Lithium Ion Batteries

by

Lei Wang

A thesis submitted in partial fulfilment of the requirements of the Degree of Doctor of Philosophy

School of Physics and Astronomy

Queen Mary University of London

United Kingdom

Supervisors: Prof. M.T. Dove and Dr. I. Abrahams

30th April 2019

Statement of originality

I, Lei Wang, confirm that the research included within this thesis is my own work or that where it has been carried out in collaboration with, or supported by others, that this is duly acknowledged below, and my contribution indicated. Previously published material is also acknowledged below.

I attest that I have exercised reasonable care to ensure that the work is original and does not to the best of my knowledge break any UK law, infringe any third party's copyright or other Intellectual Property Right, or contain any confidential material.

I accept that the College has the right to use plagiarism detection software to check the electronic version of the thesis.

I confirm that this thesis has not been previously submitted for the award of a degree by this or any other university.

Signature:

Date: 30th April 2019

Acknowledgements

I am deeply indebted to my supervisors, Prof. Martin Dove and Dr. Isaac Abrahams, for their guidance and support. I would also like to thank them for the enthusiasm they shared with me about this project, and for always finding a way to provoke in me the best of my knowledge and creativity during our numerous discussions.

I would also like to thank fellow students (present and past) for help in many ways: Ali Shehu, Guanqun Cai, Serena Maugeri, Jiaxun Liu, Ovando Carter, Ling Wang and Lei Tan.

I thank ISIS, Rutherford Appleton Laboratory for awards of beam time, and their scientist Dr Alex Hannon for his help with data collection. I also thank Dr Rory Wilson and in Queen Mary for his help with X-ray diffraction measurements.

I am very grateful to the China Scholarship Council (CSC) and Queen Mary University of London for jointly funding my PhD, and thus enlightening my life.

Finally, I would like to express my profound gratitude to my beloved parents for their moral and support and patience during my PhD study. I would also like to thank my dear wife who exceeded all bounds of kindness to me. I love all of you!!!

Abstract

The local structures and conductivities of glass samples with general compositions (50 − *x*) Li_2O: *x*MnO: 50P_2O_5 (metaphosphate glasses) and (60 − *x*) Li_2O: *x*MnO: 40P_2O_5 (polyphosphate glasses), were studied using a range of techniques including molecular dynamics (MD) simulation of neutron scattering data, a.c. impedance spectroscopy, density measurements, infrared spectroscopy, thermal analysis and X-ray diffraction.

For the first system, glasses of the selected composition (50 − *x*) Li_2O: *x*MnO: 50P_2O_5 (*x* = 10.0, 25.0, 33.3, 40.0 and 50.0) were prepared successfully. At low MnO content 50P_2O_5 (*x* = 10.0, 25.0 and 33.3), glass transition temperature increases, free volume decreases and activation energy increases, with increasing *x* value. In the compositional range $x \geq 33.3$, the glass transition temperature decreases, free volume increases and activation energy decreases, with the increasing *x*. The critical composition, *x* = 33.3, is where the structure is most compact.

Manganese cations show both network forming and network modifying behaviour in these systems. MD simulation of neutron pair distribution functions reveals two main competing phenomena: (1) increasing concentration of network forming $[MnO_2]^{2-}$ Q^4 manganate tetrahedra causes a strengthening of the network leading to higher glass transition temperatures and a more compact structure; (2) reduction in the total number of modifying cations leads to a more open structure and a reduction in cross-link density resulting in a decrease in T_g and increase in free volume.

The electrical measurement show that the charge carrier concentration is the main factor controlling the level of ionic conductivity with values in the order of 10^{-3} S cm^{-1} at 300 °C obtained in the (60 − *x*) Li_2O: *x*MnO: 40P_2O_5 system. However, this comes at the expense of a reduced ability to form glasses due to the lower phosphate content.

Table of contents

Chapter 1 Introduction

1.1 Batteries and lithium ion batteries

1.1.1 Introduction to batteries

A battery can be defined as a device that has one or more electrochemical cells that transform stored chemical energy into electrical energy via redox reactions. All batteries are composed of two electrodes, i.e. a positive terminal and a negative terminal, namely the cathode and anode respectively. These are either spatially separated or occupy the same compartment [1]. Separated electrodes are spaced by an electrolyte, a conductive material or medium. Due to the difference of chemical potentials of the two electrodes, redox reactions occur, resulting in the movement of ions through the electrolyte between them. This provokes the flow of electrons through an external circuit and this is the electrical current that can be used to power a huge range of devices.

Batteries generally can be classified into two types: primary and secondary. Primary batteries work irreversibly and cannot be recharged after the supply of reactants is exhausted. Interestingly, in some kinds of primary battery the electrodes can be replaced to allow the battery to continue to work again at the original level [2]. Secondary batteries are rechargeable, which means that, when electrical energy is provided, the chemical reaction can be reversed. This approximately restores the cell to its initial composition. Consequently, a secondary battery may be regarded as an electrochemical energy storage unit where the energy drawn from the external current is stored as chemical energy [3]. It should be noted that secondary batteries eventually dissipate the active materials and electrolyte, leading to internal corrosion. Thus, they are not indefinitely rechargeable.

From the end of the 20th century, conversion and storage of renewable energy has attracted worldwide attention due to the depletion of fossil fuel reserves and concerns over the environmental consequences of the combustion of these fossil fuels. This has led to increased effort in the development of developing high-performance batteries.

1.1.2 The role of batteries in the development of modern technology

Batteries have played a critical role in the development of modern technology. Two notable historic examples are the progression of wireless communication and electric cars (**Fig. 1.1**) [4]. In the case of the former, the first wireless device was developed in Pennsylvania in 1920 (top-right image) [4]. Roughly one century later the shrinking of batteries (along with other new technologies) has allowed modern smartphones, with various functions, to dominate the field of communication. At the beginning of the 20th century the early models of electric powered automobiles, running on lead-acid batteries, were able to reach speeds up to 30 m/s [4]. In this period - i.e. between 1900 and 1920 - the limitations in size and storage capacity of batteries caused the production of electric cars to fall from 60% of the market to 4% (data collected in America), due to their inability to keep up with driving range and speeds allowed by petrol engines. Now, 100 years later, the development of efficient battery technology has pushed fully electric cars towards the speed and driving range of traditional fossil fuelled vehicles, and in some cases, beyond. The Tesla Roadster can be taken as an excellent and topical example. Thus, the public appeal and commercialisation of fully electric cars is beginning to grow.

At the present time, a particular interest is the development of advanced, lithium ion rechargeable batteries that can support systems with higher voltage and energy densities [3,5]. Currently low-impedance lithium ion batteries (also referred to as Li-ion batteries or LIBs) are common in consumer electronic devices, for example mobile phones and laptop computers. Additionally, they are widely applied in electric vehicles, and even used in military-grade devices and weaponry. In lithium ion batteries, charged particles (lithium ions) transport from the anode to the cathode during charging and this process reverses when discharging. Rechargeable LIBs can convert and store renewable energy extremely well, as the result of their properties. Lithium (group one in the periodic table of the elements) is the lightest metallic element (atomic number 3), with only one valence electron, and its atomic mass, of only 6.941 g/mole, allows it to achieve very low density. Its thermodynamic potential and high specific capacity (3.86 A h/g and 7.23 A h/cm^3) make lithium an appealing anode material [3]. Furthermore, it may form a passivating layer that prevents chemical corrosion [3]. These properties give lithium ion batteries advantages, such as high conductivity, longevity, high energy density and excellent storage of charge.

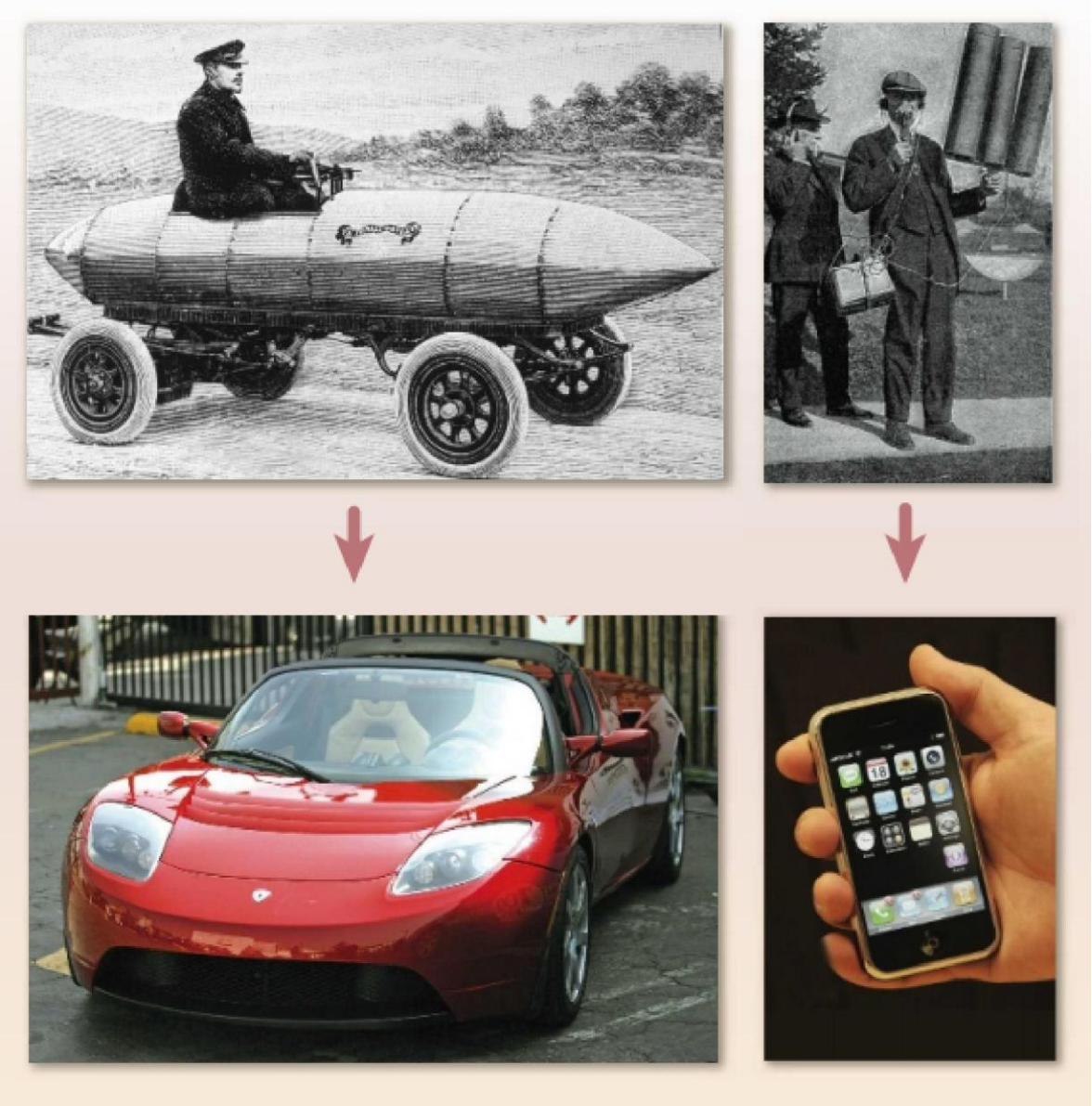

Fig. 1.1 Developments in electric cars and wireless communication in the past century [4].

1.1.3 Types of lithium ion batteries

There are different types of LIBs which have differences in their characteristics regarding aspects such as safety, chemistry, cost, and performance. Nowadays, the prevalent electrode material is $LiCoO_2$ (lithium cobaltate) which was commercialised by Sony in 1992 [6]. While it has a high energy density, it is expensive and presents safety risks when damaged. The most widely known safety problem caused in LIBs is from dendrite formation at the electrode-

electrolyte interface during cycling. These dendrites can penetrate the separator leading to short-circuits and in the case of flammable electrolytes can lead to fire. A well-known case is that of the Samsung Galaxy Note 7s mobile phones, which had to be withdrawn following safety concerns in 2016 [7]. In addition, there are concerns over the toxicity of cobalt and its cost due to its relatively small worldwide abundance. Much work has been carried out to address these issues including the development of alternatives to $LiCoO_2$, that have higher capacity, are safer, and cheaper [6,8,9]. For some alternative materials such as lithium nickel manganese cobalt oxide (NMC), lithium iron phosphate, and lithium manganese oxide (LMO), the energy density is relatively low in comparison to $LiCoO_2$. However, safety as well as longer battery life makes them highly attractive, and allows them to be possible candidates to replace $LiCoO_2$. Lithium iron phosphate ($LiFePO_4$) has a high lithium intercalation voltage (~3.5 V relative to lithium metal) and a high theoretical capacity (170 mA h g^{-1}). It also has advantages of ease of synthesis, low cost, safety, and stability when used with common organic electrolyte systems [10,11].

One advantage of lithium transition metal phosphate-based batteries lies in the strong binding force of the P−O bond. This is the strongest of the typical glass-forming cations (Si^{4+}, B^{3+} and P^{5+}) [12,13]. This contributes to the chemical stability of these materials and other advantages include their relatively low cost and high capacity. Tremendous interest has been shown in lithium transition metal phosphates (as well as related compounds) due to the framework that can reversibly intercalate/deintercalate interstitial lithium ions. The tetrahedral phosphate groups have an inductive effect when used in batteries, and this effect contributes towards a higher lithium ion conductivity, and higher working voltage in lithium ion phosphate batteries, when compared to those based on traditional oxides. The tetrahedral phosphate groups decrease the covalency of the Me−O bond, decreasing the potential of Me^n/Me^{n-1} pair with respect to Li^+/Li^0 [14]. Thus, lithium transition metal phosphate batteries display better thermal stability, long-term cycling, high energy density and electrochemical stability (essentially no loss of oxygen from the framework or reactivity with the electrolyte). Unfortunately, it is generally accepted [15-18] that lithium transition metal phosphate compounds have relatively low electronic conductivity, which makes them ideally suitable for solid electrolytes, but not for applications as electrodes. Many previous studies of these compositions reveal that they are unable to achieve an appreciable electronic conductivity (>10^{-6} S cm^{-1}) at room temperature. In the case of the application as electrodes, Tarascon et al. [15] comments in a review that “one of the main drawbacks with using these materials is their poor electronic

conductivity, and this limitation had to be overcome through various materials processing approaches…" Indeed, there are some effective methods to improve their electronic conductivities. For example, it is reported by Chung *et al.* [19] that the electronic conductivity of $LiFePO_4$ can be raised by a factor of more than 10^8 relative to the pure end member, by selective doping with some cations. In $LiMPO_4$ compositions (where M is a transition metal, such as Fe, Cu, Mn etc.), electrons are provided by M when these materials present electronic conductivity. Increasing the percentage of M or doping with some other effective cations can improve the electronic conductivity. However, both approaches reduce the amount of Li^+ ions (to maintain electroneutrality), which decreases the ionic conductivity as a result. Thus, when introducing electronic conductivity to the $LiMPO_4$ system, the ratio of Li^+ ions to cations (M) must be taken into consideration.

Some other disadvantages of traditional LIBs include interfacial and grain boundary resistances which lead to reductions in conductivity. Passivation, or corrosion can lead to increases in interfacial resistance. Birke *et al* [20] proposed a design of a monolithic all solid-state glass lithium battery to overcome some of the problems associated with conventional LIBs. In their system, the electrolyte is solid. Its simple design provides a natural seal, resistance to shocks and vibrations, solves the problems of liquid seals and prevents passivation or corrosion. Although glass is structurally disordered, glass materials can possess higher ionic conductivity when compared to crystalline materials. In such batteries, the electrodes and electrolyte are composed of a common network that enables lithium ions to transfer continually. When compared to a crystalline system, the glass system has no grain boundaries and higher isotropic conductivity. This allows for easier ion movement and higher conductivity through the battery.

1.1.4 Electrochemistry of lithium ion batteries

Electrochemical reactions in LIBs happen in all three components: aqueous or solid lithium ion conducting electrolyte; the anode; and cathode [3]. Oxidation happens at the anode and reduction takes place at the cathode [1]. The anode acts as a reducing agent, transferring electrons to the external circuit and lithium ions to the electrolyte. The cathode acts as an oxidising agent, it accepts electrons and lithium ions, from the external circuit and the electrolyte respectively [3]. Typically, the cathode consists of a transition metal oxide which is reduced during discharge and oxidised during recharge. Lithium ions can move in and out of

both electrodes during the reaction. These processes are insertion (or intercalation) and extraction (or deintercalation). An intercalation or insertion host, in the form of A_zB_y, captures lithium ions in a reversible lithium battery. Suitable materials for this type of host usually have rigid lattices, with a layer of open structure to allow insertion (or extraction) of lithium ions. These lattices can accept (or eject) compensating electrons into (or from) their electronic bands [3].

A series of intercalation/extraction reactions occur at the electrodes to create positive/negative charges [21]. As a result, the electrical energy from the power supply at the electrodes is converted into stored chemical energy and the battery charges. **Fig 1.2** illustrates this mechanism of discharge and charge in a lithium ion battery.

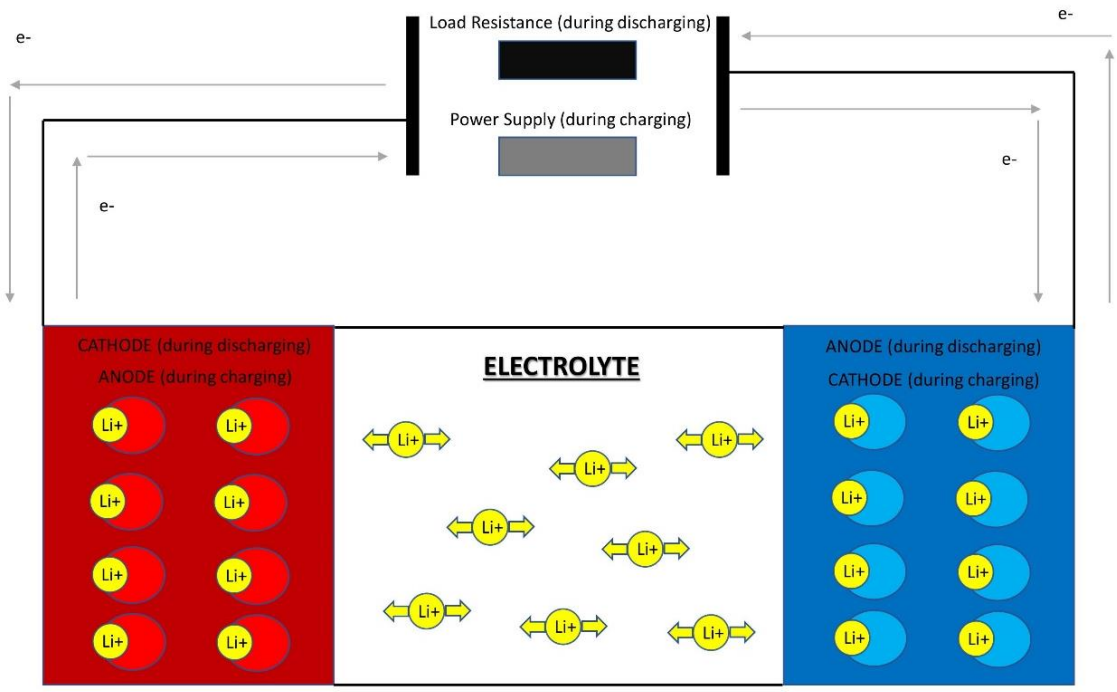

Fig. 1.2 Charge and discharge processes in an LIB.

A typical anode material is lithium intercalated graphite, on discharge Li^+ ions and electrons are created through oxidation:

$$Li_xC \rightarrow xLi^+ + xe^- + C \qquad (1.1)$$

while the cathode is typically a transition metal oxide such as $LiCoO_2$ where reduction can occur through acceptance of Li^+ ions and electrons:

$$Li_{1-x}CoO_2 + xLi^+ + xe^- \rightarrow LiCoO_2 \quad (1.2)$$

For a cell based on these electrodes, the total discharge reaction is given by:

$$Li_xC + Li_{1-x}CoO_2 \rightarrow LiCoO_2 + C \quad (1.3)$$

On charging, the reverse reactions occur:

$$\text{Anode: } LiCoO_2 \rightarrow Li_{1-x}CoO_2 + xLi^+ + xe^- \quad (1.4)$$

$$\text{Cathode: } xLi^+ + xe^- + C \rightarrow Li_xC \quad (1.5)$$

The total redox reaction for charging in lithium ion battery is:

$$LiCoO_2 + C \rightarrow Li_xC + Li_{1-x}CoO_2 \quad (1.6)$$

Over-discharging and overcharging in lithium ion batteries can occur. Over-discharging can possibly lead to an irreversible chemical reaction which produces lithium oxide [16]:

$$Li^+ + e^- + LiCoO_2 \rightarrow Li_2O + CoO \quad (1.7)$$

Similarly, overcharging can lead to the production of cobalt (IV) oxide, which can be observed by x-ray diffraction [22]:

$$LiCoO_2 \rightarrow Li^+ + CoO_2 + e^- \quad (1.8)$$

In addition to ion transport in LIBs, electronic movement is essential in the cathode and anode as mentioned in **Section 1.1.3**. Obviously, cations and electrons transport in opposite directions. Mixed electronic-ionic conductivity is necessarily required for preservation of overall charge neutrality when batteries are in operation, and importantly the chemical (ambipolar) diffusion coefficient is rate-limited by the slower species [19].

1.2 Glass

1.2.1 Introduction to glasses

To get a better understanding of the term “glass”, we should begin with an understanding of the word “amorphous”. The term “amorphous” refers to a structure without long-range order. This type of structure may still have some short-range order, which is very

similar to that in related crystalline phases. A common way to produce amorphous material is to quickly quench liquid, where the atoms do not have time to organise themselves into a crystal lattice. Thus, amorphous materials can be defined as materials without the long-range periodic character of a crystal [23]. The terms non-crystalline and amorphous can be used interchangeably because they are synonyms according to this definition.

There are several definitions for the term "glass" which is a type of amorphous material. A useful definition among them is that "a glass is an amorphous solid which exhibits a glass transition" [23]. At the glass transition there is a discontinuity in thermodynamic properties such as thermal expansion and heat capacity, and a change from liquid like behaviour to solid-like behaviour [23].

1.2.2 Structures of glasses

The atoms in a glass are linked in a three-dimensional network. However, this network is not a periodic one but exhibits short-range order, which occurs due to the atoms being arranged in regular polyhedral structures. Although the units of local structure in the glass and in the crystal may be very similar, glasses, unlike crystals, do not possess sharp X-ray diffraction patterns. In crystals, the structural units are put together as a regular lattice. However, the existence of sufficient flexibility and distortion of bond angles in a glass results in structural units can be arranged in a non-periodic way to form a random network [24].

In crystalline materials (**Fig 1.3**), atoms and/or ions are arranged and located regularly and consistently in the crystalline structure. Once the crystalline structure is defined, each location can be exactly specified, with a far more continuous pattern than will be demonstrated by a glass structure. In contrast, glasses do not possess this long-range order, which means the positions of atoms or ions are not specifically defined in three-dimensional space (**Fig 1.3**). Although the long-range structure is disordered, there are many similarities to crystalline phases, and they share the same regular polyhedra. In other words, most glasses possess a continuous random network.

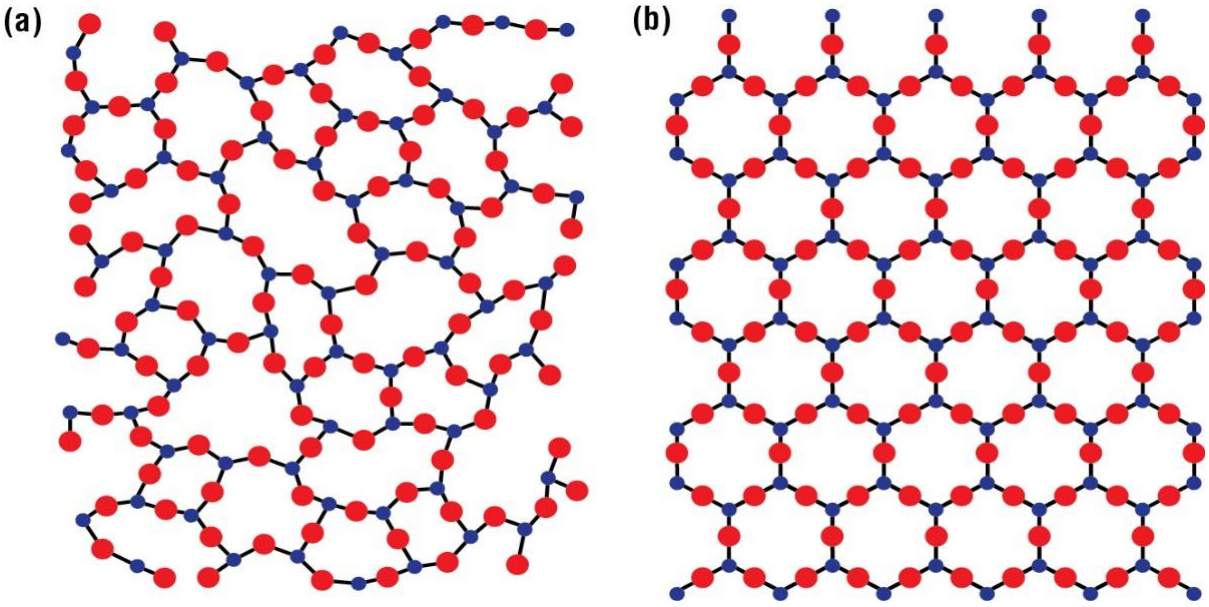

Fig. 1.3 Schematic illustration of (a) a glass with no long-range periodicity and (b) a crystalline material with a periodic network [24].

It is inappropriate to describe glass materials in the same ways used to describe crystals, such as using phrases like lattice, unit cell and lattice parameters, atomic coordinates and symmetry. In this case, Pair Distribution Functions (PDFs) are used as a common method to describe pair correlations as a function of distance [25].

Certain polyhedra are more likely to form the disordered networks of glasses. In silicates and phosphates, glasses and crystals have the same building blocks (cation polyhedra) arranged in different patterns. While the bond angles between polyhedra are well defined in crystals, glasses have broader distributions of bond angles [26].

1.2.3 Network formers, modifiers and intermediates

Zachariasen [26] proposed certain conditions for the formation of oxide glass-structures, these including the following requirements (empirical observations for oxides):

1. No oxygen atom may be linked to more than two cations.
2. The cation coordination number is small: three, four or six.
3. Oxygen polyhedra must share corners, not edges or faces. This would impose greater order.

4. 3D networks, at least three corners must be shared

Zachariasen suggested that for consistent glass formation all four rules should be obeyed. The rules mean that certain oxides such as SiO_2, B_2O_3, GeO_2 and P_2O_5 readily form glasses and others such as MgO, Al_2O_3, Na_2O, CaO do not.

Oxides such as SiO_2 and P_2O_5 which form individual glasses are labelled as "network formers". In these oxides, chemical bonds have a bond energy greater than 334.7 kJ/mole. Aliovalent network formers are connected in different ways to form network structures in glasses. B (boron) has a valence electron configuration of $2s^2\ 2p^1$. All three valence electrons are involved directly in bonding such as in BCl_3, which means each boron atom has three bonds connected to other atoms. In borate glasses, the network former (B_2O_3) consists of corner-sharing BO_3 triangles connected by bridging oxygens which form boroxol rings which is the basic structural unit in boric oxide glass (see **Fig. 1.4**). When network modifiers are introduced, boron may be hybridised in an sp^3 fashion to generate borate tetrahedra. In SiO_2 (silica glass), like other network formers from group IV, each Si (silicon) atom is connected to four oxygen atoms, since the valence electron configuration $3s^2\ 3p^2$ of Si generates four equivalent bonds via sp^3 hybridization. In silica glasses, the network predominantly is made of corner-sharing SiO_4 tetrahedra interconnected by bridging oxygen (**Fig. 1.4**). P_2O_5 (phosphate glass) is a typical network former from group V in the periodic table, which is characterised by a rigid network formed from PO_4 tetrahedra. The valence electron configuration of P (phosphorus) is $3s^2\ 3p^3$. In some cases, all five valence electrons directly contribute to σ-bonds as in PCl_5, while phosphorus also exhibits the lone pair effect to form trivalent species such as PPh_3 and PCl_3. In phosphate glasses, the P atoms are sp^3 hybridised to give PO_4 tetrahedra, three of the bonds may be considered to be single σ-bonds and the fourth a double π-bond. In reality crystal structures containing the orthophosphate anion PO_4^{3-} show the bonds to have equal lengths indicating the π-bond is delocalised over the anion. In vitreous P_2O_5 three of the oxygen atoms bridge P atoms, and the fourth oxygen atom forms a double bond with the P atom and is non-bridging, or terminal. When network modifiers are added to P_2O_5 glass, a depolymerisation occurs leading to various phosphate species. The phosphate tetrahedra are connected to each other through corner sharing (shown in **Fig. 1.4**). In some cases, there are two or more different glass formers in a glass network. For example, silica and boron trioxide acts as the main glass-forming constituents in borosilicate glasses, in which boroxol rings and SiO_4 tetrahedra are linked to each and share some oxygen atoms.

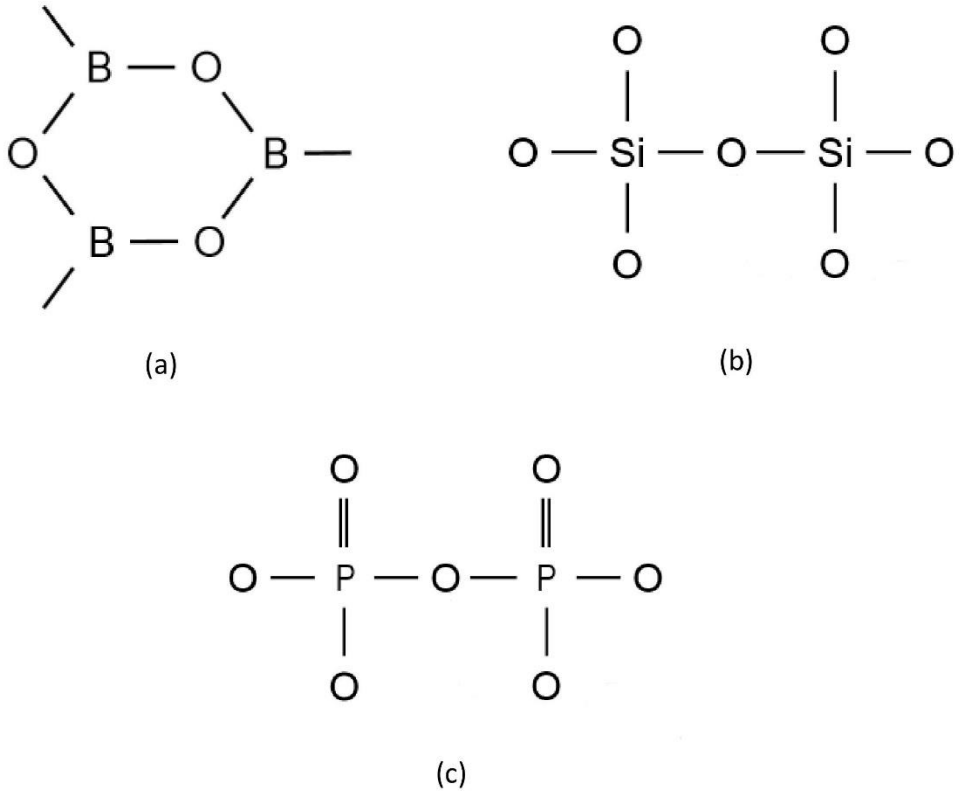

Fig. 1.4 Aliovalent network formers in different glass systems: (a) borate glass, (b) silica glass, and (c) phosphate glass.

In addition to network formers, there are some oxides which do not directly participate in formation of a structure, but instead disrupt the existing network. These are labelled as "network modifiers", and the bonds they cause are generally ionic with energy less than 251.0 kJ/mole. Typical network modifying oxides include Li_2O, Na_2O, K_2O, MgO, CaO etc.

There are three ways for network modifiers to affect an A_2O_3 type glass network formation:

1. Breaking up oxygen bridges between structure units such as A-O-A bonds and create non-bridging oxygen atoms.
2. Increasing the oxygen coordination of cation A.
3. A combination of both.

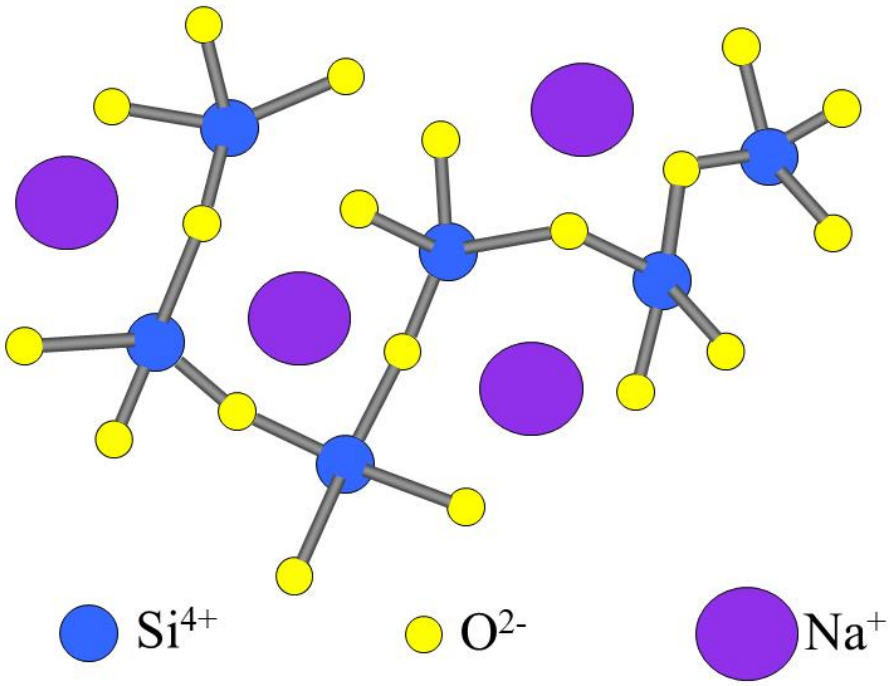

Fig. 1.5 SiO_2 glass system with added sodium as a network modifier.

An example structure of SiO_2 modified with Na_2O is shown in **Fig. 1.5**. It is worth mentioning that some network modifying oxides can change the number of oxygen atoms directly linked to the network forming atoms, For example when Na_2O is added to B_2O_3 glass (**Fig. 1.6**), the trigonal T^3 species are converted to tetrahedral Q^4 species (where T^n and Q^n represent tertiary and quaternary species, respectively and *n* is the number of bridging oxygen atoms)**.**

A third type of oxide commonly found in glasses are known as "network intermediates" or "conditional glass formers", which have a bond energy between 251.0 to 334.7 kJ/mol. The network intermediates (conditional glass formers) cannot be used to form glasses directly and individually from other elements. Instead, they can act as glass formers in combination with other network formers. Meanwhile, they decrease the melting point and viscosity of melting in a similar manner to a network modifier. Examples of intermediates include TiO_2, ZnO, PbO, and Al_2O_3. **Fig. 1.7** shows Ti^{4+} acting as a network former in SiO_2.

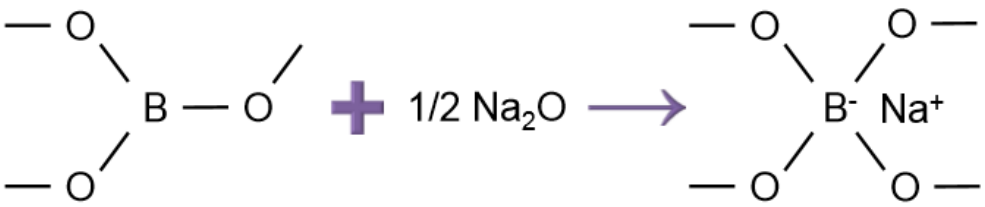

Fig. 1.6 The conversion of T^3 to Q^4 borate caused by the addition of Na_2O to B_2O_3 glass.

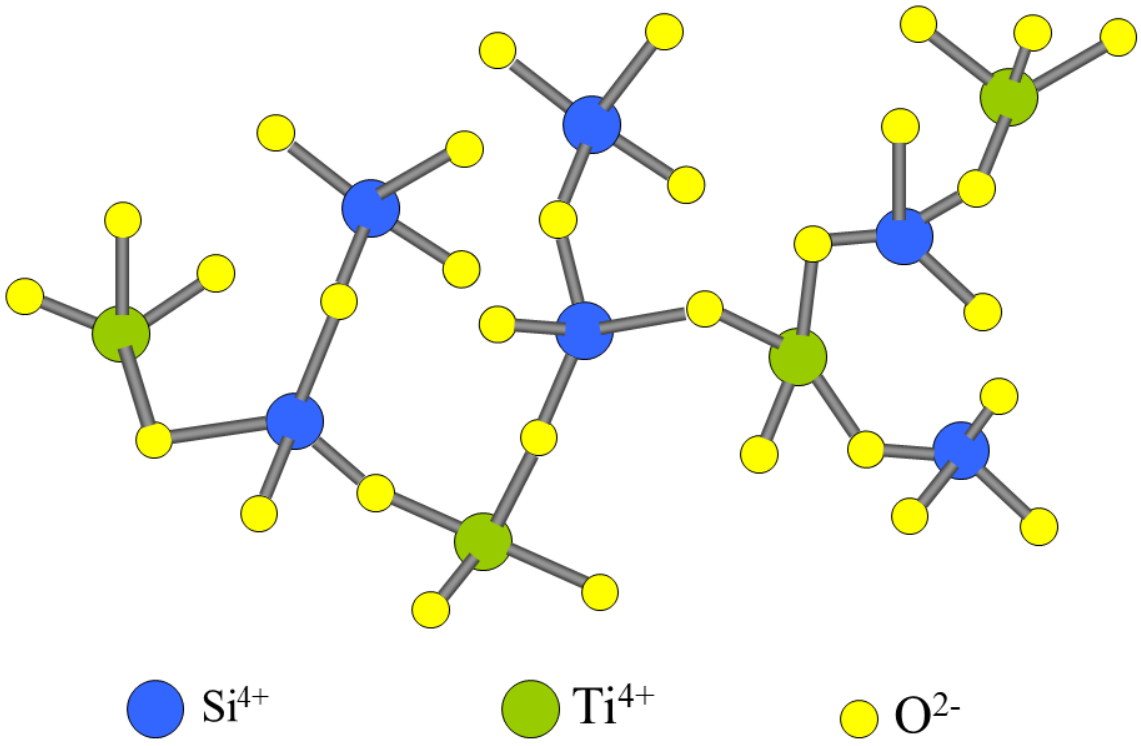

Fig 1.7 SiO_2 glass system with added titanium as a network intermediate

1.2.4 Melting, crystallisation and glass transition

The melting temperature (or melting point) can be defined as the temperature at which a substance transforms from its solid state to its liquid one at atmospheric pressure. At this

point, the solid and liquid both exist in equilibrium. When this temperature is considered as the point of the reverse change from liquid state to solid state, it is referred to as the freezing point or crystallisation point. However, since some substances can be supercooled, the freezing point is not considered as a characteristic property of a substance and certainly is not equal to the melting temperature. In fact, glasses, in contrast to crystalline solids, do not possess a melting point; when heated they undergo a smooth glass transition into a viscous liquid. Upon further heating, they gradually soften, a process which can be characterised by certain key softening points in the change in state.

Crystallisation is the process of formation of solid crystals, in which substances are precipitated from a solution, the liquid state of a melted solid, or more rarely, are deposited directly from a gas. The crystallisation process can be divided into two major parts: nucleation, and crystal growth. Nucleation is the step in which the solute molecules dispersed in the solvent gather into clusters on the nanometre scale, which causes an elevated solute concentration in a small region. These stable clusters constitute the nuclei. To become stable nuclei, the clusters need to reach a critical size which is dictated by the operating conditions (temperature, supersaturation, etc.) or the nucleus will dissolve quickly, and the crystal will not grow. The crystal growth is the subsequent growth of the nuclei that succeed in achieving the critical cluster size.

Fig. 1.8 shows the variation of volume as a function of temperature on cooling a liquid. Lowering the temperature will initially cause contraction of the liquid and once the temperature reaches the point of solidification (or freezing) T_f, if the liquid crystallises, a discontinuous change in volume is introduced in the curve. In this case, the solidification temperature at the discontinuity point is called the crystallisation temperature. As the temperature decreases further contraction will continue. However, the slope of the curve becomes more gradual than that of the original liquid.

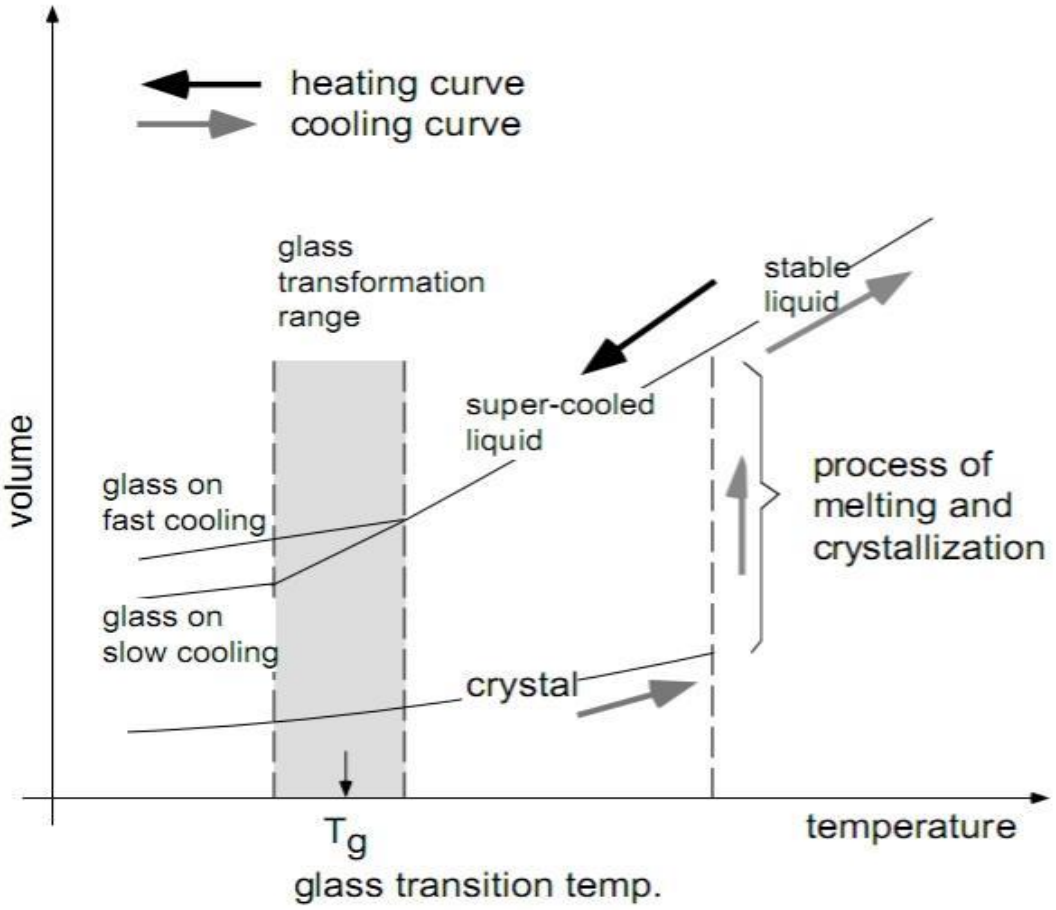

Fig. 1.8 Volume changes associated glass formation [27].

The manufacturing process of glasses requires that the raw materials be heated to a temperature sufficient to produce a fused melt and then be cooled in a special way. Vitrification, an artificial cooling method, is the supercooling of a viscous liquid to form the glass state. This process occurs when the liquid is rapidly cooled, such that there is insufficient time for the atoms to align into a crystal structure [27], because the rate of cooling of the melt is faster than the rate of crystallisation.

To understand glass formation, the term glass transition should be explained accurately. The process of glass transition involves the transformation of an amorphous materials between a hard state and a molten state [28]. In addition, it is necessary to consider a thermodynamic variable, for example, the specific volume, *V* as a function of temperature, in order to study the process with greater accuracy.

As shown in **Fig. 1.8**, considering a liquid heated and kept at a relatively high temperature, contraction will initially occur when the temperature drops. As the temperature decreases, the viscosity of the liquid continuously increases resulting in progressive freezing to its final solidification point T_f. Two phenomena may happen. As mentioned above, the liquid can crystallise. Alternatively, a second phenomenon could occur, where crystallisation does not happen and the liquid passes to a supercooled state. The point representing the supercooled state follows an extension of the liquid curve, which passes the point T_f without discontinuity [29]. From **Fig. 1.8**, we can see that the temperature decreases initially resulting in a contraction of the supercooled liquid, with a coefficient that is the same as that of the original liquid. A change in slope of the curve starts at a certain temperature T_g (glass transition temperature) and the volume decreases to a value that is closer to that of the crystalline solid. This break observed in the cooling curve represents the transformation from a supercooled liquid to a rigid, amorphous glass [29].

However, the position of T_g is not constant even under constant pressure. Instead, the time scale of the experiment plays an essential role in the glass transition process. In other words, the experimental value obtained for T_g varies with the cooling rate of the liquid. As shown in **Fig. 1.8**, a higher cooling rate results in a shift of T_g to higher temperature, whereas a slower cooling rate moves T_g towards lower temperatures. Because of this instability, the concept of a transition interval or a transformation interval [T_g] is used to describe the glass transition. The value of the upper limit of the transformation interval [T_g] is decided by the highest possible cooling rate in forming glass, while the lower limit is defined by the lowest cooling rates.

1.3 The chemistry of vitreous phosphates

1.3.1 Phosphate tetrahedra

Inorganic phosphates play an essential role in higher life forms as the main inorganic components of bone and are widely used artificially both industrially and in agriculture. Complex polymeric phosphates are fundamental components in glasses, synthetic ceramics and glass ceramics. The basic unit of phosphates is the phosphate-tetrahedron where one phosphorus atom is bonded to four oxygen atoms. In glasses these are linked by covalent oxygen atoms to form a network. Oxygen atoms, called bridging oxygens (BOs), act as connections between the individual structural units. A phosphate tetrahedron has maximum

connectivity index of three, i.e. there can be up to 3 BOs connecting it to other units. In amorphous P_2O_5, the maximum connectivity of phosphate tetrahedra is achieved giving an average neutral species of $PO_{2.5}$ [30]. The remaining oxygens are non-bridging oxygen atoms (NBOs). In phosphate networks the P-(BO) bond length ranges from 1.56 to 1.60 Å, while the P-(NBO) bond lengths are shorter and vary between 1.43 and 1.45 Å [31].

1.3.2 Phosphate speciation and the Q^n notation

Since degrees of polymerisation in glasses vary, it is best to describe the anionic networks through the speciation of the phosphorous atom. The terminology Q^n may be the best choice for speciation description. Here *n* indicates the number of bridging oxygen atoms per tetrahedron. There are four possible tetrahedral phosphate units for phosphorous, differentiated by the number of bridging oxygen atoms which link one tetrahedron to another [32]. These are summarised diagrammatically in **Fig. 1.9**. A cross-linked 3-dimensional network structure is achieved in a pure Q^3 system i.e. $(PO_{2.5})_m$, as in vitreous P_2O_5. The Q^2 unit defines a network in the form of polymer-like meta-phosphate chains, $(PO_3)_n^{n-}$. The pyrophosphate unit, Q^1 $(PO_{3.5})^{2-}$ is often encountered in glasses as a chain end, while the Q^0 $(PO_4)^{3-}$ unit is the isolated orthophosphate anion [28]. Thus, the oxygen-to-phosphorus ratio can be used to classify and to characterise the network structures of phosphate glasses.

Introducing network modifying oxides (e.g. M_2O) into vitreous P_2O_5, breaks bridging oxygen bonds (P-O-P) to increase the number of non-bridging oxygen atoms. These coordinate to the modifier [33,34]. As the number of tetrahedra linked through bridging oxygen atoms decreases, the oxygen-to-phosphorus ratio changes, as does Q^n.

$$2Q^n + M_2O \rightarrow 2Q^{n-1} + 2M^+ \quad (1.9)$$

The coordination of the electropositive modifying cation makes the P-(NBO) bond more ionic by increasing the charge separation between phosphorous oxygen ions [28].

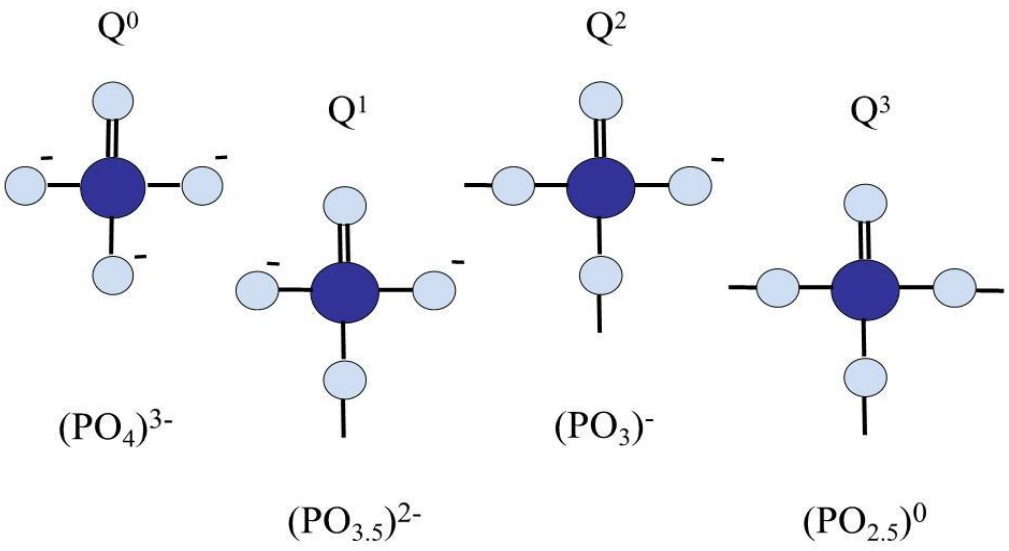

Fig. 1.9 Phosphate speciation in glasses. P and O atoms are dark and light shaded circles respectively.

1.3.3 Compositional dependence of phosphates and disproportionation

In different vitreous phosphates, the ratio of Q^n (n = 0, 1, 2, 3) varies a lot. The fraction of a particular Q^n species $f(Q^n)$ in a phosphate glass is important and is calculated from the composition and the role of all cations in the system. A glass of general composition xMO_y: P_2O_5, where M represents a network modifying cation or mixture of cations with an average charge $2y$ +, is discussed below.

There are four possible Q^n species (Q^0, Q^1, Q^2 and Q^3) and a, b, c and d are the numbers of Q^0, Q^1, Q^2 and Q^3 phosphorus atoms per formula unit, respectively. Overall electroneutrality must be maintained, so the total charge on any given anionic phosphate framework species must equal the total cationic charge:

$$2xy = 3a + 2b + c \tag{1.10}$$

The number of phosphorus atoms is 2 per formula unit:

$$2 = a + b + c + d \tag{1.11}$$

Table 1.1 Q^n fractions $f(Q^n)$, in glasses of general composition xMOy: P_2O_5

2*xy* **(**cationic or anionic charge**)**	**Q^n Species**	***f*(Q^n)**
6	Q^0	$f(Q^0) = 1$
4 – 6	$Q^0 + Q^1$	$f(Q^0) = xy - 2$, $f(Q^1) = 3 - xy$
4	Q^1	$f(Q^1) = 1$
2 – 4	$Q^1 + Q^2$	$f(Q^1) = xy - 2$, $f(Q^2) = 3 - xy$
2	Q^2	$f(Q^2) = 1$
0 – 2	$Q^2 + Q^3$	$f(Q^2) = xy - 2$, $f(Q^3) = 3 - xy$
0	Q^3	1

When just one form of possible Q^n species is present in the glass, we directly get a value of xy = 3, 2, 1 and 0 for Q^0, Q^1, Q^2 and Q^3 respectively. When xy is non-integral, the glass is predicted to contain a mixture of the two nearest Q^n species. Since there are two phosphorus atoms per formula unit formula unit, the values of $f(Q^n)$ are readily calculated by dividing the values by 2.

The $f(Q^n)$ formula given in **Table 1.1** assumes only a maximum of two types of Q^n species in a particular glass. However, occasionally more than two species occur through disproportionation of Q^n species. These require an experimentally determined degree of disproportionation.

Although the ratio of oxygen atoms to phosphorus directly determines the ratio of bridging to non-bridging oxygen atoms, some factors such as quenching rate can affect the distribution of NBOs. It is reported [35] that in polyphosphate glasses ($60Li_2O$: $40P_2O_5$), [O] / [P] > 3.0, higher quenching rate affects the arrangement of NBOs in the glass matrix, which reveals that in comparison to normally quenched samples more $(PO_4)^{3-}$ (Q^0) and $(PO_3)^-$ (Q^2) units are generated when glasses are quenched rapidly. This can be explained by the existence of an equilibrium between various phosphate units in the glass melt:

$$2(PO_{3.5})^{2-} \leftrightarrow (PO_4)^{3-} + (PO_3)^- \; (2Q^1 \leftrightarrow Q^0 + Q^2) \tag{1.12}$$

In traditional methods, the lower cooling rate provides enough time for $(PO_4)^{3-}$ (Q^0) and $(PO_3)^-$ (Q^2) units to combine and makes the equilibrium shift to the $(PO_{3.5})^{2-}$ (Q^1) side, while the higher quenching rate seems to be sufficiently rapid to freeze all the three species. Thus, an appreciable number of the species exist when the higher quenching rate method is applied, while traditionally quenched glasses consist predominantly of $(PO_{3.5})^{2-}$ (Q^1) units.

Similar disproportionation processes can occur with other phosphate species so that generally:

$$2Q^n \leftrightarrow Q^{n-1} + Q^{n+1} \tag{1.13}$$

Thus, although Q-speciation can be approximately calculated through a mathematical method, quenching rate can have an influence on the distribution of non-bridging oxygens so that other Q-species may form. Higher quenching rates can cause a disproportionation to convert a part of predominant Q^n to Q^{n-1} and Q^{n+1} species.

1.3.4 Networks modifiers and intermediates introduced to phosphate glasses

Network modifiers change various properties related to the transformation of the glass structure when introduced into a phosphate glass. Considering the addition of Li_2O to P_2O_5, the network modifiers alter the structure of the phosphate glass to change the glass transition temperature, T_g [36]. The T_g of vitreous Li_2O-P_2O_5 decreases from 635 K [37] to about 505 K after addition of 10 mole% of Li_2O. The decreasing trend in T_g continues with the addition of Li_2O until concentration reaches 20 mole%. However, further addition of Li_2O results in an increase in T_g, although the fraction of NBOs also increases. The only explanation is that a greater concentration of Li_2O increases the entanglement of long chains. This transforms a 3-dimensional network of interconnected Q^3 groups within P_2O_5 to a 1-dimensional chain [28].

Network intermediates can also be incorporated into phosphate glass to improve their physical and chemical properties. An illustrative example of how intermediates affect the structure is the addition of Al_2O_3 to alkali metaphosphate glasses which results in increased chemical durability and glass transition temperature [38]. This is because, at high concentrations, $Al(OP)_4$ and $Al(OP)_5$ become more important, which contribute to cross-linking of phosphate chains.

1.4 Ionic conduction in crystalline solids and glasses

1.4.1 Nernst-Einstein relation

High concentration, high diffusivity and high mobility of charge carriers are the main requirements for high ionic conductivity in solids. Experiments on ion migration in solids with and without the application of an external electric field, concluded that there was no difference between ion migration caused by an electric field and that caused by diffusion due to concentration gradients [39]. The diffusion coefficient D is used to characterise ion transport due to the presence of a concentration gradient, while transport of ions caused by an electric field is characterised by the overall drift or unidirectional mobility μ. The Einstein equation presents the relationship between these two parameters [39-42].

$$D = \mu k_B T \tag{1.14}$$

where k_B is the Boltzmann constant and T is absolute temperature. When a charged particle is placed in a uniform electric field **E**, it will be accelerated to a constant drift velocity $\boldsymbol{v}_d$ which is related to the drift mobility μ through the equation:

$$\boldsymbol{v}_d = q\mu\mathbf{E} \tag{1.15}$$

where q is the ion charge. Fick's flux law of migrating ions can be applied to both ion migration due to concentration gradients and that due to an electric field, generating two separate equations:

$$\mathbf{J} = -D\boldsymbol{\nabla}c \tag{1.16}$$

$$\mathbf{J} = -D\boldsymbol{\nabla}c + cq\mu\mathbf{E} \tag{1.17}$$

where **J** is the ion flux and c is ion concentration. Through Ohm's law, the flux of migrating ions **J** is related to ion charge q, ionic conductivity σ and electric field **E**, which can be described as

$$\mathbf{J} = \sigma\mathbf{E}/q \tag{1.18}$$

If the concentration gradient is zero ($\nabla c = 0$), then combining **Eqn. 1.17** and **1.18**, the ionic conductivity is equal to:

$$\sigma = q^2 c\mu \tag{1.19}$$

From **Eqn. 1.14**, the relationship between ionic conductivity and diffusion coefficient (Nernst-Einstein relation) can be derived as

$$\sigma = q^2 cD/k_B T \tag{1.20}$$

1.4.2 Ion transport mechanism and hopping models in crystalline solids

In ionic conducting solids, a large number of low energy vacant sites, connected to each other in such a way as to create diffusive pathways for migration, is required to form a suitable structural environment for high mobility of charge carriers. Generally, a larger number of available sites than the number of charge carriers is required for high performance [43-46]. Therefore, ionic conduction needs the presence of various types of defects (vacancies and/or interstitials), which are intrinsic properties of crystalline materials. In addition, the size of charge carriers must be taken into consideration, since if ions are too large then they will be incompatible with the narrow widths of the bottlenecks. These bottlenecks are typically the face of an interstitial site formed by atoms of the immobile sublattice. For example, the triangular face to an interstitial octahedral or tetrahedral site will be formed by three atoms of the immobile sublattice.

Despite over 50 years of study, no universal theory can be successfully used to describe ionic conduction mechanisms in crystalline materials. Due to the complex nature of the non-periodic structure, it is even more difficult to resolve the conductivity behaviour of glasses satisfactorily [47].

Ionic conductivity in solid materials depends on various parameters, among which concentration, diffusivity and mobility of charge carriers are the most important. The mobility is related to the structure and depends on the level of the structural disorder caused by different types of defects. Considering the type of defects involved, five possible mechanisms are presented below for the ionic conduction process [39]:

a. Exchange Mechanism – two ions exchange sites with each other directly.

b. Ring Mechanism – three or more ions move within a ring to occupy each other's position.

c. Vacancy Mechanism – ions jump to occupy a vacant site, or vacancies move from site to site.

d. Direct Interstitial Mechanism – ion jump from one interstitial site to another.

e. Indirect Interstitial Mechanism – interstitial ions move into crystallographic lattice sites forcing the atom or ion that was there, to move into interstitial site.

Only mechanisms c to e result in long-range ion diffusion. All these defect-based mechanisms are developed on the assumption that, ion migration is realized by hopping from one available site to another, and this kind of hopping is treated as fully random without being affected by other immobile ions or existing dipoles. Based on these defect mechanisms, there are some possible models for hopping. Although the single ion hopping model is simple and ideal, it presents a valuable theoretical basis for understanding the main features of how ions migrate in solids. Some basic aspects of the model will be briefly discussed below.

As described in the single ion hopping model, successive hops between available sites allow ions to move through the solid and these motions can be characterised by the hopping frequency *f*. Hopping is a thermally activated process and associated with the thermal vibrations of atoms. Thus, the hopping frequency only depends on the absolute temperature *T* and the relation can be described by an Arrhenius type equation:

$$f = f_0 \exp(-Q_m/k_B T) \tag{1.21}$$

where f_0 is the vibrational frequency of atoms in the immobile sublattice and Q_m is the hopping activation energy. Due to the randomness of hopping, this motion leads jumping ions to perform either forward or backward jumps in the process. In addition, the probabilities of forward or backward jumps are dependent on the surrounding environment and associated energy barriers. When there is no external electrical field the probabilities are equal, whereas when an external electric field, **E**, is applied, jumps in the field direction (forward jumps) have a higher probability, i.e. the applied field reduces the activation energy in the forward direction. Therefore, the activation energy in the presence of an electric field, ***E***, can be described as:

$$E_a = Q_m - \frac{1}{2} qEl \tag{1.22}$$

where *l* is the hopping distance and E_a is activation energy. The energy barrier for backward jumps will be enhanced by the same amount and it is given by:

$$E_a = Q_m + \frac{1}{2} qEl \tag{1.23}$$

The process of ion hopping is illustratively represented in **Fig. 1.10**.

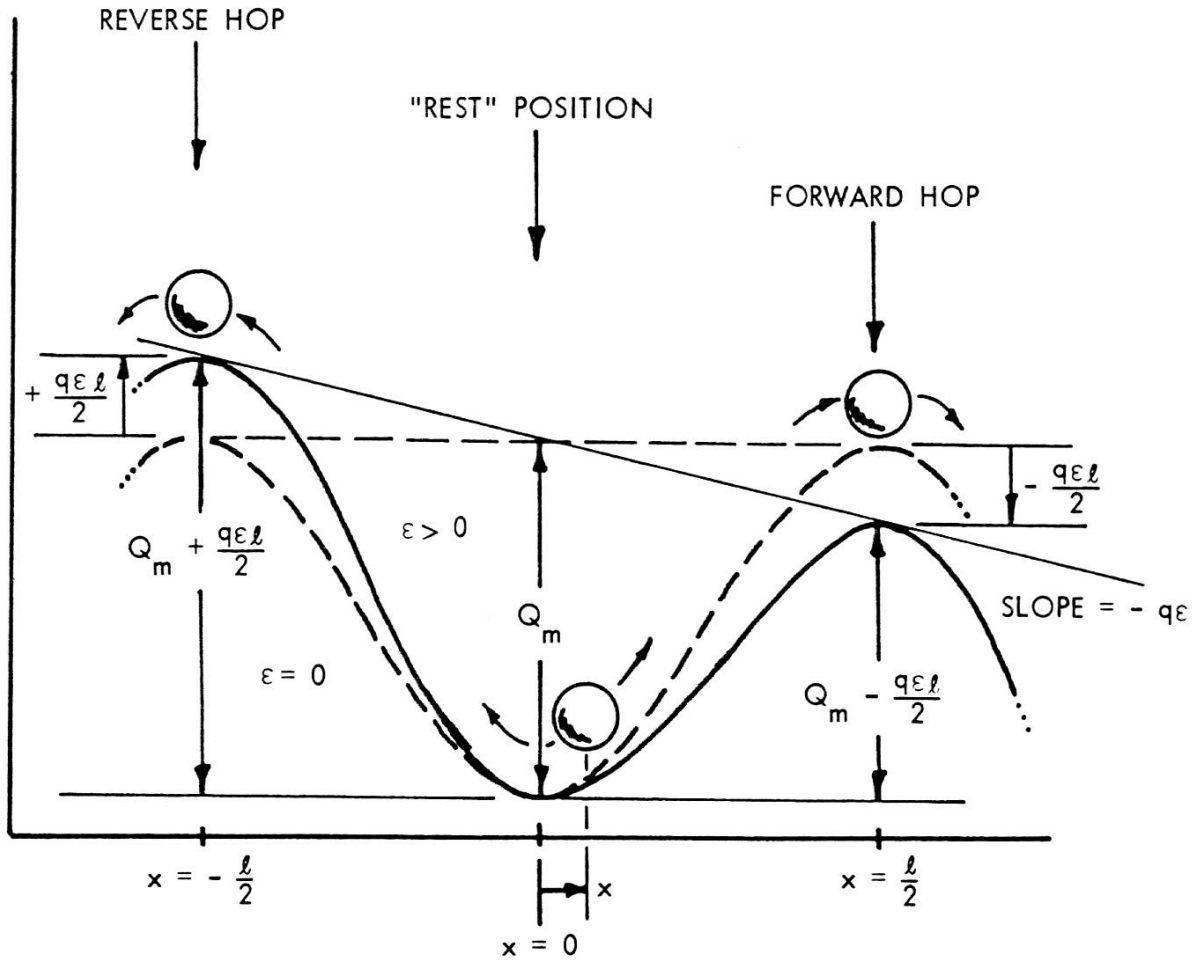

Fig. 1.10 Schematic view of the thermal energy needed for forward and backward jumps of a hopping ion from its equilibrium position, with and without applied electrical field, respectively (ε = **E)**, taken from reference [39].

There are some other more accurate models which take more factors into consideration and improve significantly the deficiencies of the single ion hoping mechanism, The Correlated Model and especially, the Cooperative Model involve interactions between all species in a solid, such as mobile ions, ions from the immobile lattice, dipoles and defects [41]. In addition, many other models of ionic conductivity (ion hopping) in solids have been proposed, such as defect cluster models and the quasi-liquid model.

1.4.3 Activation energy of conductivity in glasses

Like crystalline ion conductors, the conductivity of glasses is mainly related to temperature and concentration of charge carriers as well as many other minor factors such as ion polarizability, chemical bonding effects, ion size compared to diffusion pathway, and the size of channels in the glass network [48-50]. As in crystalline ion conductors, there is still no uniform and widely accepted theory of ion transport in glasses. Instead, a few theories have been established, such as Anderson-Stuart's strong electrolyte model. In the Anderson-Stuart model [51] it is assumed that N_i (effective carrier density of ion i) is independent of ion concentration and temperature, whereas the mobility is a quantity that depends on both parameters, ion concentration and temperature. A representation of the energetics associated with this model are shown in **Fig. 1.11**.

In the Anderson-Stuart model cations play the essential role of transporting the electrical current. To be able to do that, cations need to firstly escape from an occupied site which is next to a negative ion. Then, they jump to a new vacant space which correlates with a new negative ion. The positions of these two negative ions need to be close enough to support the movement of the cation. In phosphate glasses, where the phosphate network is negatively charged, the negative ions in the model are represented by non-bridging oxygen atoms. Together with the strain energy E_s which is associated with long range motion, the binding energy E_b contributes to the total activation energy E_a in this process:

$$E_a = E_b + E_s \tag{1.24}$$

According to Coulomb's law, with approximations, E_b can be described as

$$E_b = \frac{\beta z z_0 e^2}{\gamma(r+r_0)} \tag{1.25}$$

where z and r indicate the charge and radius of the cation, respectively, z_0 and r_0 are the charge and radius of the O^{2-} ion, respectively, γ is a covalence parameter, and β stands for a non-periodic lattice parameter which is determined by the distance between neighbouring sites. Similarly, it follows that E_s can be shown as

$$E_s = 4\pi G r_D (r - r_D)^2 \tag{1.26}$$

where r and r_D are the cation radius and the bottleneck (effective) radius respectively, and G represents the elastic modulus.

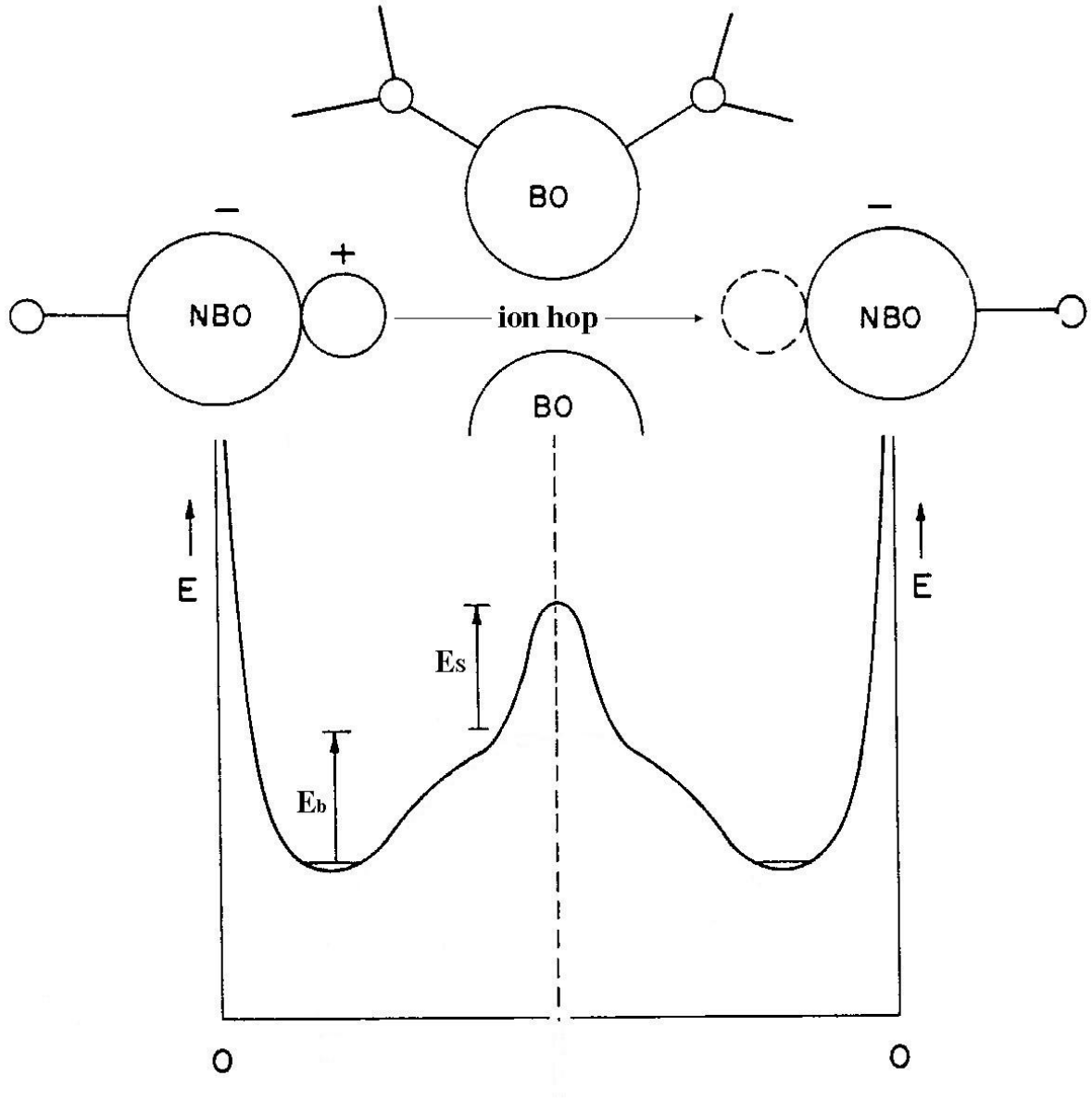

Fig. 1.11 The strong-electrolyte model showing the energetics of the cation conduction process in glasses, taken from reference [39].

After substitutions, the total activation energy E_σ can be shown to be

$$E_\sigma = \frac{\beta z z_0 e^2}{\gamma(r+r_0)} + 4\pi G r_D (r - r_D)^2 \qquad (1.27)$$

1.5 References

1 Atkins, P. W. *Physical Chemistry*. 4th edn, (Oxford University Press, 1990).

2 Pope, F. L. *Modern Practice of the Electric Telegraph*. 15th edn, (D. Van Nostrand Company, 1899).

3 Vincent, C. A. & Scrosati, B. *Modern Batteries: An Introduction to Electrochemical Power Sourses*. 2nd edn, (Antony Rowe Ltd, 1997).

4 Armand, M. & Tarascon, J.-M. Building better batteries. *Nature* **451**, 652-657 (2008).

5 Abid, M., Shaim, A. & Et-tabirou, M. Glass-forming region and electrical properties of Li_2O-PbO-P_2O_5 glasses. *Materials Research Bulletin* **36**, 2453-2461 (2001).

6 Abdel-Ghany, A., Zaghib, K., Gendron, F., Mauger, A. & Julien, C. M. Structural, magnetic and electrochemical properties of $LiNi_{0.5}Mn_{0.5}O_2$ as positive electrode for Li-ion batteries. *Electrochimica Acta* **52**, 4092-4100 (2007).

7 www.powerelectronicsnews.com.,last accessed [11 Oct 2016].

8 Jang, Y., Huang, B., Chiang, Y.-M. & Sadoway, D. Stabilization of $LiMnO_2$ in the α - $NaFeO_2$ Structure Type by $LiAlO_2$ Addition *Electrochemical and Solid-State Letters* **1**, 13-16 (1998).

9 Paulsen, J. M., Thomas, C. L. & Dahn, J. R. O2 Structure $Li_{2/3}[Ni_{1/3}Mn_{2/3}]O_2$: A New Layered Cathode Material for Rechargeable Lithium Batteries. I. Electrochemical Properties. *Journal of the Electrochemical Society* **147**, 861-868 (2000).

10 Andersson, A. S., Thomas, J. O., Kalska, B. & Häggström, L. Thermal stability of $LiFePO_4$-based cathodes. *Electrochemical and Solid-State Letters* **3**, 66–68 (2000).

11 Yamada, A., Chung, S. C. & Hinokuma, K. Optimized $LiFePO_4$ for lithium battery cathodes. *Journal of the Electrochemical Society* **148**, A224–A229 (2001).

12 Wenger, M. & Armbruster, T. Crystal chemistry of lithium: oxygen coordination and bonding. *European Journal of Mineralogy* **3**, 387-400 (1991).

13 Kanazawa, T. *Inorganic phosphate materials*. (Elsevier Science Ltd, 1989).

14 Padhi, A. K., Nanjundaswamy, K. & Goodenough, J. B. Phospho-olivines as positive-electrode materials for rechargeable lithium batteries. *Journal of the Electrochemical Society* **144**, 1188-1194 (1997).

15 Tarascon, J.-M. & Armand, M. Issues and challenges facing rechargeable lithium batteries. *Nature* **414**, 359–367 (2001).

16 Amine, K., Yasuda, H. & Yamachi, M. Olivine $LiCoPO_4$ as 4.8 V electrode material for lithium batteries. *Electrochemical and Solid-State Letters* **3**, 178–179 (2000).

17 Huang, H., Yin, S.-C. & Nazar, L. F. Approaching theoretical capacity of $LiFePO_4$ at room temperature at high rates. *Electrochemical and Solid-State Letters* **4**, A170–A172 (2001).

18 Yang, S., Song, Y., Zavalij, P. Y. & Whittingham, M. S. Reactivity, stability and electrochemical behavior of lithium iron phosphates. *Electrochemistry Communications* **4**, 239–244 (2002).

19 Chung, S.-Y., Bloking, J. T. & Chiang, Y.-M. Electronically conductive phospho-olivines as lithium storage electrodes. *Nature Materials* **4**, 123-128 (2002).

20 Birke, P., Salam, F., Doring, S. & Weppner, W. A first approach to a monolithic all solid-state inorganic lithium battery. *Solid State Ionics* **118**, 149-157 (1999).

21 Aravindan, V., Gnanaraj, J., Madhavi, S. & Liu, H.-K. Lithium-Ion Conducting Electrolyte Salts for Lithium Batteries. *Chemistry A European Journal* **17**, 14326-14346 (2011).

22 Amatucci, G., Tarascon, J. & Klein, L. CoO_2, the end member of the Li_xCoO_2 solid solution. *Journal of The Electrochemical Society* **143**, 1114-1123 (1996).

23 Elliott, S. R. *Physics of amorphous materials*. (Longman, 1983).

24 Stevens, M. P. *Polymer chemistry - an introduction*. (Oxford University Press, 1999).

25 Dove, M. T. Structure and dynamics - an atomic view of materials. *Materials Today* **6**, 59 (2003).

26 Zachariasen, W. H. The atomic arrangement in glass. *Journal of the American Chemical Society* **54**, 3841-3851 (1932).

27 Atkins, P. *Shriver & Atkins' Inorganic Chemistry* 5th edn, (Oxford University Press, 2010).

28 Abrahams, I. & Hadzifejzovic, E. Lithium ion Conductivity and thermal behaviour of glasses and crystallised glasses in the in the system Li_2O-TiO_2-Al_2O_3-P_2O_5. *Solid State Ionics* **134**, 249-257 (2000).

29 West, A. R. *Solid state chemistry and its applications*. (John Wiley & Sons, 2013).

30 Brow, R. K. Review: the structure of simple phosphate glasses. *Journal of Non-Crystalline Solids* **263**, 1-28 (2000).

31 Liang, J.-J., Cygan, R. T. & Alam, T. M. Molecular dynamics simulation of the structure and properties of lithium phosphate glasses. *Journal of Non-Crystalline Solids* **263**, 167-179 (2000).

32 Kirkpatrick, R. J. & Brow, R. K. Nuclear magnetic resonance investigation of the structures of phosphate and phosphate-containing glasses: a review. *Solid state nuclear magnetic resonance* **5**, 9-21 (1995).

33 Hoppe, U. A structural model for phosphate glasses. *Journal of non-crystalline solids* **195**, 138-147 (1996).

34 Hoppe, U., Walter, G., Kranold, R. & Stachel, D. Structural specifics of phosphate glasses probed by diffraction methods: a review. *Journal of Non-Crystalline Solids* **263**, 29-47 (2000).

35 Dabas, P., Subramanian, V. & Hariharan, K. Effect of quenching rate on the structure, ion transport, and crystallization kinetics in lithium-rich phosphate glass. *Journal of Materials Science* **49**, 134–141 (2014).

36 Hudgens, J. J. & Martin, S. W. Glass transition and infrared spectra of low-alkali, anhydrous lithium phosphate glasses. *Journal of the American Ceramic Society* **76**, 1691-1696 (1993).

37 Walter, G., J. Vogel, U. H. & Hartmann, P. The structure of CaO-Na_2O-MgO-P_2O_5 invert glass. *Journal of non-crystalline solids* **296**, 212-223 (2001).

38 Karabulut, M., Metwalli, E. & Brow, R. Structure and properties of lanthanum-aluminum-phosphate glasses. *Journal of non-crystalline solids* **283**, 211-219 (2001).

39 Tallan, N. M. *Electrical Conductivity in Ceramics and Glass*. (Marcel Dekker Incorporated, 1974).

40 Varshneya, A. K. *Fundamentals of Inorganic Glasses*. (Academic Press Incorporated, 1994).

41 Vashishta, P., Mundy, J. N. & Shenoy, G. K. *Fast Ion Transport in Solids*. (Elsevier North Holland Incorporated, 1979).

42 Soquet, J. L., Duclot, M. & Levy, M. Ionic transport mechanisms in oxide based glasses in the supercooled and glassy states. *Solid State Ionics* **105**, 237-242 (1998).

43 Cowdhari, B. V. R., Yahaya, M., Talib, I. A. & Salleh, M. M. *Proceedings of the 4th Asian Conference on Solid State Ionics*. (World Scientific Publishing Co., 1944).

44 Shriver, D. F. & Farrington, G. C. Special Report: Solid Ionic Conductors. *Chemical and Engineering News* **63**, 42-44 (1985).

45 Bruce, P. G. & Abrahams, I. A defect cluster model for ion migration in solid electrolytes. *Journal of Solid State Chemistry* **95**, 74-82 (1991).

46 West, A. R. *Basic Solid State Electrochemistry*. (John Willey & Sons Ltd, 1999).

47 Takahashi, T. Solid-state ionics-recent trends and future expectations. *Bulletin of Electrochemistry* **11**, 133 (1995).

48 Kennedy, J. Ionically conductive glasses based on SiS2. *Materials chemistry and physics* **23**, 29-50 (1989).

49 Geller, S. Crystal structure of the solid electrolyte, RbAg4I5. *Science* **157**, 310-312 (1967).

50 Minami, T. & Machida, N. Preparation of new glasses with high ionic conductivities. *Materials Science and Engineering: B* **13**, 203-208 (1992).

51 Jogad, M. S. Anderson-stuart model to analyze conductivity of fluormica glass-ceramics. *Materials Letters* **54**, 249-255 (2002).

Chapter 2 Methods

2.0 Introduction

This chapter deals with the theory and brief description of characterisation techniques used in this work and general synthetic methods.

2.1 Density measurements

All the density measurements were carried out using a gas displacement method which can measure the volume of solid objects. As shown in **Fig. 2.1**, V_{cell} and V_{exp} are the volume of the cell and of the expansion chamber respectively. The cell and expansion chamber begin at ambient pressure P_a, and ambient temperature T_a when the valve is closed. Then, the pressure of the cell is increased to an elevated pressure P_1. The mass balance equation becomes:

$$P_1(V_{cell} - V_{samp}) = n_C R T_a \tag{2.1}$$

where n_C is the number of moles of gas in the sample cell and R is the gas constant. The equation for calculating the expansion volume can be expressed as:

$$P_a V_{exp} = n_E R T_a \tag{2.2}$$

where n_E is the number of moles of gas in the expansion volume. Opening the valve decreases the pressure to P_2 and the new mass balance equation is given by:

$$P_2(V_{cell} - V_{samp} + V_{exp}) = n_c R T_a + n_E R T_a \tag{2.3}$$

After rearranging the equations above, then introducing P_a into the equation, we obtain:

$$V_{samp} = V_{cell} - \frac{V_{exp}}{\frac{P_1 - P_a}{P_2 - P_a} - 1} \tag{2.4}$$

P_{1g} and P_{2g} need to be written as gauge pressures:

$$P_{1g} = P_1 - P_a \tag{2.5}$$

$$P_{2g} = P_2 - P_a \tag{2.6}$$

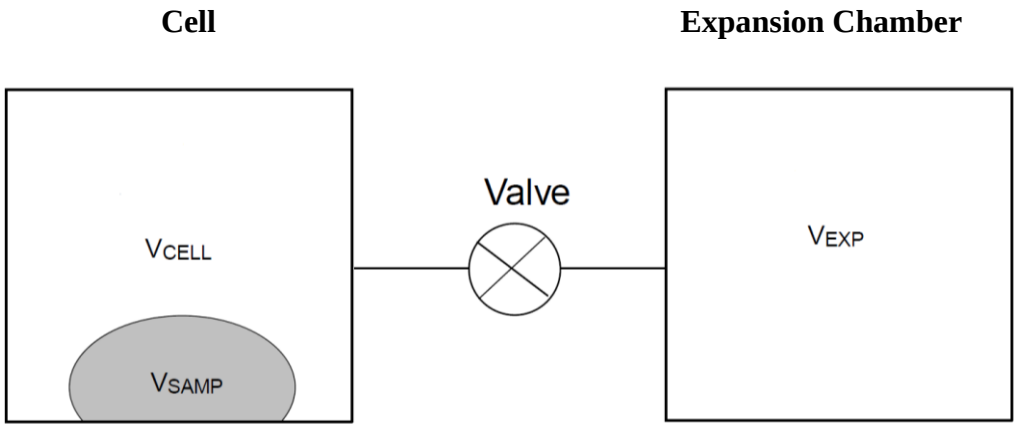

Fig. 2.1 Simplified block diagram for density measurements using gas displacement.

Finally, V_{samp} can be rewritten as:

$$V_{\text{samp}} = V_{\text{cell}} - \frac{V_{\text{exp}}}{\frac{P_{1g}}{P_{2g}} - 1} \tag{2.7}$$

The equation above provides the results of the volume of the sample. In detail, V_{cell} and V_{exp} are decided by calibration procedures and the pressures can be measured by a gauge pressure transducer. The mass measurement is achieved by using an electronic balance, and density is then calculated using *density = mass / volume*.

2.2 Thermal analysis

The most widely-used thermal analysis techniques are Differential Thermal Analysis (DTA) and Differential Scanning Calorimetry (DSC) [1,2]. Both can be used to detect the smallest temperature (heat) changes in a studied material.

The principles behind DTA are summarised as follows [3]:

1. An inert reference material is required;

2. The reference material must be stable across the entire temperature range;

3. The heating/cooling rates are equally applied to the tested sample and reference material;

4. This is performed in a strictly controlled, inert or oxidising atmosphere, e.g., N_2, Ar, He, air;

5. ΔT, the difference in temperature between the sample and reference material is measured throughout the experiment;

6. The instrument is equipped with a single heater for both the sample and reference material.

DSC shares the first four principles with DTA. However, DSC instruments require a different heating control apparatus, namely two programmable heaters, one for the sample and another for the reference material. In addition, $\Delta T = 0$ remains unchanged in DSC testing. Instead, the difference in heat flow (ΔQ) between sample material (Q_s) and reference material (Q_r) is measured in this method.

Both DTA and DSC can be applied in identical thermal cycles while recording changes of temperature. Any changes (exothermic or endothermic) are detected relative to the inert reference, which can reflect transformations, such as glass transitions, crystallisation and melting.

2.3 Infrared spectroscopy (IR)

As with many other spectral methods, infrared spectroscopy derives its information by the process of energy absorption. The bonds within each functional group either vibrate, rotate or sway in response to radiation. Infrared spectroscopy (IR) is a type of vibrational spectroscopy which deals with the infrared part of the electromagnetic spectrum [3] in the wavelength (λ) range from 0.78 μm to 1000 μm. For practical purposes, researchers divide the IR spectrum into three parts: near, mid and far. For this project the only relevant part of the spectrum will be mid-infrared (2.5 to 25 μm), which is used to study the fundamental vibrations and associated rotational-vibrational structure. For practical applications the reciprocal value of wavelength, wave number $\tilde{\nu}$ (cm^{-1}) is more widely used than the wavelength itself. The relation between wavelength and wave number is shown below:

$$\tilde{\nu} = \frac{1}{\lambda} \tag{2.8}$$

As shown in **Table 2.1**, IR features in the phosphate glasses studied in this work are in the mid-infrared region from 4000 to 400 cm^{-1} which corresponds to 2.5 to 25 μm.

Table 2.1 IR features frequently observed in phosphate glasses [4,5].

Frequency (cm^{-1})	Assignment
~ 1260	P = O vibration superposed with $(PO_2)_{as}$ mode in Q^2 units.
~ 1190	$(P—O^-)$ vibration in Q^2 units
~ 1100 to 1140	Broad band for $(P—O^-)_{as}$ vibration in Q2 units
~ 1040	Vibration of PO_4^{3-} tetrahedra
~ 970	$(P—O^-)_{as}$ vibration in Q^1 units
~ 880 to 900	$(P—O—P)_{as}$ vibration of BOs
~ 720 to 780	$(P—O—P)_s$ vibration of BOs
~ 530	Deformation mode of $P—O^-$ groups

When absorption happens, it transitions occur between vibrational and rotational energy levels. Only vibrational transitions are typically observed in solids. Vibrations can be divided into stretching and bending. Stretching vibrations can be symmetric or asymmetric, which involve changes in the inter-atomic distance along the bond. Bending vibrations relate to changes in the angle between two bonds. This includes twisting, rocking, wagging and scissoring. Functional group must undergo a change in dipole moment to be IR active. A permanent dipole is not necessary, however, a change in dipole moment is. If the frequency of the electromagnetic radiation matches the vibrational frequency of the functional group, the radiation interacts with the changing dipole moment and excites functional group to a higher energy level, changing the amplitude of vibration.

Using IR spectroscopy, we can analyse the intensities and shapes of absorption bands which occur in a relevant region, to derive some qualitative information. The mid-IR spectrum region can be divided into two parts. The first part of IR spectrum from 4000 to 1200 cm^{-1}, is always used for identification of functional groups, since their vibrations always occur in the same frequency band. The other part (referred to as the fingerprint region) of the spectrum which ranges from 1200 to 200 cm^{-1}, can be compared with standard patterns to identify unknown materials. Thus, the frequency of absorbed radiation can be associated with a bond type [6]. This contributes to a further understanding of the sample structure.

2.4 Scattering measurements

2.4.1 Bragg's law and diffraction

In 1912, von Laue, Friedrich and Knipping showed that crystalline solids could diffract incident X-rays, first demonstrating the occurrence of diffraction in crystalline structures [7]. In the next year, the Bragg father-and-son team successfully determined the crystal structure of sodium chloride by implementing this new phenomenon practically. With further studies, these finding contributed to their Nobel Prize. Nowadays, diffraction techniques have become the most commonly used methods for structural analysis of crystalline materials [8].

Diffraction can be defined as a process by which a material with a periodic internal order scatters incident radiation to cause constructive and destructive interference of the scattered radiation. It is important to mention that both X-rays, and neutrons, can be treated as forms of radiation characterised by wave-like behaviour. As shown in **Fig. 2.2**, both the angle of incidence and the angle of reflection are represented as θ (when orientated correctly, θ is called the Bragg angle). Waves are reflected from planes of atoms separated by a distance d. For diffraction to occur the wavelength of incident radiation and the distance between the scattering objects must share the same order of magnitude. Only when this is the case will the distances of each beam of the scattered radiation be equal to an integral multiple of the wavelength, $n\lambda$. It follows that,

$$n\lambda = 2d \sin\theta \tag{2.9}$$

In applications, three integers h, k, l, commonly referred to as Miller Indices, are used to define each group of parallel planes (Miller planes) [9]. d_{hkl} is the perpendicular distance between nearest neighbour (hkl) planes. For beams at certain angle of incidence, each plane possesses its own specific angle θ_{hkl}. n is usually absorbed into the (hkl) Miller plane when we simplify the equation. Bragg's law can be given as

$$\lambda = 2d_{hkl} \sin\theta_{hkl} \tag{2.10}$$

Using Miller indices, a diffraction pattern can be indexed and can be used to directly obtain the unit cell parameters.

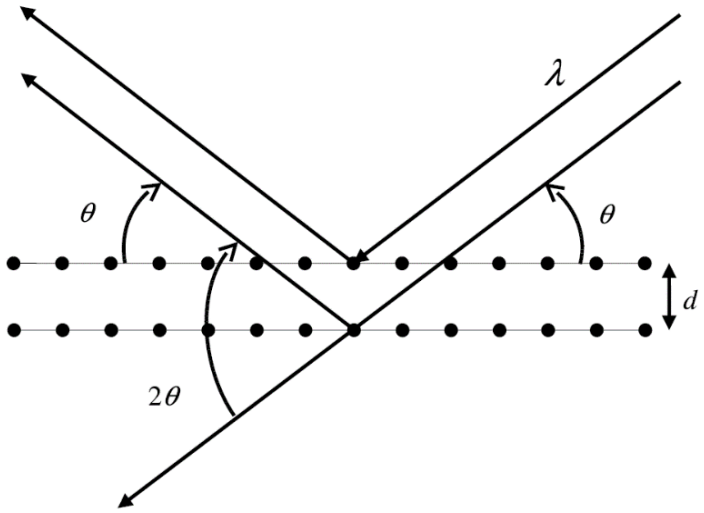

Fig. 2.2 Illustration of Bragg's law for crystal diffraction, taken from reference [10], where λ is the wavelength of the radiation, d is the distance between two atom planes and θ is the angle of incidence (and reflection). A reflection will occur if $n\lambda = 2d \sin\theta$.

2.4.2 Diffuse scattering and total scattering

2.4.2.1 Diffuse scattering

As early as 1913, Friedrich discovered that there were weak radial streaks in the pattern along the Laue spots in an X-ray experiment of KCl, representing the first observation of diffuse X-ray scattering. During the next year, Debye first started his theoretical work on this special scattering and predicted that atomic vibration was the main cause of diffuse scattering and would lead to a continuous contribution to single crystal X-ray scattering.

From diffuse scattering data, information on the deviation from the average structure can be obtained, since diffuse scattering is caused by any temporary or permanent modulation of space group symmetry. Notably, the occurrence of diffuse scattering can be anywhere in reciprocal space. Diffuse scattering often occurs as a broad undulation in diffraction patterns and its intensity is generally weak when it is compared to Bragg peaks, and as such diffuse scattering is often treated as part of the background scattering produced in crystalline systems.

2.4.2.2 Total scattering

In addition to Bragg diffraction, diffuse scattering is nowadays becoming a necessary part of research on amorphous materials and in partially disordered crystalline materials. Local disorder exists inevitably, and, in these materials, the short-range structures have different characteristics from the long-range average structure.

Total scattering, as described for example by Dove *et al.* [11], is the scattering of radiation by matter that covers most scattering vectors and includes scattering with all possible changes of energy of the radiation. In the total scattering method, lattice parameters and average positions of atoms can be obtained as well as fluctuations of the atomic arrangement from the average structure, i.e. local disorder.

In summary, total scattering contains two parts: Bragg diffraction and diffuse scattering. From the aspect of this project, the structures of studied materials were obtained mostly by using total scattering methods, including X-ray and neutron scattering.

2.4.2.3 X-ray and X-ray scattering

Nowadays X-rays are the most accessible and the most commonly used radiation for diffraction methods. In the laboratory, X-rays can be produced when a beam of electrons strikes a metal target (usually copper or molybdenum) [11]. The X-rays are generated by two different mechanisms. When the electrons enter the metal, they are rapidly decelerated, and an accelerating or decelerating charge will produce electromagnetic radiation (X-rays). This mechanism is called Bremsstrahlung. In the second mechanism, high energy electrons are accelerated towards a metal target and this process causes electrons to be ejected from one of the inner electron shells. The process of by which an electron drops from a higher to lower orbital results in the production of X-ray radiation. The generated X-rays are electromagnetic waves which possess wavelengths from 0.1 Å to 100 Å. In the case a copper target, transitions from the 2*p* to 1*s* (K_α) and 3*p* to 1*s* (K_β) orbitals generate X-ray wavelengths of 1.5418 Å and 1.392 Å, respectively. The stronger K_α peak is typically used for diffraction experiments and in fact consists of two peaks $K_{\alpha1}$ (λ = 1.54065 Å) and $K_{\alpha2}$ (λ = 1.5433 Å) due to the two possible spin transition. Since experiments are always performed using a fixed wavelength, absorbing filters are used to remove the rest of X-rays apart from that at the required

wavelength. Alternatively, a monochromator (a specially mounted crystal in the form of a flat plate) can used to diffract only the K_α (or $K_{\alpha 1}$) peak onto the sample.

X-rays of higher intensity and wider wavelength range can be utilised by using synchrotron sources [11]. In a synchrotron an electron travelling in a circular orbit accelerates in a radial direction and decelerates tangentially, which makes that the circular beam continuously lose energy as photons. The synchrotron radiation is emitted as a continuous band of X-rays wavelengths from which a monochromator can be used to select a specific wavelength for experiments.

X-rays with a wavelength of about 1 Å are suitable for diffraction methods since this wavelength is in the order of the interatomic spacing of crystals or amorphous materials. In practice, a scattering effect is a result of the interaction of X-rays with the electrons of different atoms. To be more exact, X-rays interact with the electronic density distribution around the nuclei of different atoms. Because atoms with bigger atomic number in the periodic table possess more electrons, they can have more interactions with X-rays. Therefore, the X-ray scattering power correlates directly with the number of electrons that the atoms possess. Generally, $f(Q)$ ($\mathbf{Q}$ is scattering vector and $Q = |\mathbf{Q}| = 4\pi \sin\theta/\lambda$), is used to characterise each atom [12]. In the limitation that $\mathbf{Q}$ goes to zero, where the X-rays are scattered without deflection, the scattering factor f equals the atomic number Z. In summary, the atomic number of a given element reflects the intensity of the effect on the scattered X-ray.

In 1914, Debye and Scherrer in Germany, and Hull in the United States developed the X-ray powder diffraction method independently. In this method, samples are required to be ground into powder, in which there are many randomly orientated crystallites. Thus, at least some of the crystallites can be correctly orientated to satisfy Bragg's law for each set of allowed reflections. Different solid crystalline substances possess different characteristic X-ray powder patterns and they can be used as a "fingerprint" for the identification of the crystalline solid [13].

Fig. 2.3 The PANalytical Empyrean Ag-anode X-ray diffractometer, located at Queen Mary University of London. The X-ray wavelength is λ = 0.5609 Å, the maximum diffraction angle 2θ = 156°, which corresponds to Q_{max} = 21.9 Å^{-1}.

Glasses possess an amorphous structure, in other words they contain no crystallographic planes. Thus, the X-ray diffraction patterns of glasses do not show Bragg peaks [13]. However, they do contain broad features which can be measured through the total scattering method and can be further analysed using the PDF method introduced in the following section. In the total scattering method, Ag, instead of Cu, is chosen as the anode material, thus achieving a higher Q_{max}. Ag K_α radiation has a shorter wavelength of 0.5609 Å, leading to a better resolution when compared to that of Cu. The diffractometer that used for this in the present work was a PANalytical Empyrean Ag-anode X-ray diffractometer (**Fig. 2.3**). Additionally, data with a larger Q_{max} of 40 Å^{-1}, corresponding to the wavelength of 0.1617 Å, can be collected using synchrotron X-ray radiation. The synchrotron data in this project were collected on the XPDF I51-1 diffractometer at the Diamond facility, Rutherford Appleton Laboratory.

2.4.2.4 Neutron and neutron scattering

Sir James Chadwick proved the existence of neutrons in 1932. Neutron are one kind of subatomic particle with no charge. They have a mass that is roughly equal to a proton, and neutrons have a magnetic moment caused by the combination of their constituent quarks. When travelling, a neutron shows a wave-like behaviour, which can be described by the de Broglie relation as given: $\lambda = h/mv$, where λ is the neutron wavelength, *h* and *m* are Planck's constant and the particle's rest mass, respectively, and *v* is the particle velocity [14].

Both nuclear reactors and spallation sources can be used to produce neutrons. Compared with reactor sources, pulsed or spallation neutron sources operate with less radioactive and toxic waste, which makes them safer. In the present work, neutron diffraction data were collected at the ISIS Facility, Rutherford Appleton Laboratory, UK, where neutrons are generated using a spallation source (**Fig. 2.5** and **Fig. 2.6**). In the production process (**Fig. 2.4**) protons are injected into a synchrotron ring where they are accelerated to relativistic speeds. These high energy protons (ca. 800 MeV) are periodically fired as a pulse at a heavy-metal (such as tungsten) target. This knocks out neutrons from the nucleus of the target atom. The neutron yield of this method is very high (roughly 30 neutrons per proton) [15]. After the generation of neutrons, moderators (e.g. hydrogen, methane or water) that surround the target are used to slow the neutrons, so suitable wavelengths can be obtained for related experiments. This neutron beam has a spectrum of wavelengths that is determined by the type of moderator being used. The time of flight (tof) of the neutrons from the target to the detector (via the sample) is measured and is directly proportional to the wavelength.

Over the last 40 years, neutron scattering techniques have become one of the most successful structural analysis methods and are a widely used alternative to X-rays in diffraction experiments [16]. Since neutrons are electrically neutral, compared to the charged particles with the same kinetic energy, they can penetrate much deeper into materials and interact with nuclei with strong nuclear forces. Furthermore, neutron spins may also interact with the magnetic moment of atoms originating from unpaired electrons in the outer electronic orbitals, resulting in magnetic scattering.

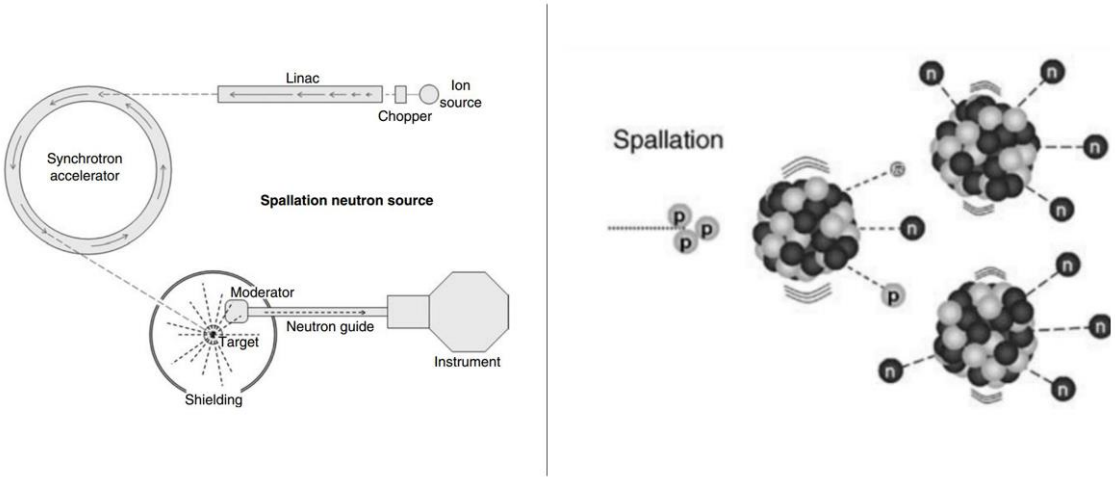

Fig. 2.4 The production process of a spallation neutron source, taken from reference [17]. A beam of protons is accelerated in a synchrotron to achieve high-energy, then it is used to bombard a heavy-metal target to produce neutrons.

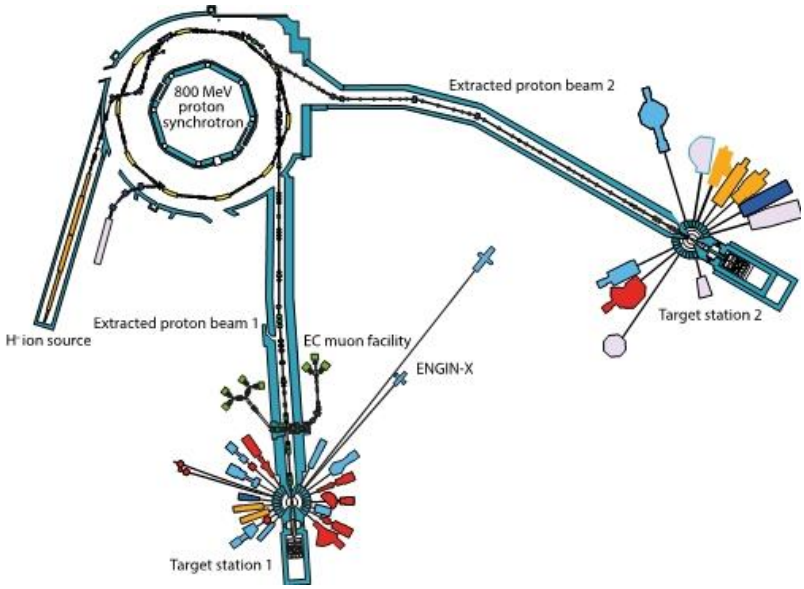

Fig. 2.5 A map of ISIS, showing the proton synchrotron and the two target stations with the beamlines (instruments) shown in different colours and departing radially from the respective target stations, taken form reference [18].

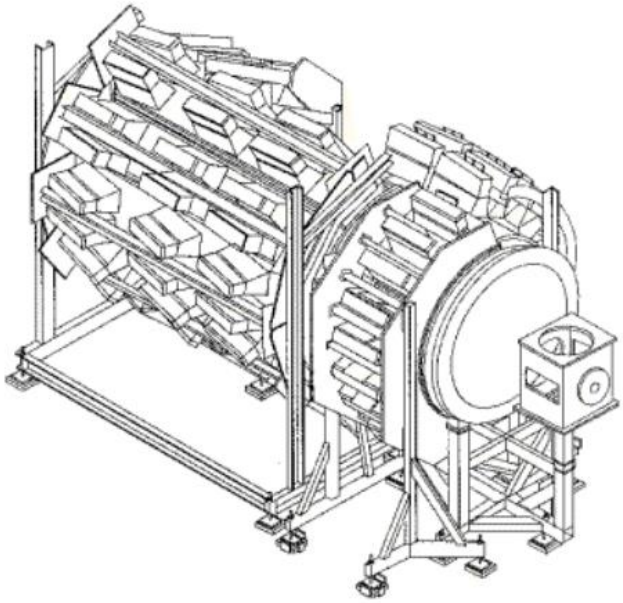

Fig. 2.6 Overview of the SANDALS diffractometer, taken from reference [18], which is the instrument used for collection of sample data in this project. SANDALS is an abbreviation of "Small Angle Neutron Diffractometer for Amorphous and Liquid Samples", a total scattering instrument designed for the diffraction of liquids and glasses and other disordered systems.

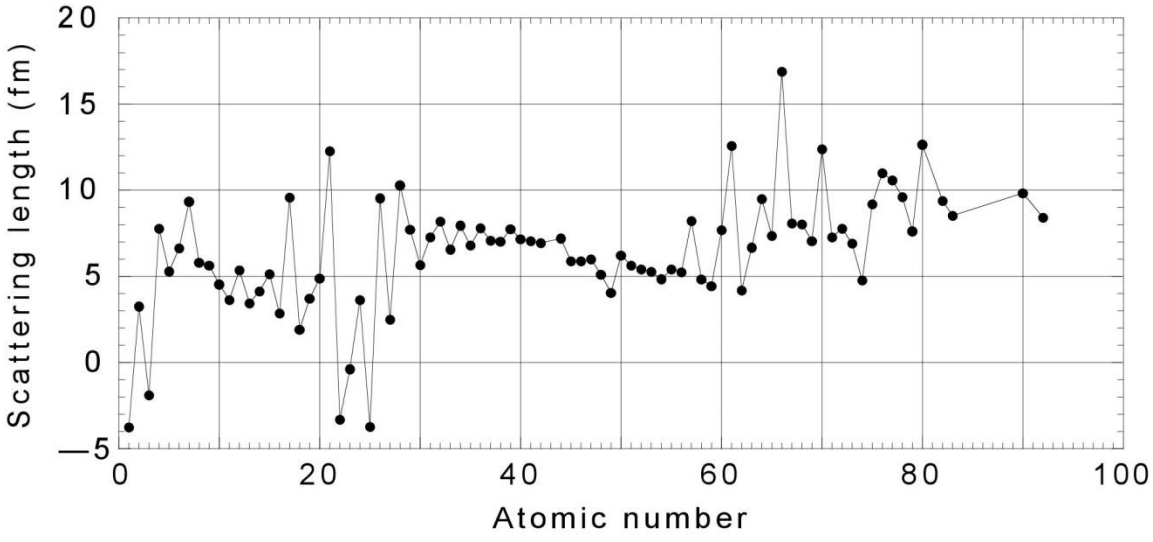

Fig. 2.7 Variation of neutron-scattering length with atomic number, taken from reference [19].

The nuclear interaction strength (scattering power) between the atom and the neutron is reflected by the scattering length b and a scattering cross section, σ [20], where $\sigma = 4\pi b^2$ (units of area). The sizes of atomic nuclei are 10^{-5} times those of the atoms, while the wavelength of neutrons in diffraction experiments are similar to those in X-ray experiments i.e. similar to the size of the atom. In this case, the scattering function is so wide in Q that it can be regarded as a constant for all values of Q of practical interest [11]. Thus, unlike the X-ray scattering factor, f, which is Q-dependent, the neutron scattering length b, is constant for each isotope and has no obvious relation with the value of Q. Indeed, it seems to vary in an irregular manner on moving across the periodic table, which means that it is independent of atomic number (**Fig. 2.7**). Usefully, the values of some lighter atoms have relatively large values of b, when compared to heavier atoms. Furthermore, because the neutron-nucleus scattering may or may not result in a change of phase of π of the neutron wave, the sign of the scattering amplitude can be either positive or negative [11].

2.4.2.5 Comparison of the characteristics of X-ray diffraction and neutron scattering

Electron shells of the atoms and the atomic nuclei scatter X-rays and neutrons, respectively. Different ways of interaction contribute to the advantages and disadvantages of each technique. Thus, these two are complementary to each other, and the proper choice of one method over the other, or combination of two methods in one studied material, is very important [21].

The scattering of X-rays is stronger than that of neutrons and X-ray beams are much more intense than neutron beams [11]. Also, large samples can absorb X-rays. Thus, much smaller samples are used for X-ray diffraction than in neutron beams. However, neutrons have relatively weak interactions with atoms, which makes them a highly sensitive and non-destructive probe, which can deeply penetrate a material. In this way, it can be used to investigate the bulk of a material rather than just its surface. Neutron scattering methods can locate the atomic nuclei precisely at relatively high angles, while X-ray scattering methods can only provide information on the distribution of the electron density in the same case. This is an important difference, since usually the nuclei are not located at the centre of the electron cloud, because of valence effects (electron cloud induced effects).

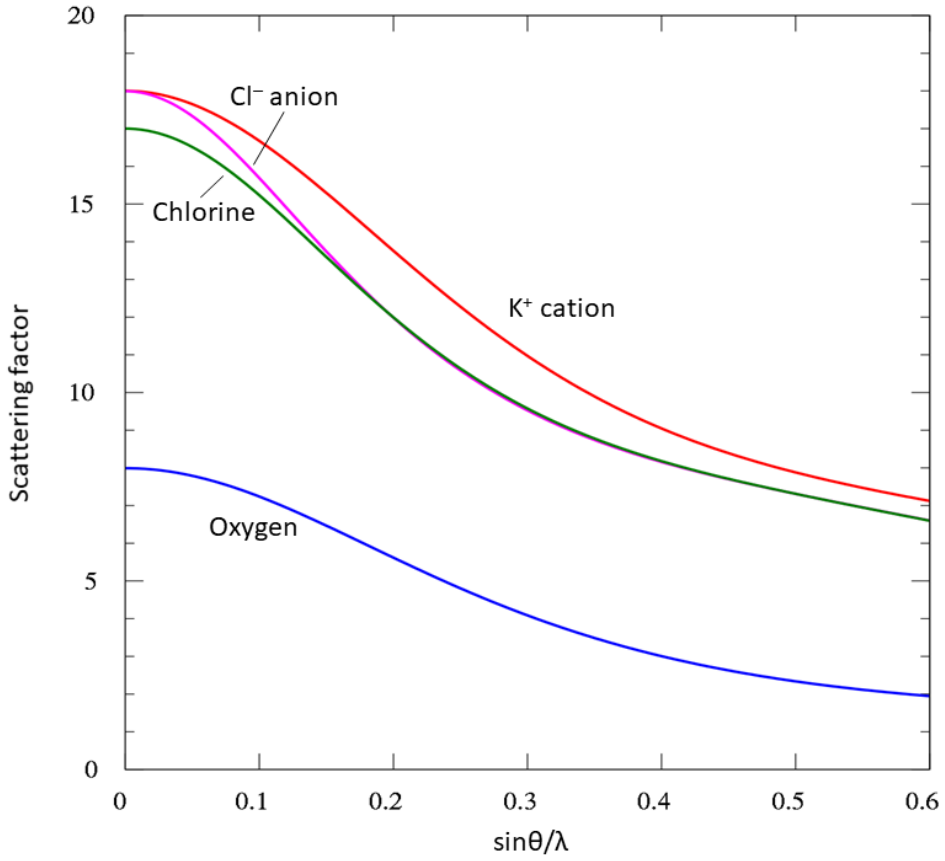

Fig. 2.8 Variation in X-ray atomic scattering factors of oxygen (blue), chlorine (green), Cl^- (magenta), and K^+ (red) with $\sin\theta/\lambda$.

In the periodic table neighbouring elements with similar atomic number, such as Mn and Fe or Co, possess similar X-ray scattering powers. Therefore, it is very difficult to distinguish them in compounds. Furthermore, in systems containing both light (i.e. low atomic number) and heavy (i.e. high atomic number) atoms, it is difficult to obtain precise scattering from relatively light atoms, since X-ray scattering will be dominated by the larger scattering power of the heavy atoms. As mentioned in **Section 2.4.2.3**, two neighbouring elements with similar atomic number can possess completely different neutron scattering powers (neutron scattering length). Thus, neutron scattering methods have the advantage of being able to distinguish neighbouring elements in the Periodic Table. Furthermore, none of the elements have exceptionally large neutron scattering lengths which could swamp the scattering of other atoms. In the case of studying a material including mixture of light and heavy atoms, neutron scattering might be the best possible structural analysis method [22]. For example, the hydrogen atom is virtually invisible to X-rays, but it has the same order of neutron scattering length as

any other atom. However, there are some pairs of atoms with completely different atomic numbers, but with similar neutron scattering length, such Cl and Br. In this case, structural elucidation might be better performed using X-ray techniques. In short, comparisons need to be made on a case by case basis before deciding whether X-ray or neutron scattering techniques are ideal for a particular system.

The size of the electron cloud of each atom is of the same order of magnitude, 10^{-10} m, which is comparable to that of the X-ray wavelength. This means that the electron cloud cannot be considered as a point; thus, waves scattered from different parts of a given atom (electron cloud) may have different path lengths. This small difference causes destructive interference, which consequently results in a reduction in diffraction intensity. The extent of destructive interference increases with Bragg angle. When X-rays with same wavelength λ, are scattered by a given atom, according to the relation between increasing wave vector **Q** and Bragg angle θ, $Q = |\mathbf{Q}| = 4\pi \sin\theta/\lambda$, the value of scattering factor *f* decreases as the value of *Q* increases (**Fig. 2.8**). Due to the size of the nucleus being in the order of 10^{-15} m, they can be treated as points when compared to the wavelength of the neutron beam. Thus, scattering angles cannot affect the nucleus-neutron scattering power. In summary, the X-ray scattering power of an atom falls off with increasing scattering angle to an extent that is determined by the inverse of the size of the atom, whereas with nucleus-neutron scattering the scattering power is independent of the scattering angle [11]. Thus, in cases where scattering at high angles is needed, neutron scattering may be the preferred method.

Unlike X-ray experiments, there is no laboratory alternative for neutron diffraction. Thus, neutron scattering cannot be implemented routinely, due to its high cost and being only accessible at national central facilities. X-ray methods are more widely used and are always the first choice to determine the structure of a given material, before further study for more precise information using neutron scattering.

2.4.3 Pair distribution functions

2.4.3.1 The basic scattering equations

Following the formalism given in [21,23], we can define the structure factor *F(***Q***)* as

$$F(\mathbf{Q}) = \sum_j f_j \exp\,(i\mathbf{Q}\cdot\mathbf{r}_j) \qquad (2.11)$$

which represents the scattering from a collection of particles, where f_j is the scattering length b for neutrons or the form factor $f(\mathbf{Q})$ for X-rays, and $\mathbf{Q}$ is the scattering vector. Neutron or X-ray diffraction experiments give the scattered intensity per unit atom $|F(\mathbf{Q})|^2$, $S(\mathbf{Q})$ as:

$$S(\mathbf{Q}) = \frac{1}{N}|F(\mathbf{Q})|^2 = \frac{1}{N}\sum_{j,k} f_j f_k \exp\left(i\mathbf{Q}\cdot\mathbf{r}_{jk}\right) \tag{2.12}$$

where $\mathbf{r}_{jk}$ is the separation between pairs of atoms $\mathbf{r}_{jk} = \mathbf{r}_j - \mathbf{r}_k$, and N is the total number of atoms in the sample.

2.4.3.2 Orientational average

In practice, the samples for total scattering analysis are usually non-crystalline or polycrystalline material solids. No matter which case, it is necessary to average over all orientations of $\mathbf{Q}$ and $\mathbf{r}_{jk}$:

$$\langle \exp\left(i\mathbf{Q}\cdot\mathbf{r}_{jk}\right)\rangle = \frac{1}{4\pi}\int_0^{2\pi} \mathrm{d}\phi \int_0^{\pi} \exp\left(iQr_{jk}\cos\theta\right)\sin\theta\,\mathrm{d}\theta \tag{2.13}$$

where $Q = |\mathbf{Q}|$, $r_{jk} = |\mathbf{r}_j - \mathbf{r}_k|$, and where θ and ϕ are angles in spherical coordinates (θ is the polar angle between $\mathbf{Q}$ and $\mathbf{r}_{jk}$, and ϕ is the azimuthal angle). The integration over ϕ leads to a simple factor of 2π. Hence the equation is written as:

$$\langle \exp\left(i\mathbf{Q}\cdot\mathbf{r}_{jk}\right)\rangle = \frac{1}{2}\int_{-1}^{+1} \exp\left(iQr_{jk}x\right)\mathrm{d}x = \frac{\sin(Qr_{jk})}{Qr_{jk}} \tag{2.14}$$

As a result, the orientation average scattering function is described as:

$$S(Q) = \frac{1}{N}\sum_{j,k} f_j f_k \frac{\sin(Qr_{jk})}{Qr_{jk}} \tag{2.15}$$

2.4.3.3 Defining the pair distribution function

When $j = k$, **Eqn. 2.15** contains two identical terms, and it is necessary to separate these terms from those where $j \neq k$:

$$S(Q) = \frac{1}{N}\sum_j f_j^2 + \frac{1}{N}\sum_{j\neq k} f_j f_k \frac{\sin(Qr_{jk})}{Qr_{jk}} \tag{2.16}$$

In the first term, we can assume that there are $c_m N$ atoms that are of type m; c_m is defined as the fraction of all atoms of type m, with $\sum_m c_m = 1$. Thus:

$$\frac{1}{N}\sum_j f_j^2 = \sum_m c_m f_m^2 \tag{2.17}$$

In the second term of the **Eqn. 2.16**, there is a double summation over all atoms. Taking into consideration the average behaviour expected from each atom type, the first part of the equation covers the sum of all individual atom types. On the other hand, because the second half of the equation is a sum covering all neighbouring atoms, it is feasible that the scanning distances and the probability of finding the next atom can be applied to replace it. This probability can be written as $g_{mn}(r)$, which represents the distribution of atoms of type n with respect to an atom m at the origin, as a function of distance (partial Pair Distribution Function). Assuming that $c_n\rho$ is the overall density of atoms of type n, where ρ means the overall number of atoms per volume, the number of atoms of type n ($\mathrm{d}N_{mn}$) lying within a spherical shell of thickness $\mathrm{d}r$ at a distance r from an atom of type m can be written as $4\pi r^2\mathrm{d}r \times c_n\rho \times g_{mn}(r)$, i.e. $\mathrm{d}N_{mn} = 4\pi c_n\rho g_{mn}(r)r^2\mathrm{d}r$. For application, if we consider a bond with a spread of distances $R \pm \Delta R$, the coordination number (CN) will be:

$$CN_{mn} = 4\pi c_n\rho \int_{R-\Delta R}^{R+\Delta R} g_{mn}(r)r^2\mathrm{d}r \tag{2.18}$$

In practice, we expect $g_{mn}(r)$ to be equal to 0 for values of r that fall below the smallest interatomic distance and to go to 1 when $r \to \infty$, as the atoms of type m and n have no correlations at large distances. As a result, the pair sum can be written as:

$$\frac{1}{N}\sum_{j,k} f_j f_k \frac{\sin(Qr_{jk})}{Qr_{jk}} = 4\pi\rho \int \sum_{m,n} c_m c_n f_m f_n r^2 g_{mn}(r) \frac{\sin(Qr)}{Qr}\mathrm{d}r \tag{2.19}$$

Thus, we can obtain:

$$S(Q) = \sum_m c_m f_m^2 + 4\pi\rho \int \sum_{m,n} c_m c_n f_m f_n r^2 g_{mn}(r) \frac{\sin(Qr)}{Qr}\mathrm{d}r \tag{2.20}$$

and define:

$$i(Q) = 4\pi\rho \int \sum_{m,n} c_m c_n f_m f_n r^2 g_{mn}(r) \frac{\sin(Qr)}{Qr}\mathrm{d}r \tag{2.21}$$

which is the total scattering structure factor. Because the function $g_{mn}(r) \to 1$ as $r \to \infty$, $i(Q)$ diverges at $Q = 0$. We can then separate the function into two parts

$$i(Q) = 4\pi\rho \int \sum_{m,n} c_m c_n f_m f_n r^2 (g_{mn}(r) - 1) \frac{\sin(Qr)}{Qr}\mathrm{d}r + 4\pi\rho \int \sum_{m,n} c_m c_n f_m f_n r^2 \frac{\sin(Qr)}{Qr}\mathrm{d}r \tag{2.22}$$

The second term of $i(Q)$ is non-zero only when $Q = 0$ which is experimentally inaccessible and therefore can be ignored. Thus, just the first term remains. If we define the PDF as

$$D(r) = 4\pi\rho r \sum_{m,n} c_m c_n f_m f_n (g_{mn}(r) - 1) \tag{2.23}$$

then $i(Q)$ can be written as

$$i(Q) = \int D(r) \frac{\sin(Qr)}{Q} \mathrm{d}r \tag{2.24}$$

We can obtain following transformations:

$$Qi(Q) = \int D(r) \sin(Qr)\, \mathrm{d}r \tag{2.25}$$

$$D(r) = \frac{2}{\pi} \int Qi(Q) \sin(Qr)\, \mathrm{d}Q \tag{2.26}$$

We can see that the two functions $D(r)$ and $Qi(Q)$ are the Fourier transform of each other.

If we consider that $g_{mn}(r) \to 0$ for value of r smaller than the location of the first peak in the PDF, we can obtain that $D(r) \to -4\pi\rho r \sum_{m,n} c_m c_n f_m f_n$ for small r. Similarly, $D(r)$ goes to 0 for large values of r, as $g_{mn}(r) \to 1$.

2.5 Electrical conductivity measurements

2.5.1 Introduction to electrochemical impedance spectroscopy (EIS)

Electrochemical Impedance Spectroscopy (EIS) represents a very significant method to electrically characterise materials. In the past a few decades, this method has been extended and broadened to the study of materials involving ionic conduction both in solid and liquid sates, especially in liquid. Further application of EIS has been made to the study of solids [2,24-26]. Nowadays, EIS has become a useful method of evaluating many of the electrical properties of materials and their interfaces [27] including ionic, semiconducting and mixed electronic-ionic materials.

EIS can be conducted using different methods, including AC Bridges, Lissajous Curves, Fast Fourier Transforms (FFT), Phase Sensitive Detections (PSD) and Frequency Response Analysis (FRA). FRA is regarded as the standard for EIS and is precise and sensitive.

In these impedance measurements, an alternating voltage is required. The frequency range is commonly from 0.01 Hz to 10 MHz. The general approach is to observe the response

to an alternating voltage through measurement of impedance (complex resistance). Typically, this involves the application of a range of single-frequency voltages and measurement of impedance in the frequency domain.

When the alternating voltage (at frequency of ω/2π) is applied, an alternating current is produced and shifted in phase from the voltage by θ. The delay (phase difference) represents the electrical response of the sample [28]. Both the magnitude (resistive) and phase shift (reactive) parts of impedance are frequency dependent.

The conventional definition of impedance is:

$$Z(\omega) = \frac{V_\omega}{I_\omega} = \frac{v(t)}{i(t)} \tag{2.27}$$

where $v(t) = V_0 \sin(\omega t)$ is a signal at frequency of ω/2π applied to the system, and $i(t) = I_0 \sin(\omega t + \theta)$ is the measured current. θ is therefore the phase difference between the voltage and the current. When θ is zero the impedance $Z(\omega)$ represents purely resistive behaviour.

The alternating voltage and current can be described by complex quantities including real and imaginary components. Assuming a linear response to the applied voltage, the waveforms can be sinusoidal. The voltage $V(t, \omega)$ can be given as

$$V(t,\omega) = V_0[\cos(\omega t) - i\sin(\omega t)] = V_0 e^{i\omega t} \tag{2.28}$$

and then the current $I(t, \omega)$ follows in the formula of

$$I(t,\omega) = I_0[\cos(\omega t + \theta) - i\sin(\omega t + \theta)] = I_0 e^{i(\omega t+\theta)} \tag{2.29}$$

where V_0 and I_0 are the amplitudes of voltage and the current separately, θ is the phase difference between the voltage and the current, and ωt is the angle in radians.

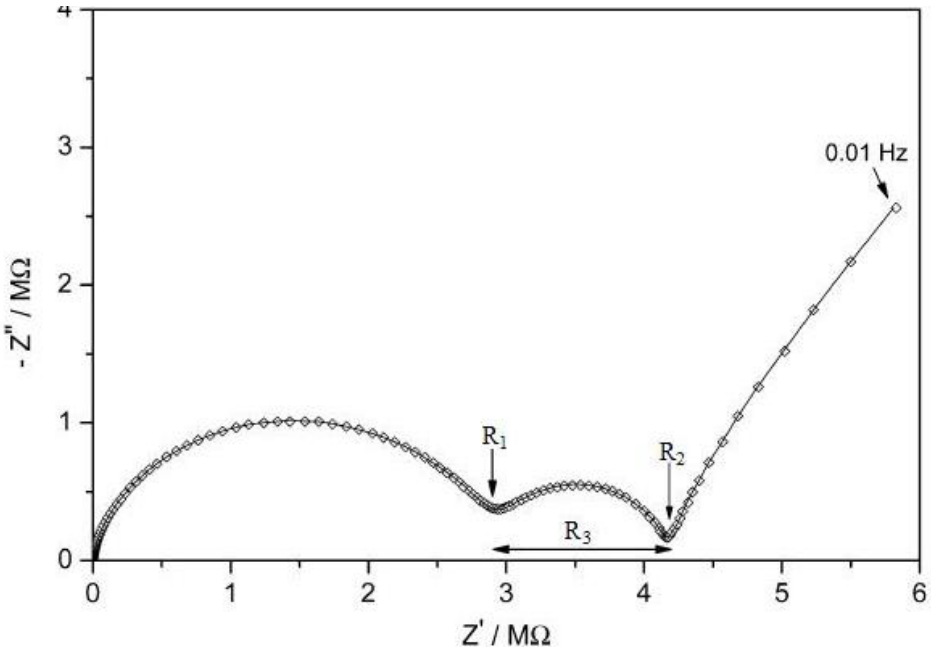

Fig. 2.9 Complex impedance spectrum for an ionic conductor, taken from reference [29]. The value of R_1 is the bulk contribution from microcrystalline conductor (intra-grain), the value of R_2 represents the total resistance, while R_3 is the grain boundary resistance.

In 1886, Heaviside [30] adapted the complex exponential functions above to the study of electrical circuits. In the complex form impedance can be described as:

$$Z(\omega) = \frac{V(\omega)}{I(\omega)} = |Z|e^{j\varphi} = Z' + jZ'' \tag{2.30}$$

where $Z' = |Z|\cos\theta$ and $Z'' = |Z|\sin\theta$. When $\theta = 0$, $Z' = R_e$ and when $\theta = \pi/2$, $Z'' = \frac{1}{\omega C}$. R_e is the frequency independent resistance and C is the capacitance.

In a right-hand orthogonal system of axes (complex plane) (**Fig. 2.9**), the magnitude and direction of the planar vector **Z** can be expressed by the value of the components Z' and Z''. Measurement of the impedance magnitude $|Z|$ and phase θ allows for the calculation of the real and imaginary parts of impedance, Z' and Z'' respectively.

2.5.2 Calculation of conductivity and activation energy

As shown in **Fig. 2.9**, in crystallised glasses the total resistance R (R_2) is represented by the sum of bulk R_b (R_1) and grain boundary R_{gb} (R_3) resistances, $R = R_b + R_{gb}$ ($R_2 = R_1 + R_2$).

However, in glasses the bulk resistance is the only resistance of the electrolytes. Thus, the conductivity of all investigated glass compositions can be calculated using the formula:

$$\sigma = \frac{1}{R} \times \frac{l}{S} \tag{2.31}$$

where l is the thickness of the pellet, S is the cross-sectional area (bottom area) of the pellet and R is the total resistance. The values of R, at each of the measuring temperature, were derived from the fitted complex impedance spectra.

The temperature dependence of conductivity is given by:

$$\sigma = \sigma_0 \exp\left(\frac{-E_a}{kT}\right) \tag{2.32}$$

where k is Boltzmann's constant and E_a is the activation energy for conductivity. Therefore, the activation energy can be calculated directly from the slope of a plot (Arrhenius Plots) of the logarithm of conductivity against the reciprocal of absolute temperature.

2.6 Molecular dynamics method

2.6.1 The integration algorithms

Molecular dynamics (MD) is a computer simulation method that can be considered a form of virtual reality. It is applied to the study of physical movements at the atomic scale, in particular N-body (multiple atoms and molecules) systems. In this simulation method the atoms and molecules interact with each other, based on the equation of Newtonian mechanics, namely $force = mass \times acceleration.$

A sequence of snapshot configurations is generated in the interaction process and each of the previous snapshots which are described by the positions, velocities and forces, can develop new snapshots. Nevertheless, in nature, the process of the interaction happens continuously. Therefore, time is continuous when the equation is integrated. However, in the simulation there is no choice but to separate the snapshots by the time interval Δt, which we shall call the time step. If the snapshots were given at times t, $t - \Delta t$, $t - 2\Delta t$ etc, the snapshot at time $t + \Delta t$ can be generated by a studied method which is required to satisfy time reversal and to be robust over many timesteps. The spatial coordinates ($\mathbf{r}(t + \Delta t)$ in the forward time direction and $\mathbf{r}(t - \Delta t)$ in backward time direction) need to be expanded as a Taylor expansion:

$$\mathbf{r}(t+\Delta t) = \mathbf{r}(t) + \frac{\partial \mathbf{r}(t)}{\partial t}\Delta t + \frac{1}{2}\frac{\partial^2 \mathbf{r}(t)}{\partial t^2}(\Delta t)^2 + \cdots \quad (2.33)$$

$$\mathbf{r}(t-\Delta t) = \mathbf{r}(t) - \frac{\partial \mathbf{r}(t)}{\partial t}\Delta t + \frac{1}{2}\frac{\partial^2 \mathbf{r}(t)}{\partial t^2}(\Delta t)^2 + \cdots \quad (2.34)$$

In the theory of Newtonian mechanics, we know that $force = mass \times acceleration$. If m is the particle mass, the velocity is defined as $\mathbf{v}(t) = \partial \mathbf{r}(t)/\partial t$ and the acceleration is defined as $\mathbf{a}(t) = \partial^2 \mathbf{r}(t)/\partial t^2$, we can develop the force $\mathbf{f}(t) = m\,\partial^2 \mathbf{r}(t)/\partial t^2$. Therefore, $\mathbf{r}(t+\Delta t)$ and $\mathbf{r}(t-\Delta t)$ are derived in the forms:

$$\mathbf{r}(t+\Delta t) = \mathbf{r}(t) + \mathbf{v}(t)\Delta t + \frac{\boldsymbol{f}(t)}{2m}(\Delta t)^2 + \cdots \quad (2.35)$$

$$\mathbf{r}(t-\Delta t) = \mathbf{r}(t) - \mathbf{v}(t)\Delta t + \frac{\boldsymbol{f}(t)}{2m}(\Delta t)^2 + \cdots \quad (2.36)$$

Equations for the position $\mathbf{r}(t+\Delta t)$ and the velocity $\mathbf{v}(t)$ can be obtained after subtracting, adding and slightly rearranging the two equations above:

$$\mathbf{r}(t+\Delta t) = 2\mathbf{r}(t) - \mathbf{r}(t-\Delta t) + \frac{\boldsymbol{f}(t)}{m}(\Delta t)^2 + O(\Delta t)^4 \quad (2.37)$$

$$\mathbf{v}(t) = \frac{\mathbf{r}(t+\Delta t) - \mathbf{r}(t-\Delta t)}{2\Delta t} + O(\Delta t)^3 \quad (2.38)$$

Both equations are called the Verlet Integration Algorithm. From the equations above, it seems that values obtained from focussing on positions rather than velocity will return a higher level of accuracy. Besides this, there are additional steps required to calculate the velocities. Meanwhile, through the method of Verlet Integration Algorithm, the equation of new positions is of no reference to the velocities. Thus, the lower accuracy of the velocities does not affect the new positions. Fortunately, more accurate values of velocities at the same time step can be generated through a refinement of the Verlet Integration Algorithm which is called the Velocity Verlet Method. To obtain these more accurate velocities, an intermediate point between two steps (one half of a timestep) needs to be taken into consideration for calculation. The velocity at the time $t + \Delta t/2$ can be written as a Taylor expansion:

$$\mathbf{v}(t+\Delta t/2) = \mathbf{v}(t) + \frac{1}{2}\frac{\partial^2 \mathbf{r}(t)}{\partial t^2}\Delta t \quad (2.39)$$

By adding, subtracting and rearranging this equation with **Eqn. 2.33**, we can obtain:

$$\mathbf{r}(t+\Delta t) = \mathbf{r}(t) + \mathbf{v}(t+\Delta t/2)\Delta t \quad (2.40)$$

At timestep $t + \Delta t$, the updated velocity can be generated as:

$$\boldsymbol{v}(t + \Delta t) = \boldsymbol{v}(t + \Delta t/2) + \frac{1}{2}\frac{\partial^2 \boldsymbol{r}(t+\Delta t)}{\partial t^2}\Delta t \tag{2.41}$$

The derived equation above seems like a Taylor expansion at time $t + \Delta t/2$ in step of $\Delta t/2$, which is considered at a wrong time. However, it is the fact that this equation is behind an expansion at $t + \Delta t$ in step of $-\Delta t/2$. After substituting, it follows that

$$\boldsymbol{v}(t + \Delta t) = \boldsymbol{v}(t) + \frac{1}{2}\left(\frac{\partial^2 \boldsymbol{r}(t+\Delta t)}{\partial t^2} + \frac{\partial^2 \boldsymbol{r}(t)}{\partial t^2}\right)\Delta t \tag{2.42}$$

which is the final expression and is commonly used in DL_POLY to calculate the velocity.

2.6.2 Thermodynamic ensembles

Molecular dynamics simulation always requires different ensembles associated with temperature, pressure and other quantities, to represent various environments. There are some relevant ensembles denoted as NVE, NPT, NVT *etc*., where N, V, E, P and T stand for the number of atoms, volume, the total energy, pressure, and temperature, respectively. For different purposes of the simulation, different ensembles are chosen accordingly, since each ensemble represents a particular conserved environment.

2.6.2.1 Microcanonical (NVE) ensemble

Through the integration algorithm mentioned in the previous section, the updated positions and velocities can be obtained after a related derivation and calculation. The equations form a scientific basis that ensures the conservation of the total energy, the sum of potential and kinetic energy. Meanwhile, in the studied system, the volume (or the shape) of the configuration and the number of particles must both be kept consistent. As such, this system has consistent levels of number of particles, volume, and energy, hence it is known as the microcanonical (NVE) ensemble in statistical thermodynamics.

The Hamiltonian for the microcanonical ensemble is written as

$$H = \sum_i \frac{p_i^2}{2m_i} + \frac{1}{2}\sum_i E(\boldsymbol{r}_i) \tag{2.43}$$

where m_i is the mass of atom labelled i with the corresponding modulus of the momentum $\mathbf{p}_i$, and $E(\mathbf{r}_i)$ is the potential energy of the atom with position $\mathbf{r}_i$. When summing up, each of the particles are counted twice. Therefore, the value of 1/2 is added to the equation.

2.6.2.2 Constant pressure (NPH) or constant stress (NSH) ensembles

In some studied particle systems, the volume can be allowed to change. Instead, the pressure is kept constant along with the number of particles. Thus, a constant value exists in this system, which is enthalpy. This kind of system is called a constant pressure (NPH) or constant stress (NSH) ensemble. For work on these ensembles, the volume (the size and shape included) change must be taken into consideration, which holds a special requirement which is fulfilled by adding new dynamical variables to the equation. They are the components of the edge vectors of the configuration, or the components of a strain tensor which can be related to the atomic variables through rescaling the coordinates. Rahmann and Parinello [31] demonstrated the first successful method to achieve this system with variable shape, after the problem of implementing a variable size by uniform shape system had been solved. In this case, the three edge vectors of the sample configuration are defined as **a**, **b** and **c**. A square matrix **h** is constructed by arranging these three vectors into columns. It follows that $V = \det(\mathbf{h}) = \mathbf{a} \cdot (\mathbf{b} \times \mathbf{c})$, where V is the volume. By defining the column vector $\boldsymbol{s}_i$ containing the fractional coordinates x_i, y_i and z_i, the position of a particle can be written in the form of $\mathbf{r}_i = \mathbf{h} \cdot \mathbf{s}_i = x_i\mathbf{a} + y_i\mathbf{b} + z_i\mathbf{c}$, where $\boldsymbol{r}_i$ is the position vector. Therefore, the square of the distance between the two particles can be derived in the form of $\mathbf{r}_{ij}^2 = \mathbf{s}_{ij}^{\mathrm{T}} \cdot (\mathbf{h}^{\mathrm{T}} \cdot \mathbf{h}) \cdot \mathbf{s}_{ij}$. As we know, the particle's equation of motion is derived from a Hamiltonian (or Lagrangian), with both potential energy and kinetic energy terms included, with the variables being the coordinates and the velocities. When new dynamic variables are introduced into the same framework as the microcanonical ensemble, analogous terms need to be constructed in the Hamiltonian. Thus, the Hamiltonian is obtained in this form:

$$H = \frac{1}{2}\sum_i m_i \dot{\mathbf{s}}_i^{\mathrm{T}} \cdot (\mathbf{h}^{\mathrm{T}} \cdot \mathbf{h}) \cdot \dot{\mathbf{s}}_i + \frac{1}{2}\sum_i E(\mathbf{s}_i, \mathbf{h}) + \frac{1}{2} M \mathrm{Tr}\left(\dot{\mathbf{h}}^{\mathrm{T}} \cdot \dot{\mathbf{h}}\right) + PV \qquad (2.44)$$

where M can be treated as an effective mass of the particle.

2.6.2.3 Constant temperature (NVT or NPT) ensemble

One tradition of the MD simulation requires researchers to generate a way to control temperature. In most cases, a given temperature will have a corresponding initial set of atom velocities. However, potential energy is released and converts into kinetic energy in the initial time steps because the distribution of potential energies of the atoms cannot be treated in the same way. It indicates that the samples would have to be heated up and many codes allow the velocities to be periodically changed until the simulation temperature fluctuates around a mean value which is roughly at the intended temperature. In this framework, the simulation is run in a system called the constant temperature (NVT or NPT) ensemble. Whilst this practical approach seems reasonable, it has no robust basis in statistical mechanics. Therefore, it is not feasible when a simulation process needs to continuously change its heat energy to maintain a constant temperature. A number of variants on the rescaling theme were proposed, and some of these are implemented in DL_POLY. Such methods ensure the MD simulation continues to progress around a chosen temperature. Unfortunately, no conservation laws exist in these methods, and as such they do not belong to any statistical mechanics ensemble. However, Nosè [32] developed a method which was refined by Hoover [33]. Nosè solved these problems by introducing a new variable, *s*, into the Hamiltonian. He scaled the momentum instead of space:

$$H = \sum_i \frac{p_i^2}{2m_i s^2} + \frac{1}{2}\sum_i E(\boldsymbol{r}_i) + \frac{1}{2}Q\dot{s}^2 + (3N+1)k_B T \ln s \qquad (2.45)$$

where N is the number of particles, Q is the effective mass and s scales the time. This Hamiltonian provides a distribution of particle energies consistent with the canonical ensemble. In this ensemble, the temperature is not a constant but instead fluctuates around an average value corresponding to the temperature of an effective heat bath in contact with the sample.

2.6.3 Ewald sum

In MD simulations, problems exist when researchers handle the Coulomb interaction due to its long range. This means that codes cannot use standard cut-offs for the interactions as for the short-range interactions. To solve this problem, the Ewald sum can be applied in MD simulations directly and is widely used in normal lattice simulations. In the method of Ewald [34] (described by Born and Huang [35]), the quantity $1/r$ was recognized to equal to a definite integral of the Gaussian function:

$$\frac{1}{r} = \frac{2}{\sqrt{\pi}} \int_0^\infty \exp(-r^2\rho^2) \mathrm{d}\rho \tag{2.46}$$

Therefore, the Coulomb energy can be expressed as:

$$E_\mathrm{C} = \frac{1}{2} \sum_l \sum_{i,j} \frac{Q_i Q_j}{2\pi^{3/2}\epsilon_0} \int_0^\infty \exp\left(-r_{ij}^2(l)\rho^2\right) \mathrm{d}\rho \tag{2.47}$$

where *i* and *j* label the pairs of atoms of charge Q_i and Q_j respectively, and *l* is the label of the copy of the configuration. By separating the integral in this equation into two parts, we can obtain:

$$\begin{aligned} \int_0^\infty \exp(-r^2\rho^2) \mathrm{d}\rho &= \int_0^g \exp(-r^2\rho^2) \mathrm{d}\rho + \int_g^\infty \exp(-r^2\rho^2) \mathrm{d}\rho \\ &= \int_0^g \exp(-r^2\rho^2) \mathrm{d}\rho + \frac{\sqrt{\pi}}{2} \frac{\mathrm{erfc}(gr)}{r} \end{aligned} \tag{2.48}$$

where g indicates an adjustable parameter and erfc(x) is the complementary error function which is defined as:

$$\mathrm{erfc}(x) = \frac{2}{\sqrt{\pi}} \int_x^\infty \exp(y^2) \mathrm{d}y \tag{2.49}$$

It is obvious that *r* plays a critical role in this system. When *r* is increased, the second term in **Eqn. 2.48** decreases to the value of zero quickly. On the other hand, the first term turns out to be useful with a transformation to reciprocal space. Ewald's transformation is shown as:

$$\frac{2}{\sqrt{\pi}} \sum_l \exp\left(-r_{ij}^2(l)\rho^2\right) = \frac{2\pi}{V} \sum_\mathbf{G} \rho^{-3} \exp(-G^2/4\rho^2) \exp\left(i\mathbf{G} \cdot \mathbf{r}_{ij}\right) \tag{2.50}$$

where r_{ij} is the distance vector between atoms *i* and *j*, *V* is the volume of the MD configuration, and **G** is the vector of the reciprocal lattice of the system with periodic boundaries. We need the integral:

$$\int_0^g \rho^{-3} \exp(-G^2/4\rho^2) \exp\left(i\mathbf{G} \cdot \mathbf{r}_{ij}\right) \mathrm{d}\rho = \frac{2\exp\left(-G^2/4g^2\right)}{G^2} \exp\left(i\mathbf{G} \cdot \mathbf{r}_{ij}\right) \tag{2.51}$$

Rearranging all the equations, we can obtain:

$$E_\mathrm{C} = \frac{1}{2} \sum_{ij} \frac{Q_i Q_j}{4\pi\epsilon_0} \sum_l \frac{\mathrm{erfc}\left(g r_{ij}(l)\right)}{r_{ij}(l)} + \frac{1}{2} \sum_{ij} \frac{Q_i Q_j}{4\pi\epsilon_0} \frac{4\pi}{V} \sum_{\boldsymbol{G}} \frac{\exp(-G^2/4g^2)}{G^2} \exp\left(i\mathbf{G} \cdot \mathbf{r}_{ij}\right) \tag{2.52}$$

One point was not discussed in the equations above; the terms $i = j$ for $l = 0$ must be included when the transformation to reciprocal space is being made, and this important point needs to be accounted for when the equations are derived. To solve this problem, the term needs to be separate from the real-space summation, which is obtained by subtracting the raw term. As a result, the term known as the self-energy is given as:

$$E_{\text{self}} = \lim_{r \to 0} \frac{Q_i^2}{4\pi\epsilon_0} \frac{\text{erfc}(gr) - 1}{r} \tag{2.53}$$

The numerator is equal to the error function, erf(gr), which is the limit of small argument $\text{erfc}(gr) \to 2gr/\sqrt{\pi}$. Thus, the term can be shown as:

$$E_{\text{self}} = -\frac{1}{4\pi\epsilon_0} \sum_i \frac{gQ_i^2}{\sqrt{\pi}} \tag{2.54}$$

We also have to consider the situation for **G** = 0 in the reciprocal space term. The value of the term for **G** = 0 is zero in a system with a centre of symmetry. However, it is difficult to calculate and analyse the term in a system without a centre of symmetry, because of dependence of the result on the direction in which **G** approaches the value of 0. Therefore, researchers frequently neglect the term for **G** = 0.

2.6.4 Potentials

Potentials, usually known as "force fields", are the mathematical equations that represent interactions between atoms in the studied system. These equations often include some parameters with values that can be obtained by fitting to data sets of experimental results. Crystallographic parameters (unit cell parameters, atomic positions) and physical properties (often elastic and vibrational quantities) are used for fitting processes. Researchers often obtain parameters by fitting to energies of crystals or clusters of atoms calculated by ab initio methods. In either case, values of parameters should have the best agreement with experimental data.

In this work, the model was used for amorphous states rather than crystalline. The atomic forces in glasses and in the corresponding crystals are of the same order of magnitude, because of the observation of similar mechanical properties. Crystalline solids and the corresponding glasses share the same local structure. It can therefore be assumed that a force field able to reproduce the properties of crystals can be reasonably applied in the simulation of the corresponding glasses [36].

Many sets of potentials (force fields) can be chosen for systems. In this work, the model of Pedone *et al.* [36] was applied for the simulations. There were two main reasons for this choice. First, this potential was developed for a range of elements, including Li, O, P and Mn that are studied in this work. Second, the potential was specially developed for application to glasses. The form of the potential used is:

$$E_{ij} = \frac{Q_i Q_j}{4\pi\varepsilon_0 r_{ij}} + D_{ij}\left[\left\{1 - e^{-a_{ij}(r_{ij}-r_0)}\right\}^2 - 1\right] \quad (2.55)$$

where ε_0 is the vacuum permittivity, r_{ij} is the distance between atom i and j, Q_i and Q_j are effective ionic charges of atom i and j, D_{ij} is the bond dissociation energy (the minimum energy of the function), r_0 is the is the equilibrium bond distance, and a_{ij} is the vibrational frequency.

The first term is the long-range Coulomb interaction between the charged ions. The effective ionic charge is not an exact charge quantity that ions possess. Since some electrons are distributed within a chemical bond, ionic charges may vary with changing chemical composition. Pedone *et al.* assumed that the value of the ionic charge should be a fitted parameter rather than given too exactly. For example, the charge value of the oxygen anion is set to –1.2 e because this value has been successfully used in some force fields, such as BKS potential for silicates. The second term is the classical Morse potential, the interaction combining short-range attraction and repulsion. The attractive interaction is associated with covalent bonding and the repulsion is caused by the overlap of electrons of neighbouring ions. Although the Coulomb interaction is not contained between atoms that are bonded with the Morse potential, Pedone *et al*. took the method of including the Coulomb interaction. They considered the parameters in the Morse potential as fitting parameters and treated them to have no physical significance. The values of parameters for materials containing Li, O, P and Mn, were taken from [36] and are summarised in **Table 2.2**:

Table 2.2 Potential parameters used in MD simulations [36].

Atom Pair	D_{ij} (eV)	r_0 (Å)	a_{ij} (Å^{-1})
$O^{-1.2} - O^{-1.2}$	0.042395	3.618701	1.379316
$Li^{0.6} - O^{-1.2}$	0.001114	2.681360	3.429506
$P^{3.0} - O^{-1.2}$	0.831326	1.800790	2.585833
$Mn^{1.2} - O^{-1.2}$	0.029658	2.852075	1.997543

From **Eqn. 2.55**, it is observed that the model is a pair-potential excluding terms that depend on bond angles. In the simulation of a glass formation process, melting a solid-state configuration and then quenching causes a continuous change of atomic neighbours. Thus, it is preferred that the model does not need to include these terms.

Five crystal structures, $Li_2MnP_2O_7$ [37], beta-$Li_2MnP_2O_7$ [38], $Li_2MnP_4O_{12}$ [39], $LiMnP_3O_9$ [40] and $LiMnPO_4$ [41], were taken as examples to test the performance of the chosen potential. The definition of lattice energy, is the sum of all pairwise interactions in the structure. A lattice-energy minimisation calculation was performed for each structure, which is used by most lattice simulation programs. The lattice program GULP package was used [42,43] for this work. Standard function minimisation techniques were used to determine the structure with lowest lattice energy and properties including vibrational frequencies at this minimum-energy structure. The structures generated for all five compositions are compared to those experimental observed in **Fig. 2.10-2.14**. The calculated structures contain the same structural elements that can be clearly identified. However, there are some small rotations of the structural polyhedra. For example, there are obvious differences between the experimental and calculated structures for $Li_2MnP_4O_{12}$, with the calculated one more compact.

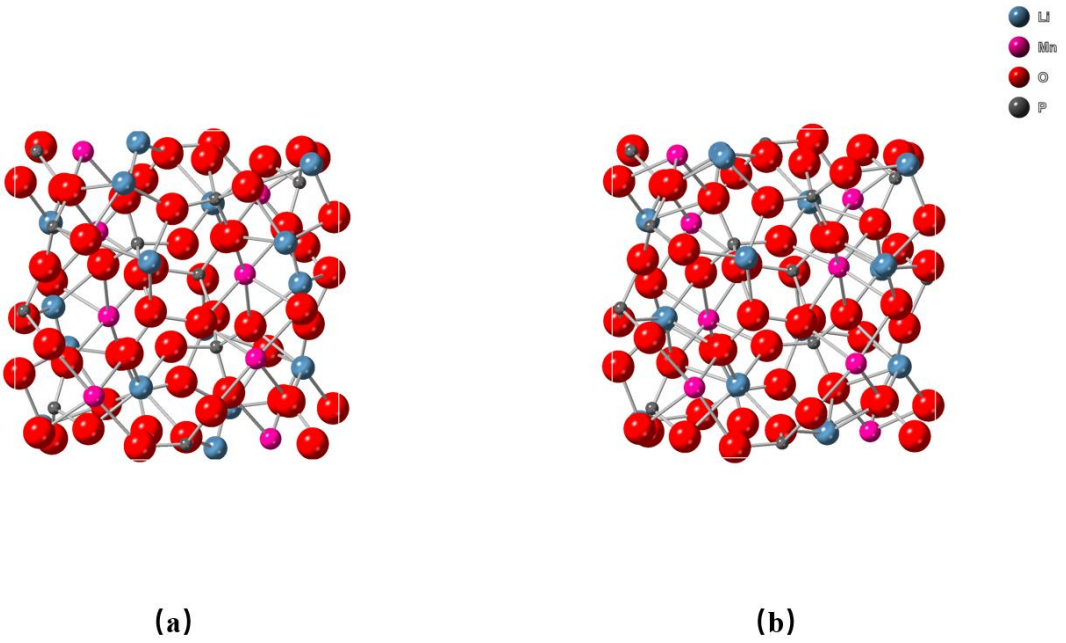

Fig. 2.10 The crystal structure of $Li_2MnP_2O_7$: (a) experimental and (b) calculated.

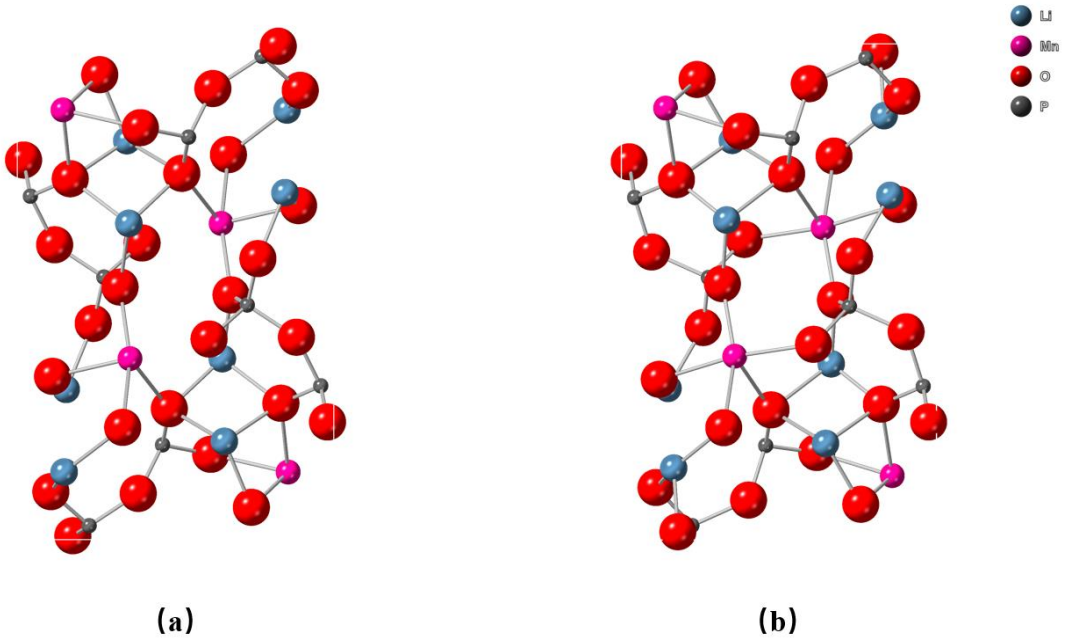

Fig. 2.11 The crystal structure of beta-$Li_2MnP_2O_7$: (a) experimental and (b) calculated.

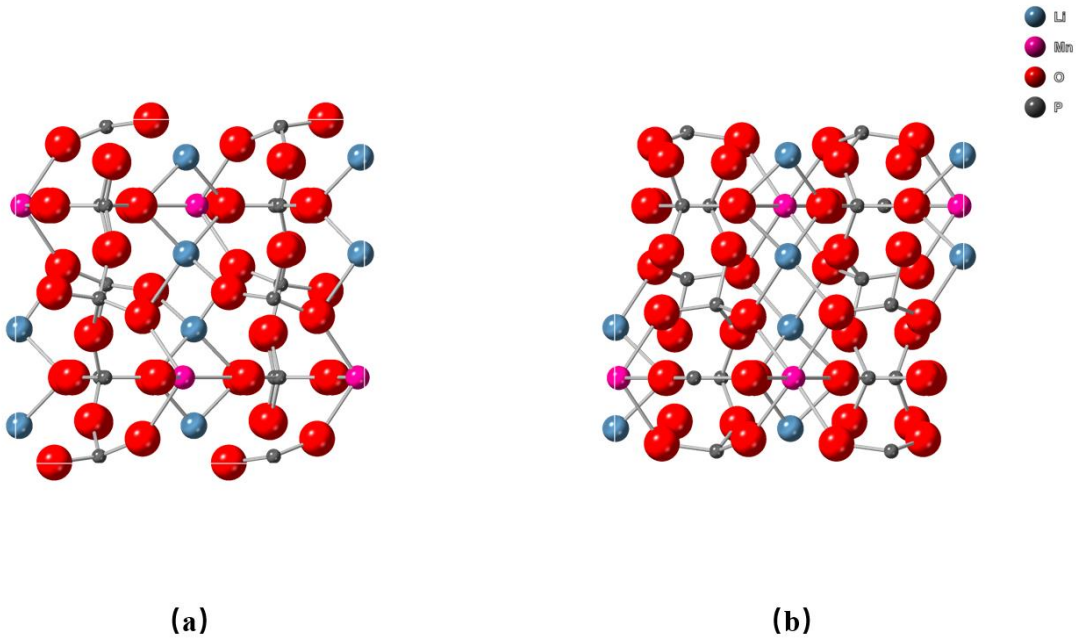

Fig. 2.12 The crystal structure of $Li_2MnP_4O_{12}$: (a) experimental and (b) calculated.

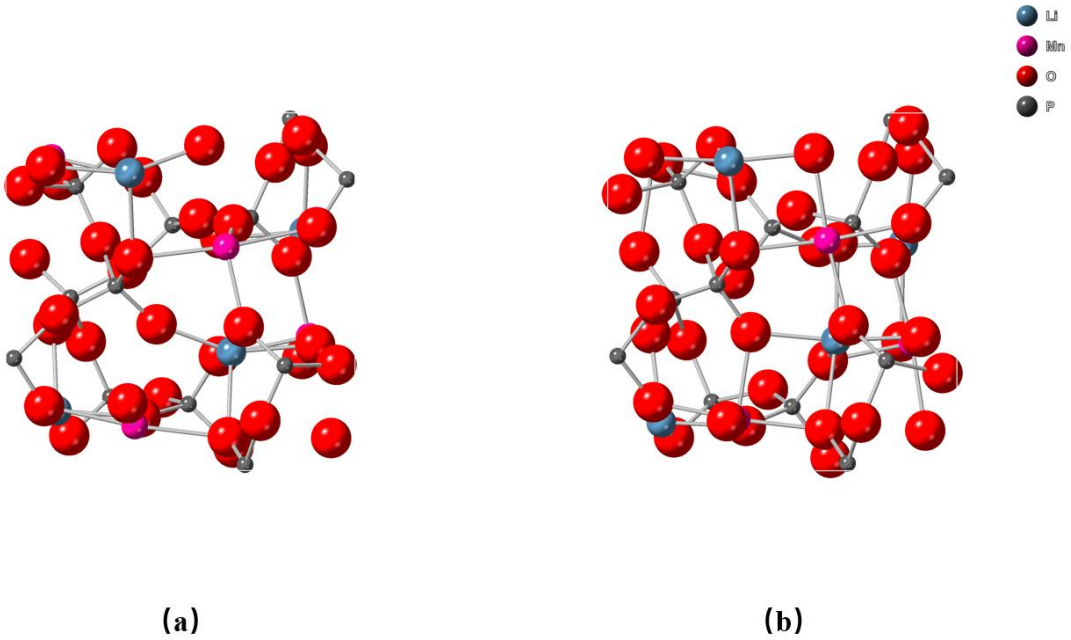

Fig. 2.13 The crystal structure of $LiMnP_3O_9$: (a) experimental and (b) calculated.

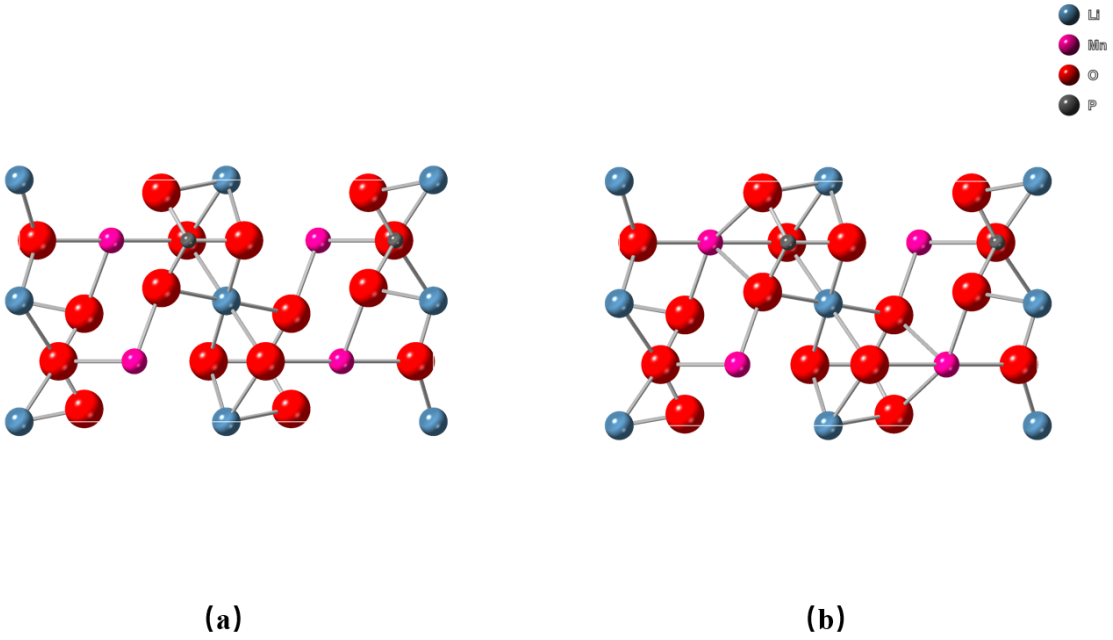

Fig. 2.14 The crystal structure of $LiMnPO_4$: (a) experimental and (b) calculated.

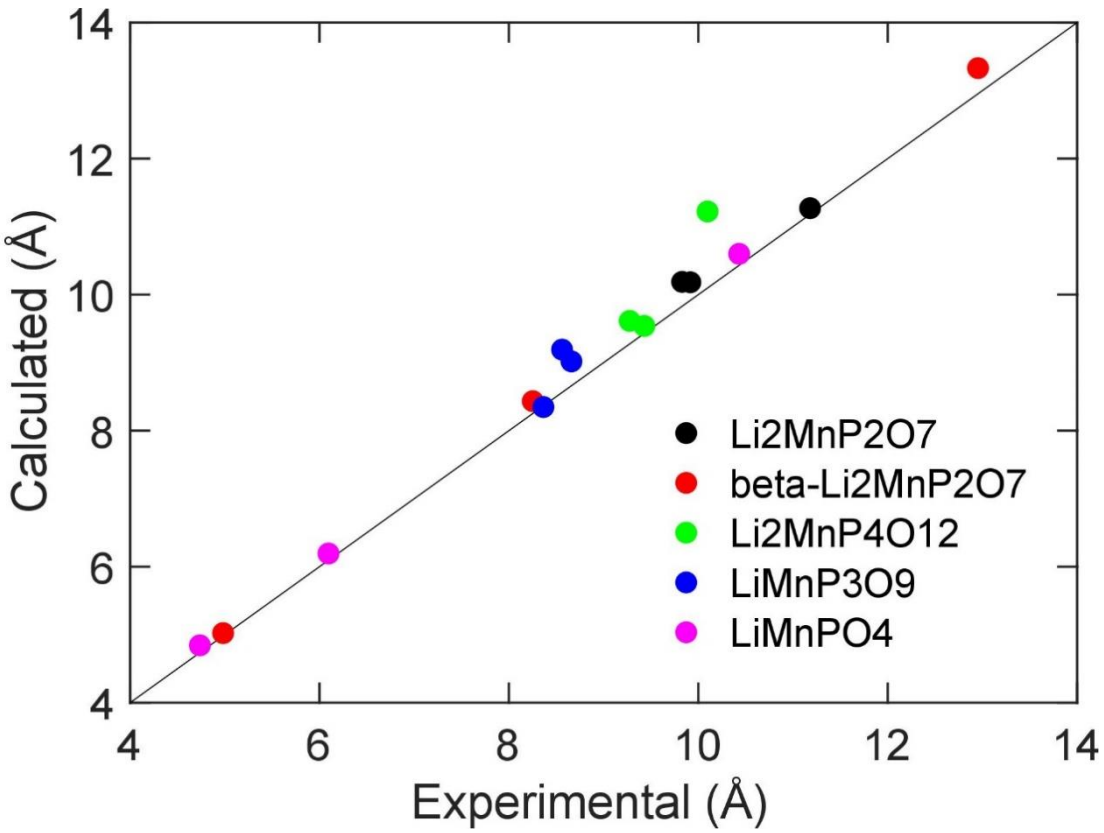

Fig. 2.15 Comparison of experimental and calculated lattice parameters for five crystalline lithium manganese phosphates.

A comparison of experimental and calculated lattice parameters for the five compositions is shown in **Fig. 2.15**. Typically, it is expected that the agreement between calculated and experimental lattice parameters should be within around 3%, and this is the case for most of the results. For most cases, the points in the plot of the two values are close to a straight line of unit gradient, which means that the model is good. However, there are some very large discrepancies. For example, one of the lattice parameters for $Li_2MnP_4O_{12}$ is far away from the straight line. The volume discrepancies between experimental and calculated results for $Li_2MnP_2O_7$, beta-$Li_2MnP_2O_7$, $Li_2MnP_4O_{12}$, $LiMnP_3O_9$, and $LiMnPO_4$ are about 8.53%, 6.12%, 16.54%, 11.58%, 5.6%, respectively. Thus, the model is least satisfactory for $Li_2MnP_4O_{12}$. This suggest that the force field differs somewhat in structures with different bonding frameworks.

In **Table 2.3** we compare the average bond lengths of each cation–oxygen pair between the experiment and calculated structures. Generally, the agreement is very good. The Li–O distances all show agreement better that 3% (usually with a slight under-estimate of the calculate values) and the Mn–O agreement 4% or lower (usually with a slight over-estimate for

the calculated value). The P–O distances are 3–6% under-estimated in the calculation, giving the most significant discrepancy between calculation and experiment.

Overall, the tests show that the model of Perdone *et al*. is not perfect, but that we can judge it to be adequate for the simulation of Li–Mn–P–O glasses. The largest discrepancy, namely too short a P–O distance, is unlikely to be significant in the modelling of the glass states. For the application in this thesis it was felt inappropriate to try to improve the model, given that one of its advantages is that it is likely to be free of any biases that might arise from fitting to a more focussed set of data.

Table 2.3 Average bond distances generated from the experimental and calculated, and differences for all five structures.

Composition	Bond type	Exp. (Å)	Cal. (Å)	Difference (%)
$Li_2MnP_2O_7$	Li−O	2.046	1.991	−2.68
	P−O	1.543	1.482	−3.98
	Mn−O	2.184	2.172	−0.52
beta-$Li_2MnP_2O_7$	Li−O	1.999	1.998	−0.06
	P−O	1.544	1.494	−3.25
	Mn−O	2.208	2.235	+1.22
$Li_2MnP_4O_{12}$	Li−O	2.169	2.157	−0.55
	P−O	1.534	1.448	−5.61
	Mn−O	2.185	2.276	+4.01
$LiMnP_3O_9$	Li−O	2.068	2.044	−1.14
	P−O	1.540	1.477	−4.09
	Mn−O	2.108	2.201	+4.23
$LiMnPO_4$	Li−O	2.142	2.179	+1.69
	P−O	1.543	1.489	−3.47
	Mn−O	2.207	2.222	+0.67

2.6.5 MD code

The algorithms given above are implemented in the general Molecular Dynamics (MD) code DL_POLY [44], with high performance for both parallel and serial simulations. All the MD simulations in this project were performed using DL_POLY version 4.08 [44] on Apocrita (a part of the MidPlus consortium).

2.7 References

1 A.West. Other techniques: Microscopy, spectroscopy, thermal analysis. *Basic Solid State Chemistry* **1**, 162-210 (1999).

2 Varshneya, A. K. *Fundamentals of Inorganic Glasses*. 1st edn, (Academic Press 2013).

3 Willard, H. H. *Instrumental methods of analysis*. 7th edn, (Wadsworth Publishing Company, 1988).

4 Muresan, D. *et al.* Structural investigation of calcium-soda-phosphate glasses with small content of silver oxide. *Journal of Optoelectronics and Advanced Materials* **8**, 558 - 560 (2006).

5 Schwarz, J., Ticha, H., Tichy, L. & Mertens, R. Physical properties of PbO-ZnO-P_2O_5 glasses. I. Infrared and Raman spectra. *Journal of Optoelectronics and Advanced Materials* **6**, 737-746 (2004).

6 Maas, J. H. V. *Basic Infrared Spectroscopy*. 1st edn, (Heyden & Sons Ltd, 1972).

7 Cullity, B. D. & Stock, S. R. *Elements of X-Ray Diffraction*. 3rd edn, (Pearson Education Limited, 2013).

8 Cheetham, A. K. & Day, P. *Solid State Chemistry: Techniques*. (Clarendon Press, 1988).

9 Ashcroft, N. W. & Mermin, N. D. *Solid State Physics*. (Holt, Rinehart and Winston, 1976).

10 Soper, A. K. Report RAL-TR-2011-013. (Rutherford Appleton Laboratory Technical, 2011).

11 Dove, M. T. *Structure and Dynamics: An Atomic View of Materials*. (Oxford University Press, 2013).

12 Soper, A. K. & Barney, E. R. Extracting the pair distribution function from white-beam X-ray total scattering data. *J. Appl. Cryst.* **44**, 714-726 (2011).

13 West, A. R. *Solid state chemistry and its applications*. 1st edn, (John Wiley & Sons, 2007).

14 Squires, G. L. *Introduction to the Theory of Thermal Neutron Scattering*. 1st edn, (Dover Publications Inc., 1978).

15 Windsor, C. G. *Pulsed Neutron Scattering*. 1st edn, (Taylor & Francis Ltd., 1981).

16 Bacon, G. E. *Neutron Diffraction*. 1st edn, (Oxford University Press, 1962).

17 Clearfield, A., Reibenspies, J. H. & Bhuvanesh, N. *Principles and Applications of Powder Diffraction*. 1st edn, (John Wiley and Sons, 2008).

18 http://www.isis.stfc.ac.uk, last accessed [30 Apr 2019]

19 Kearley, G. J. & Peterson, V. K. *Neutron Applications in Materials for Energy*. 1st edn, (Springer International Publishing, 2015).

20 Sears, V. Neutron scattering lengths and cross sections. *Neutron News* **3**, 26-37 (1992).

21 Bacon, G. E. *X-ray and Neutron Diffraction*. 1st edn, Vol. 2017 (Pergamon Press Ltd., 1966).

22 Clements, R., Hester, J. R., Kennedy, B. J. & Ling, C. D. The fluorite–pyrochlore transformation of $HO_2 - y\mathrm{Nd}y\mathrm{Zr}_2\mathrm{O}_7$. *Journal of Solid State Chemistry* **8**, 2108-2113 (2011).

23 Dove, M. T. An introduction to the use of neutron scattering methods in mineral sciences. *European Journal of Mineralogy* **14 (2)**, 203–224 (2002).

24 Macdonald, J. R. & Johnson, W. B. *Impedance Spectroscopy: Theory, Experiment, and Applications*. 3rd edn, (John Wiley & Sons, Inc., 2018).

25 Raistrick, I. D. Application of impedance spectroscopy to problems in solid state ionics. *Solid State Ionics* **18-19**, 40-49 (1986).

26 Jourdaine, L., Bonnat, M. & Souquet, J. Electrochemical measurement of the diffusion coefficient of silver in thin films of $V_2O_5P_2O_5$ glass. *Solid State Ionics* **18-19**, 461-466 (1986).

27 Irvine, J. T. S., Sinclair, D. C. & West, A. R. Electroceramics: Characterization by Impedance Spectroscopy. *Advanced Materials* **2**, 132-138 (1990).

28 Macdonald, J. R. Impedance spectroscopy. *Annals of Biomedical Engineering* **20**, 289–305 (1992).

29 Dygas, J. R. *et al.* Polycrystalline BIMGVOX.13 studied by impedance spectroscopy. *Solid State Ionics* **176**, 2085-2093 (2005).

30 Heaviside, O. *Electrical Papers*. (Macmillan & Co, 1892).

31 Rahman, M. P. a. A. Crystal Structure and Pair Potentials: A Molecular-Dynamics Study. *Phys. Rev. Lett.* **45**, 1196 (1980).

32 Nosé, S. A unified formulation of the constant temperature molecular dynamics methods. *J. Chem. Phys.* **81**, 511 (1984).

33 Hoover, W. G. Canonical dynamics: Equilibrium phase-space distributions. *Phys. Rev. A* **31**, 1695 (1985).

34 Ewald, P. P. Die Berechnung optischer und elektrostatischer Gitterpotentiale. *Ann. Phys.* **369**, 253-287 (1921).

35 Born, M. & Huang, K. *Dynamical Theory of Crystal Lattices*. 2nd edn, (Oxford University Press, 1954).

36 Pedone, A., Malavasi, G., Menziani, M. C., Cormack, A. N. & Segre, U. A new self-consistent empirical interatomic potential mode for oxides, silicates and silica-based glasses. *The Journal of Physical Chemistry B* **110**, 11780-11795 (2006).

37 Adam, L., Guesdon, A. & Raveau, B. A new lithium manganese phosphate with an original tunnel structure in the $A_2MP_2O_7$ family. *Journal of Solid State Chemistry* **181**, 3110-3115 (2008).

38 Nishimura, S.-I., Natsui, R. & Yamada, A. A new polymorph of lithium manganese (II) pyrophosphate β-$Li_2MnP_2O_7$. *Dalton Transactions* **43**, 1502-1504 (2014).

39 Moutataouia, M., Lamire, M., Saadi, M. & Ammari, L. Dilithium manganese (II) catena-tetrakis-(polyphosphate), $Li_2Mn(PO_3)_4$. *Acta Cryst.* **E70**, i1 (2013).

40 Murashova, E. V. & Chudinova, N. N. Synthesis and crystal structures of lithium polyphosphates, $LiPO_3$, $Li_4H(PO_3)_5$, and $LiMn(PO_3)_3$. *Crystallography Reports* **46**, 942–947 (2001).

41 García-Moreno, O. *et al.* Influence of the Structure on the Electrochemical Performance of Lithium Transition Metal Phosphates as Cathodic Materials in Rechargeable Lithium

Batteries: A New High-Pressure Form of $LiMPO_4$ (M = Fe and Ni). *Chem. Mater.* **13**, 1570-1576 (2001).

42 Gale, J. D. Empirical potential derivation for ionic materials. *Philosophical Magazine B* **73**, 3-19 (1996).

43 Gale, J. D. & Andrew, L. R. The General Utility Lattice Program (GULP). *Molecular Simulation* **29**, 291-341 (2003).

44 Todorov, I., Smith, W., Trachenko, K. & Dove, M. DL_POLY_3: new dimensions in molecular dynamics simulations via massive parallelism. *Journal of Materials Chemistry* **16**, 1911–1918 (2006).

Chapter 3 Structure and Conductivity in (50-*x*) Li_2O: *x*MnO: 50P_2O_5 Glasses

3.0 Introduction

This chapter deals with synthesis and structural investigation of two crystalline compositions $LiMn(PO_3)_3$ (lithium manganese metaphosphate) and $Li_2Mn(PO_3)_4$ (di-lithium manganese metaphosphate), and five glass compositions (50 − *x*) Li_2O: *x*MnO: 50P_2O_5 (*x* = 10.0, 25.0, 33.3, 40.0 and 50.0). Assuming, the MnO is network modifying, the samples are all metaphosphates, with an O:P ratio of 3. These compositions were chosen because of the expected ease of synthesis of the glasses (in general glasses with higher O:P ratios crystallise more easily). The crystalline systems have been studied used X-ray diffraction and the glass systems have been studied used density measurements, infrared spectroscopy, thermal analysis, neutron scattering, molecular dynamics simulations and electrical measurements.

3.1 Experimental

3.1.1 Synthesis

Samples of general composition (50−*x*) Li_2O: *x*MnO: 50P_2O_5 (**Table 3.1**) were prepared using appropriate amounts of reagent-grade Li_2CO_3 (BDH, 99.9%), MnO (BDH, 99.6%), and $NH_4H_2PO_4$ (May & Baker, 98.0%). For the neutron scattering PDF analysis Li_2CO_3 isotopically enriched in ^{6}Li (American Elements, $^6Li_2CO_3$, 94.61%; $^7Li_2CO_3$, 5.39%) was mixed with naturally abundant Li_2CO_3 (^{7}Li 92.41%; ^{6}Li, 7.59% [1]) to obtain “null lithium” glasses in which the average neutron scattering length of Li is approximately equal to zero.

Table 3.1 Compositions studied in this chapter.

Compositions (50−*x*) Li_2O: *x*MnO: 50P_2O_5	Value of *x*
40Li_2O: 10MnO: 50P_2O_5	10.0
25Li_2O: 25MnO: 50P_2O_5 (or $Li_2Mn(PO_3)_4$)	25.0
16.7Li_2O: 33.3MnO: 50P_2O_5 (or $LiMn(PO_3)_3$)	33.3
10Li_2O: 40MnO: 50P_2O_5	40.0
50MnO: 50P_2O_5	50.0

For standard glasses i.e., those containing naturally abundant lithium, appropriate amounts of the starting materials (Li_2CO_3, MnO, and $NH_4H_2PO_4$) were weighed accurately to give approximately 5 g of glass. The starting materials were ground together using an agate mortar and pestle as a slurry in industrial methylated spirits (IMS, VWR, 99%) for 15 min. The slurry was then dried in air at ambient temperature for at least 3 h. The dried mixture was placed in a platinum crucible and transferred to an electric muffle furnace (Lenton Laboratory Furnace AWF 12/5). The mixture was heated at 300 °C for 30 min to release the volatile decomposition products (H_2O and NH_3), then cooled and reground. The sample was reheated to 650 °C for 1 h to release CO_2. The sample was then heated to 1100 °C to achieve the melt, remaining at this temperature for at least 1 h. Glasses were obtained by quenching in air between two stainless-steel plates. Glasses were either dry ground in an agate mortar or broken up into small chunks. In both cases glasses were stored under vacuum over silica gel. The decomposition reactions at 300 and 650 °C are shown below:

$$2\ NH_4H_2PO_4\ (s) \xrightarrow{300\ °C} P_2O_5\ (s) + 4\ NH_3\ (g) + 3\ H_2O\ (g) \quad (3.1)$$

$$Li_2CO_3\ (s) \xrightarrow{650\ °C} Li_2O\ (s) + CO_2\ (g) \quad (3.2)$$

For preparations of "null lithium" glasses, all the processes such as grinding, heating and quenching were identical to those used for standard glasses. However, the $^6Li/^7Li$ isotopic ratio was adjusted to give "null lithium" i.e. to give an average neutron scattering length (b_{aver}) for lithium approximately equal to zero. These were prepared to create data sets where the

scattering was entirely due to the non-Li atoms. In this way the pair correlations involving Li could clearly be identified by subtracting the total pair distribution function of the null lithium sample from that of the natural lithium sample. The neutron scattering lengths of ^{6}Li (b_6) and ^{7}Li (b_7) are 2.00 fm and −2.22 fm respectively while that for natural Li (b_N) is −1.90 fm [2].

Assuming that x and y indicate the mole percentages of ^{6}Li and ^{7}Li, respectively, to make the average scattering length b_{aver} equal to 0, it follows that:

$$xb_6 + yb_7 = b_{aver} = 0 \quad (3.3)$$

Obviously, the total mole percentage has a value of 100%:

$$x + y = 100\% \quad (3.4)$$

Thus, using the scattering lengths given above we obtained x = 52.61% and y = 47.39%. Using the isotopic abundances of natural and isotopically enriched Li_2CO_3 the required masses of each are readily calculated for each composition.

Traditional solid-state reaction methods were used to prepare polycrystalline samples. As for the glass preparations, appropriate amounts of the starting materials (Li_2CO_3, MnO, and $NH_4H_2PO_4$) were ground together using an agate mortar and pestle as a slurry in IMS for 15 min and then dried in air at ambient temperature for 3 h. The dried mixture was placed in a platinum crucible and heated to 300 °C for 30 min and reheated to 650 °C for 1 h. The samples were then cooled and reground. In the case of $LiMn(PO_3)_3$, the mixture was reheated to 350 °C for 72 h, before slow cooling to room temperature in the furnace. In the case of $Li_2Mn(PO_3)_4$, the mixture was heated to 700 °C for 24 hours and then slow cooled to room temperature in the furnace.

A summary of the different synthesis conditions used for glass and crystalline samples is given in **Table 3.2**.

The compositions (50−x) Li_2O: xMnO: 50P_2O_5 (x = 25 and x = 33.3) were chosen for the glasses since they are isocompositional with the crystalline systems $Li_2Mn(PO_3)_4$ and $LiMn(PO_3)_3$ and hence a direct comparison can be made between the amorphous and crystalline structures.

Table 3.2 Summary of preparation parameters for samples of composition (50−*x*) Li_2O: *x*MnO: 50P_2O_5 described in this work, where G and C represent "glass" and "crystalline", respectively and "Li Type" indicates whether the samples were "natural" for naturally abundant Li or "null" for null-lithium. Slow cooling indicates that samples were left to cool exponentially in the furnace over a period of 6 to 12 h, while quenching involved rapid cooling onto a stainless-steel plate.

x	G /C	Li Type	Reaction 1		Reaction 2		Reaction 3		
			T (°C)	Time (h)	T (°C)	Time (h)	T (°C)	Time (h)	Cooling Procedure
33.3	C	natural	300	0.5	650	1	350	72	slow
25.0	C	natural	300	0.5	650	1	700	24	slow
33.3	G	Null	300	0.5	650	1	1100	1	quenched
25.0	G	Null	300	0.5	650	1	1100	1	quenched
50.0	G	natural	300	0.5	650	1	1100	1	quenched
40.0	G	natural	300	0.5	650	1	1100	1	quenched
33.3	G	natural	300	0.5	650	1	1100	1	quenched
25.0	G	natural	300	0.5	650	1	1100	1	quenched
10.0	G	natural	300	0.5	650	1	1100	1	quenched

3.1.2 Density measurements

Density measurements were performed by helium gas displacement (AccuPyc 1330 Pycnometer). Measurements were repeated at least five times and average values used. Density values are required for the calculation of free volume which is an essential measure of the structure compactness which can influence Li^+ mobility. In addition, density values are required for accurate data correction for PDF measurements and for the MD simulations.

3.1.3 Infrared spectroscopy

Infrared spectroscopy was carried out on a Perkin Elmer: Spectrum 65 FT-IR spectrometer in the range 600-1500 cm^{-1} with a resolution of 32 cm^{-1}. The measurements were made on powdered samples and all spectra were measured at room temperature. This

measurement was used to detect the approximate distribution of phosphate Q-species in studied glasses.

3.1.4 Thermal analysis

Combined thermogravimetric analysis (TGA) and differential thermal analysis (DTA), as well as differential scanning calorimetry (DSC) were used to investigate the thermal behaviour of glass and crystalline compositions, using a Thorn Scientific STA 1500 and a Perkin Elmer DSC-7, respectively. Samples of approximate mass 30 mg were subjected to controlled heating and cooling cycles. Thermograms were collected in air over the temperature range 20 °C to 1000 °C, with heating and cooling rates of 20 °C min^{-1}. TGA was used to confirm that no decomposition of the glass took place (eg. through volatilization), while DTA and DSC were applied to obtain the key temperatures of T_g, T_c and T_m, which give information on the network strength and the workability of the glass.

3.1.5 X-ray diffraction

Standard X-ray powder diffraction data were collected on a PANalytical X'Pert Pro diffractometer in flat plate θ/θ geometry using Ni filtered Cu-Kα radiation (λ = 1.5418 Å), in the 2θ range 5-70°, in steps of 0.033° with an effective count rate of 100 s per step. In the case of glass samples these measurements were used to confirm the amorphous nature. For Rietveld analysis of the crystalline samples $Li_2Mn(PO_3)_4$ and $LiMn(PO_3)_3$ data were collected on a Malvern PANalytical Cubix 3 diffractometer in flat plate θ/θ geometry using Ni filtered Cu-Kα radiation (λ = 1.5418 Å), in the 2θ range 5-120°, in steps of 0.0158° with an effective count rate of 400 s per step. These data were analysed using the GSAS refinement software [3] to yield details of the crystal structure. For X-ray scattering analysis, data were collected on PANalytical Empyrean diffractometer using Rh-filtered Ag-Kα radiation (λ = 0.5609 Å). Data were collected from 3-148° 2θ in θ/θ geometry with samples mounted in 1 mm diameter Kapton capillaries. Data were collected in steps of 0.033° 2θ, with a scan time of 440 s per step. For each sample five scans were summed to give the final data. Data sets for an empty Kapton capillary and the empty instrument were collected under the same conditions for data correction purposes, which was carried out using the GudrunX software [4]. In addition, further X-ray diffraction data were collected on the XPDF I51-1 diffractometer at the Diamond

Facility, Rutherford Appleton Laboratory. For these experiments, samples were loaded into 1 mm diameter silica glass capillaries. A wavelength of 0.1617 Å (E = 76.69 keV) was used over a large area detector (Q_{max} = 40 $Å^{-1}$) for 10 min for each sample. Data were analysed in the same way as the laboratory X-ray data using GudrunX [4]. Combined with the results from neutron diffraction, PDFs generated from X-ray data can provide some basic information, such as bond lengths.

Table 3.3 Dimensions of the loaded cans used to collect neutron data on glass compositions of general formula (50−x) Li_2O: xMnO: 50P_2O_5 (x = 10, 25, 33.3 and 50), where "Li Type" indicates whether the samples contained "natural" for naturally abundant Li or "null" for null-lithium.

Composition (x)	Li Type	Diameter (mm)	Height(mm)	Weight (g)
33.3	null	11	56	6.60
25.0	null	11	54	7.21
50.0	natural	11	58	8.66
40.0	natural	11	53	7.92
33.3	natural	11	57	7.66
25.0	natural	11	58	5.37
10.0	natural	11	57	6.59

3.1.6 Neutron scattering

Neutron scattering data were collected on the SANDALS diffractometer at the ISIS facility, Rutherford Appleton laboratory. Samples were loaded as large glass chunks into thin walled 11 mm diameter vanadium cans. The dimensions of the loaded cans are presented in **Table 3.3**. Total data collections of around 1800 μA h were made for each sample. Data sets for an empty can and empty instrument were collected for data correction purposes and data for a vanadium/niobium rod used for normalisation. Data correction was carried out using the GudrunN software [4]. Like the X-ray PDFs, neutron PDFs can offer experimental information about the structure of the studied glasses, with the added advantage of greater Q-range yielding

more accurate PDFs compared to those from X-ray scattering and the enhanced contribution of lithium to the neutron data.

3.1.7 Molecular dynamics (MD) simulations

MD simulations were performed using DL_POLY version 4.08 [5,6] on Apocrita (a part of the MidPlus consortium). Mentioned in **Section 2.6.4**, the form of the potential used is:

$$E_{ij} = \frac{Q_i Q_j}{4\pi\varepsilon_0 r_{ij}} + D_{ij}\left[\left\{1 - e^{-a_{ij}(r_{ij}-r_0)}\right\}^2 - 1\right] \quad (3.5)$$

The values of parameters were taken from the reference [7] and are summarised in **Table 2.2**.

The initial model was based on an NaCl lattice with random replacement of atoms to give the required stoichiometry. In each case, the size of the model was around 11000 atoms. MD simulations were performed with a constant temperature (NPT) ensemble. The equations of motion were integrated using the Nosé-Hoover algorithm [6]. Simulations were carried out in steps of 0.01 ps over a total of 20000 ps. Parallel calculations at different temperatures were carried for each composition to establish the melting temperature. This was judged by assessing the degree of crystallinity in the resulting $D(r)$ distributions. Final simulated melting temperatures of 2000, 2500, 3000, 2500 and 2000 K were used for the x = 10.0, 25.0, 33.3. 40.0 and 50.0 compositions, respectively. In each case, after 20000 ps a simulated quench to 300 K was performed to obtain the glass.

Table 3.4 Parameters for pellets of glass compositions (50−x) Li_2O: xMnO: 50P_2O_5 used in electrical measurements.

Composition	x	Bottom Area (mm^2)	Height (mm)	T_{max} (°C)	T_{min} (°C)
40Li_2O: 10MnO: 50P_2O_5	10.0	70.12	1.68	317	200
25Li_2O: 25MnO: 50P_2O_5	25.0	39.29	1.62	300	161
16.7Li_2O: 33.3MnO: 50P_2O_5	33.3	122.5	1.31	401	212
10Li_2O: 40MnO: 50P_2O_5	40.0	75.96	1.05	347	203
50MnO: 50P_2O_5	50.0	76.34	1.29	300	203

3.1.8 Electrical measurements

Conductivity and related activation energy are very important properties for electrode materials and can be obtained through electrical measurements. Five glass samples (**Table 3.4**) were selected. Pellets were produced by pouring the melt into a stainless-steel cylindrical mould. For all samples, pellets were polished using a selection of abrasive papers 1200 to 4000 grit. Finally, silver film electrodes were applied to the polished faces of sample pellets.

Electrical measurements were carried out using a computer controlled Autolab PGSTAT302N frequency response analyser in the frequency range from 0.1 to 330 kHz in air with an ac signal amplitude of 100 mV. Experiments were carried out at a set of stabilised temperatures during controlled heating and cooling cycles. The cooling measurements were performed to investigate possible thermal hysteresis. To avoid sample softening, the highest measurement temperature was about 30 to 60 °C below the corresponding glass transition temperature. The lowest measurement temperature was around 160 to 200 °C. **Table 3.4** summarises the pellet parameters and corresponding measuring conditions of the studied samples.

3.2 Results & discussion

3.2.1 Crystalline $LiMn(PO_3)_3$ and $Li_2Mn(PO_3)_4$

To provide a comparison with the glasses the crystal structures of two crystalline compositions $LiMn(PO_3)_3$ and $Li_2Mn(PO_3)_4$ were analysed. These crystalline phases are isocompositional with the x = 33.3 and 25.0 glass samples, respectively. Both powders were purple (lilac) in colour. The fitted X-ray powder diffraction profiles for crystalline $LiMn(PO_3)_3$ and $Li_2Mn(PO_3)_4$ are shown in **Fig. 3.1**. The starting model for $LiMn(PO_3)_3$ was taken from Murashova and Chudinova, while that for $Li_2Mn(PO_3)_4$ was taken from an unpublished single crystal structure from the Abrahams group [8]. Crystal and refinement parameters are given in **Tables 3.5** and **3.6**, refined structural parameters in **Tables 3.7** and **3.8**, significant bond lengths and angles given in **Tables 3.9** and **3.10**, for $LiMn(PO_3)_3$ and $Li_2Mn(PO_3)_4$, respectively.

(a)

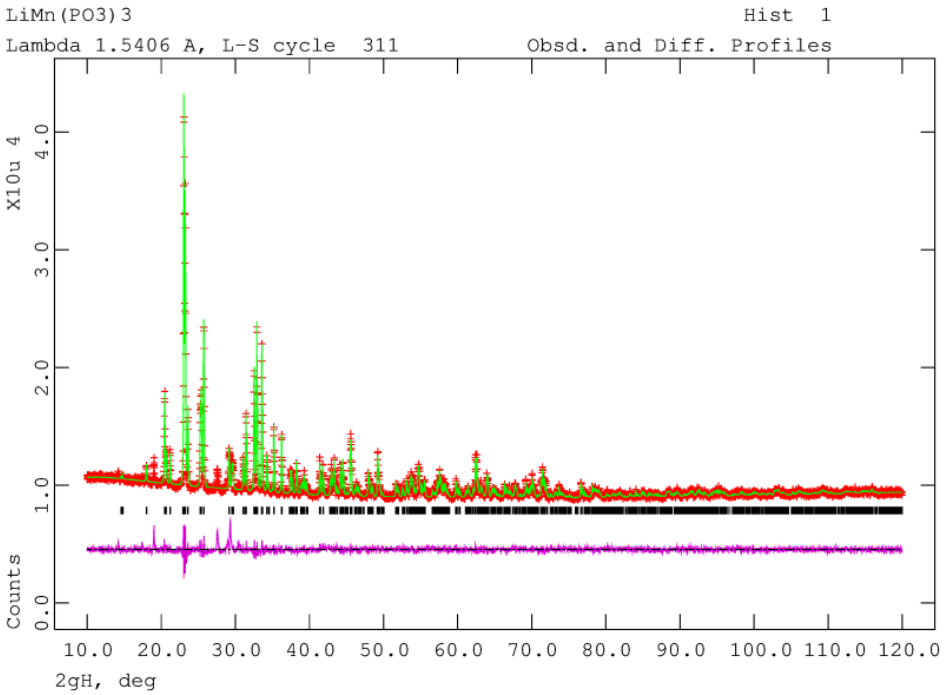

(b)

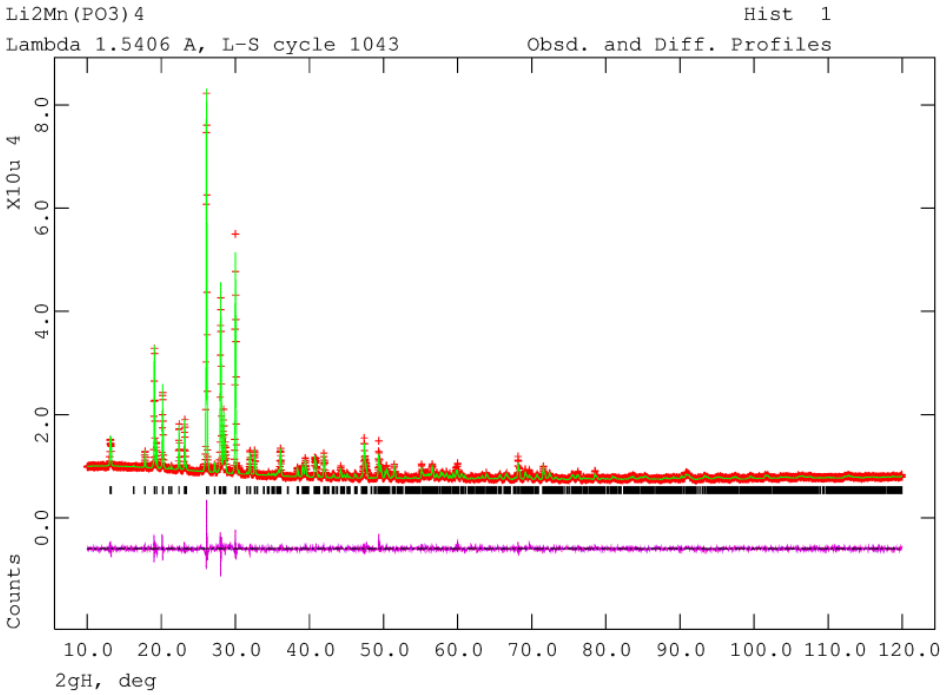

Fig. 3.1 Fitted X-ray powder diffraction profiles for (a) $LiMn(PO_3)_3$ and (b) $Li_2Mn(PO_4)_4$ showing observed (+ symbols), calculated (green line), and difference (lower magenta line) profiles. Reflection positions are indicated by markers.

Table 3.5 Crystal, Data Collection and Structure Refinement Data for $LiMn(PO_3)_3$. Estimated standard deviations are given in parentheses.

(a) Crystal data	
Name	Lithium manganese metaphosphate
Empirical formula	$LiMnO_9P_3$
Structural formula	$LiMn(P_3O_9)$
Formula weight	298.79 g mol^{-1}
Crystal system	Orthorhombic
Space group	$P2_12_12_1$
Unit cell dimensions	a = 8.4495(1) Å, b = 8.6711(1) Å, c = 8.7558(1) Å
Volume	641.50 (2) $Å^3$
Z	4
Density (calculated)	3.094 g cm^{-3}
Absorption coefficient μ	24.59 mm^{-1}
F(000)	580
Sample description	Purple powder
Synthesis	Solid state synthesis from Li_2CO_3, MnO and $NH_4H_2PO_4$
(b) Data collection	
Diffractometer	PANalytical Cubix 3
Scan mode	θ/θ
Temperature	293 K
Wavelength	1.5418 Å
2θ range collected	5-120°
Step size	0.0158°
Scan time	400 s
Monochromator/filter	Ni-filter
(c) Refinement	
Refinement software	GSAS (Larson and Von Dreele, 1986)
Initial model source	E. V. Murashova and N. N. Chudinova, Crystallography Reports 46 (2001) 942.
2θ range refined	10-120°
Excluded regions	5-10°
Data corrections	None
Secondary phases	$Li(PO_3)$ not modelled
No. of observations/restraints/parameters	6982/0/63
Total no. of reflections used	1161
Peak shape	Pseudo-Voigt
Final R-factors	R_p = 0.0179, R_{wp} = 0.0117 R_{ex} = 0.0101, χ^2 = 3.165 R_B = 0.0953
Maximum atomic shift (Å)	0.00

Table 3.6 Crystal, Data Collection and Structure Refinement Data for $Li_2Mn(PO_3)_4$. Estimated standard deviations are given in parentheses.

(a) Crystal data	
Name	Di-lithium manganese metaphosphate
Empirical formula	$Li_2MnO_{12}P_4$
Structural formula	$Li_2Mn(P_4O_{12})$
Formula weight	384.70 g mol^{-1}
Crystal system	Orthorhombic
Space group	*Pnma*
Unit cell dimensions	a = 9.4333(2) Å, b = 9.2814(2) Å, c = 10.1063(3) Å
Volume	884.85(5) $Å^3$
Z	4
Density (calculated)	2.888 g cm^{-3}
Absorption coefficient μ	22.13 mm^{-1}
F(000)	748
Sample description	Purple powder
Synthesis	Solid state synthesis from Li_2CO_3, MnO and $NH_4H_2PO_4$
(b) Data collection	
Diffractometer	PANalytical Cubix 3
Scan mode	θ/θ
Temperature	293 K
Wavelength	1.5418 Å
2θ range collected	5-120°
Step size	0.0158°
Scan time	400 s
Monochromator/filter	Ni-filter
(c) Refinement	
Refinement software	GSAS (Larson and Von Dreele, 1986)
Initial model source	A. Nadarajah, BSc project dissertation, School of Biological and Chemical Sciences, Queen Mary University of London 2013.
2θ range refined	10-120°
Excluded regions	5-10°
Data corrections	Preferred orientation
Secondary phases	None
No. of observations/restraints/parameters	6982/0/65
Total no. of reflections used	1422
Peak shape	Pseudo-Voigt
Final R-factors	R_p = 0.0255, R_{wp} = 0.0167 R_{ex} = 0.0108, χ^2 = 5.628 R_B = 0.1297
Maximum atomic shift (Å)	0.00

Table 3.7 Atomic Coordinates and Isotropic Thermal Parameters for $LiMn(PO_3)_3$. Estimated standard deviations are given in parentheses.

Atom	Site	x	y	z	Occ.	U_{iso} (Å^2)
Mn1	4a	0.1283(4)	0.8581(4)	0.1615(4)	1	0.015(3)
P1	4a	0.2014(7)	0.8070(8)	0.5634(7)	1	0.012(2)
P2	4a	0.3074(7)	0.5229(8)	0.6911(6)	1	0.012(2)
P3	4a	0.0308(6)	0.3243(6)	0.6824(8)	1	0.012(2)
O1	4a	0.1583(14)	0.8651(15)	0.4052(13)	1	0.009(3)
O2	4a	0.3127(13)	0.9085(11)	0.6592(13)	1	0.009(3)
O3	4a	0.2662(13)	0.6420(14)	0.5488(14)	1	0.009(3)
O4	4a	0.0388(12)	0.7728(12)	0.6504(13)	1	0.009(3)
O5	4a	0.3698(14)	0.6142(12)	0.8205(15)	1	0.009(3)
O6	4a	0.1243(14)	0.4702(14)	0.7346(13)	1	0.009(3)
O7	4a	0.5846(11)	0.8878(13)	0.8569(13)	1	0.009(3)
O8	4a	-0.1087(14)	0.3677(13)	0.5809(11)	1	0.009(3)
O9	4a	0.1252(13)	0.1919(13)	0.6156(11)	1	0.009(3)
Li1	4a	0.3464	0.8649	0.8842	1	0.02

Table 3.8 Atomic Coordinates and Isotropic Thermal Parameters for $Li_2Mn(PO_3)_4$. Estimated standard deviations are given in parentheses.

Atom	Site	x	y	z	Occ.	U_{iso} (Å^2)
Mn1	4c	0.5132(5)	0.25	0.3018(4)	1	0.088(4)
P1	8d	0.7926(5)	0.0411(8)	0.3912(4)	1	0.081(4)
P2	4c	0.8010(7)	0.25	0.6023(7)	1	0.081(4)
P3	4c	0.7755(8)	-0.25	0.5126(7)	1	0.081(4)
O1	8d	0.6267(10)	0.0494(15)	0.3743(10)	1	0.010(3)
O2	8d	0.8340(10)	0.1139(15)	0.5157(10)	1	0.010(3)
O3	4c	0.6490(15)	0.25	0.6273(14)	1	0.010(3)
O4	4c	0.6215(19)	-0.25	0.5104(14)	1	0.010(3)
O5	8d	0.8245(12)	-0.1223(15)	0.4198(8)	1	0.010(3)
O6	4c	0.8406(15)	-0.25	0.6356(12)	1	0.010(3)
O7	4c	0.8975(15)	0.25	0.7006(15)	1	0.010(3)
O8	8d	0.8789(12)	0.0688(14)	0.2710(9)	1	0.010(3)
Li1	8d	0.5031	0.1020	0.6694	1	0.010(3)

Table 3.9 Significant contact distances (Å) and angles (°) in $LiMn(PO_3)_3$. Estimated standard deviations are given in parentheses.

Mn1-O1	2.149(12)		P1-O1	1.518(12)
Mn1-O2	2.085(10)		P1-O2	1.537(12)
Mn1-O5	2.203(11)		P1-O3	1.537(10)
Mn1-O7	2.170(11)		P1-O4	1.599(10)
Mn1-O8	2.131(10)		P2-O3	1.656(12)
Mn1-O9	2.165(11)		P2-O5	1.479(13)
Li1-O1	2.349(13)		P2-O6	1.658(11)
Li1-O2	2.026(12)		P2-O7	1.543(12)
Li1-O5	2.253(10)		P3-O4	1.639(10)
Li1-O7	2.036(9)		P3-O6	1.560(12)
Li1-O8	2.031(11)		P3-O8	1.523(12)
Li1-O9	2.099(10)		P3-O9	1.515(11)
O1-Mn1-O2	87.4(6)		O1-P1-O2	117.0(7)
O1-Mn1-O7	97.0(5)		O1-P1-O3	108.6(9)
O1-Mn1-O8	175.5(5)		O1-P1-O4	106.9(7)
O1-Mn1-O9	94.4(5)		O2-P1-O3	111.1(6)
O2-Mn1-O7	173.7(5)		O2-P1-O4	111.8(7)
O2-Mn1-O8	88.3(5)		O3-P1-O4	100.0(7)
O2-Mn1-O9	87.8(4)		O3-P2-O5	108.5(8)
O7-Mn1-O8	87.2(5)		O3-P2-O6	98.5(6)
O7-Mn1-O9	87.3(4)		O3-P2-O7	113.1(7)
O8-Mn1-O9	84.1(4)		O5-P2-O6	107.7(8)
O1-Li1-O2	83.6(4)		O5-P2-O7	113.9(7)
O1-Li1-O5	169.3(5)		O6-P2-O7	113.9(7)
O1-Li1-O7	85.9(5)		O4-P3-O6	98.1(6)
O1-Li1-O8	87.7(4)		O4-P3-O8	108.1(6)
O1-Li1-O9	99.2(4)		O4-P3-O9	109.1(7)
O2-Li1-O5	87.2(4)		O6-P3-O8	111.3(7)
O2-Li1-O7	90.4(4)		O6-P3-O9	117.4(7)
O2-Li1-O8	90.3(5)		O8-P3-O9	111.7(7)
O2-Li1-O9	176.8(4)			
O5-Li1-O7	88.8(5)			
O5-Li1-O8	97.8(5)			
O5-Li1-O9	90.1(4)			
O7-Li1-O8	173.4(5)			
O7-Li1-O9	91.3(5)			
O8-Li1-O9	88.3(4)			

Table 3.10 Significant contact distances (Å) and angles (°) in $Li_2Mn(PO_3)_4$. Estimated standard deviations are given in parentheses.

Mn1-O1	2.270(13)		P1-O1	1.576(9)
Mn1-O1	2.270(13)		P1-O2	1.480(11)
Mn1-O4	2.285(16)		P1-O5	1.573(13)
Mn1-O6	2.173(14)		P1-O8	1.485(10)
Mn1-O8	2.231(13)		P2-O2	1.568(13)
Mn1-O8	2.231(13)		P2-O2	1.568(13)
Li1-O1	1.915(12)		P2-O3	1.456(15)
Li1-O3	1.991(10)		P2-O7	1.347(14)
Li1-O4	2.563(13)		P3-O4	1.452(18)
Li1-O5	3.013(10)		P3-O5	1.581(11)
Li1-O7	2.146(11)		P3-O5	1.581(11)
Li1-O8	2.192(11)		P3-O6	1.386(12)
O1-Mn1-O1	110.3(6)		O1-P1-O2	109.4(6)
O1-Mn1-O4	89.66(34)		O1-P1-O5	104.9(8)
O1-Mn1-O6	87.15(35)		O1-P1-O8	116.6(6)
O1-Mn1-O8	173.3(4)		O2-P1-O5	103.5(6)
O1-Mn1-O8	75.9(4)		O2-P1-O8	118.1(9)
O1-Mn1-O4	89.66(34)		O5-P1-O8	102.2(8)
O1-Mn1-O6	87.15(35)		O2-P2-O2	107.3(10)
O1-Mn1-O8	75.9(4)		O2-P2-O3	107.0(6)
O1-Mn1-O8	173.3(4)		O2-P2-O7	106.1(6)
O4-Mn1-O6	174.4(6)		O2-P2-O3	107.0(6)
O4-Mn1-O8	87.6(4)		O2-P2-O7	106.1(6)
O4-Mn1-O8	87.6(4)		O3-P2-O7	122.5(10)
O6-Mn1-O8	96.1(4)		O4-P3-O5	106.5(7)
O6-Mn1-O8	96.1(4)		O4-P3-O5	106.5(7)
O8-Mn1-O8	97.9(6)		O4-P3-O6	117.2(10)
O1-Li1-O3	154.0(4)		O5-P3-O5	97.1(9)
O1-Li1-O4	86.4(5)		O5-P3-O6	113.7(7)
O1-Li1-O7	108.3(4)		O5-P3-O6	113.7(7)
O1-Li1-O8	84.4(5)			
O3-Li1-O4	78.2(5)			
O3-Li1-O7	90.58(35)			
O3-Li1-O8	104.4(5)			
O4-Li1-O7	83.0(4)			
O4-Li1-O8	162.3(4)			
O7-Li1-O8	114.3(4)			

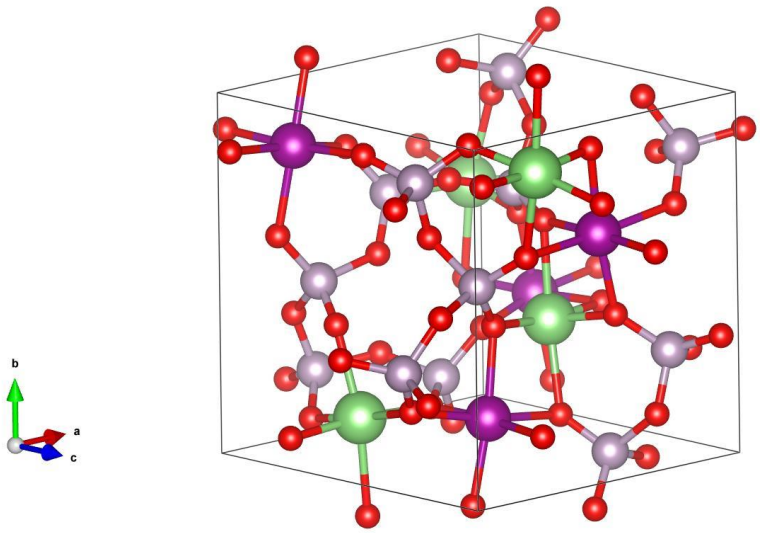

Fig. 3.2 Crystal structure of $LiMn(PO_3)_4$, oxygen atoms in red, phosphorus atoms in grey, manganese atoms in purple and lithium atoms in green.

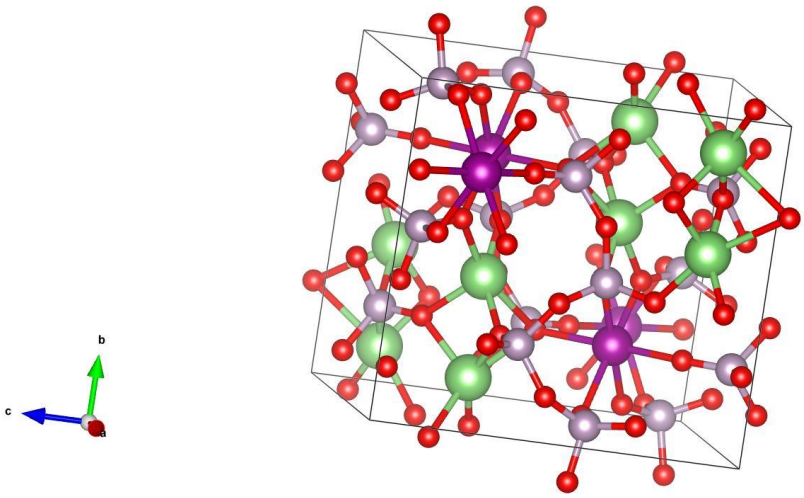

Fig. 3.3 Crystal structure of $Li_2Mn(PO_3)_4$, oxygen atoms in red, phosphorus atoms in grey, manganese atoms in purple and lithium atoms in green.

The structure of $LiMn(PO_3)_3$ (**Fig. 3.2**) consists of infinite $(PO_3)_n^{n-}$ chains, which corner share with MnO_6 octahedra to give the three dimensional structure. Each phosphate tetrahedron is therefore linked to two other phosphate tetrahedra and two manganate octahedra. Li^+ ions are located in octahedral sites, which edge share with the manganate octahedra. The P-O bond

lengths are in the range 1.48 to 1.66 Å, while the average Li−O and Mn−O distances are 2.13 Å and 2.15 Å.

The structure of $Li_2Mn(PO_3)_4$ is shown in **Fig. 3.3** and consists of Q^2 phosphate chains running parallel to the *b*-axis. These chains are linked together via corner sharing manganate octahedra. The Li atoms are 5-coordinate in distorted 4 pyramidal sites (defect octahedral) which face share with each other and corner share with the phosphate chains. A sixth Li-O contact at 3.0 Å is too long to be considered to be bonding. The average Mn-O distance is 2.24 Å, while that for Li-O and P-O are is 2.16 Å and 1.50 Å, respectively.

Subsequent to the start of this work, the structure of $Li_2Mn(PO_4)_2$ was published by Moutataouia *et al.*[9]. The structure reported here and in that in the literature are very similar.

3.2.2 Glass formation

3.2.2.1 General results

All the glasses were transparent and purple in colour due to the high concentration of Mn^{2+}. The purple colour deepened with increasing Mn^{2+} concentration. After grinding samples to fine powders, the samples had a light pink colouration (**Fig. 3.4**).

X-ray powder diffraction patterns for synthesised standard glass compositions $(50-x)$ Li_2O: xMnO: $50P_2O_5$ (x = 10.0, 25.0, 33.3, 40.0 and 50) are shown in **Fig. 3.5**. The patterns each show a single broad halo centred at approximately 25° 2θ, characteristic of an amorphous solid with no indication of crystallisation as shown by the absence of Bragg peaks. The results confirm that glass formation was successful for this range of compositions.

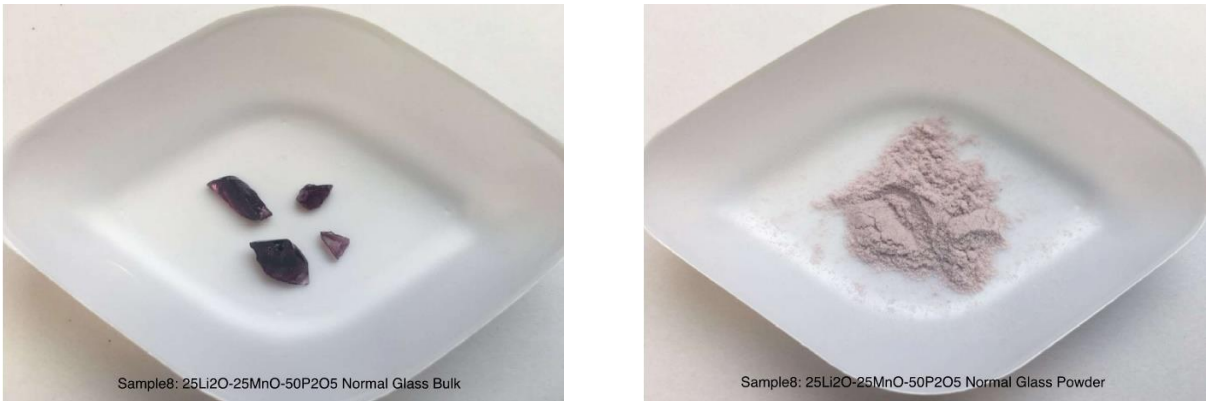

(a) **(b)**

Fig. 3.4 Appearance for glass samples of compositions $25Li_2O{:}25MnO{:}50P_2O_5$ in forms of bulk (a) and powder (b).

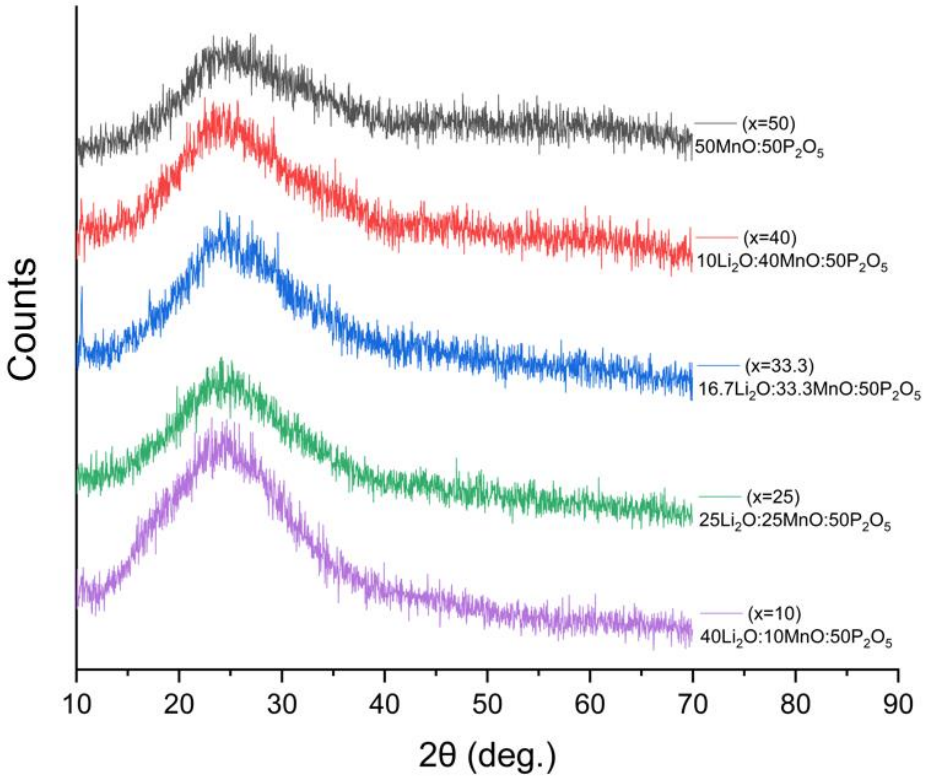

Fig. 3.5 XRD patterns for synthesised standard glass compositions $(50-x)\ Li_2O{:}\ xMnO{:}\ 50P_2O_5$ (x = 10.0, 25.0, 33.3, 40.0 and 50.0).

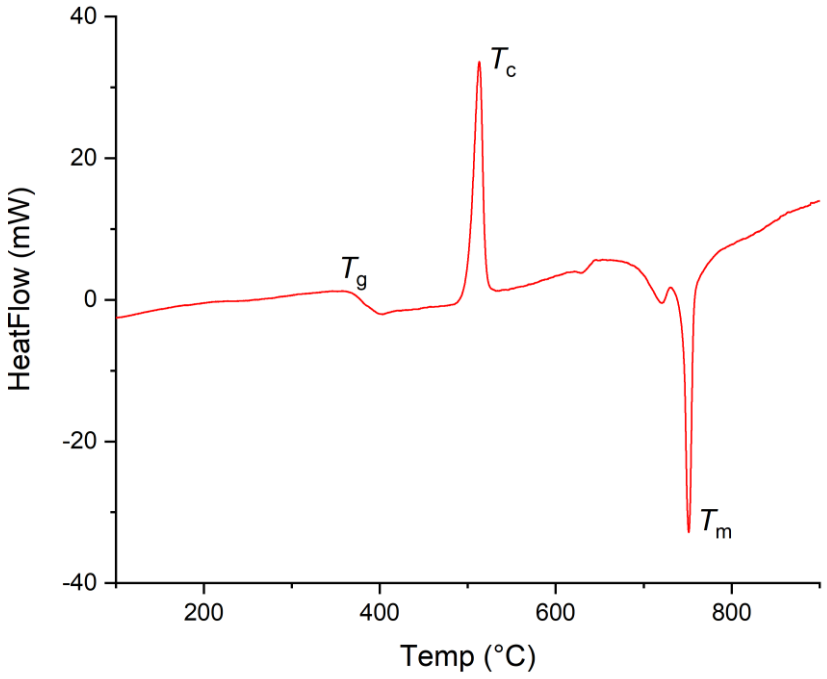

Fig. 3.6 DSC thermogram for glass sample with composition $25Li_2O$: $25MnO$: $50P_2O_5$.

DSC was used to measure the thermal behaviour of the glass samples. **Fig. 3.6** shows the DSC thermogram for the x = 25.0 glass sample, which is typical. On heating, the endothermic deflection at 360 °C represents the glass transition temperature, T_g, while the first exothermic peak, indicates the crystallisation of the glass T_c at 512 °C. This is followed by an endothermic peak corresponding to the melting temperature T_m at 751 °C. The value of T_g depends on the thermal history of the studied material (i.e. the rate of cooling of the melt) and can occur over a broad temperature range. The stability of the glass against crystallisation (the value of T_c - T_g) is relatively high at 152 °C, which means that the glass is relatively easy to form by quenching in air. The high value of T_g means that this material could potentially be used in a solid-state battery, up to 360 °C, without softening or crystallising.

The thermal event temperatures for all compositions are listed in **Table 3.11**. The compositional variation of T_g, T_c, $T_c - T_g$ and T_m is shown in **Fig. 3.7**. It is evident that as the concentration of manganese increases, T_g firstly increases to a maximum value (at x = 33.3) and then drops. For the melting temperature (T_m), the trend is similar to that for T_g.

Table 3.11 Summary of thermal parameters for glass samples of general composition (50−*x*) Li_2O: *x*MnO: 50P_2O_5 (Estimated uncertainty is ±5%).

Glass Composition(s) (*x*)	T_g (°C)	T_c (°C)	$T_c - T_g$ (°C)	T_m (°C)
10.0	340	484	144	650
25.0	360	512	152	751
33.3	447	610	163	847
40.0	408	548	140	749
50.0	364	603	239	729

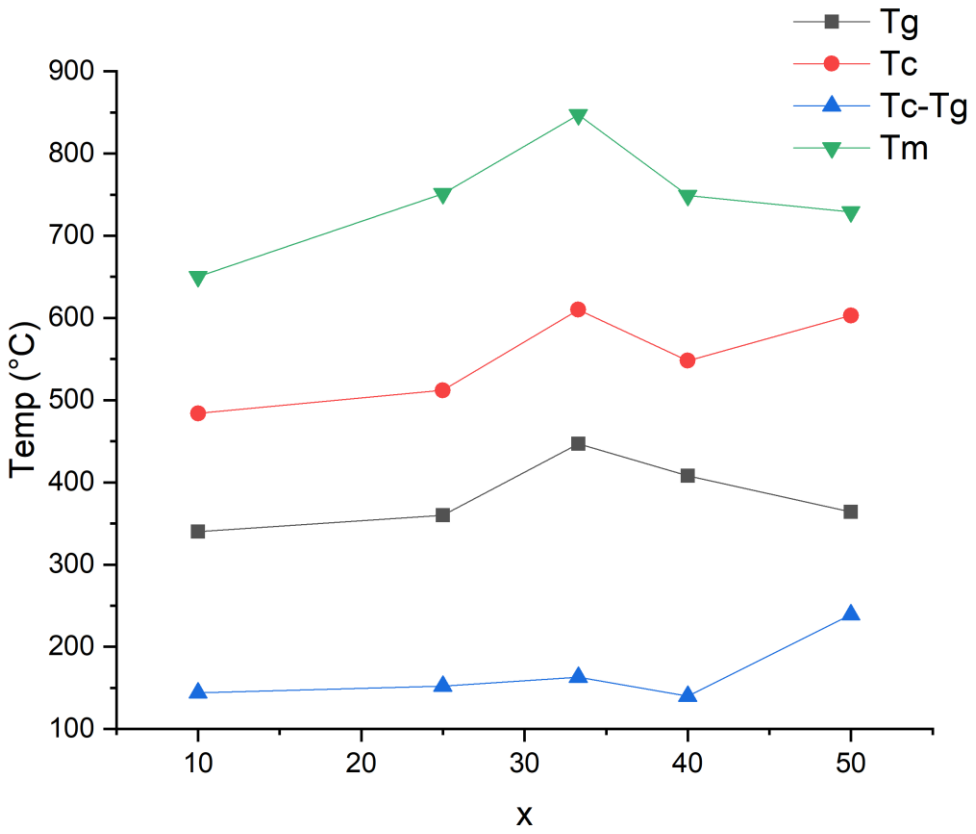

Fig. 3.7 Compositional variation of T_g, T_c, T_c - T_g and T_m in glasses of composition (50-*x*) Li_2O: *x*MnO: 50P_2O_5

T_g reflects the strength of the glass network, i.e. higher T_g values indicate a stronger network. To explain the observed trend in T_g the role of Mn^{2+} needs to be considered. This ion

can act as a network former or a network modifier and is therefore termed a network intermediate. As *x* increases, the Mn content increases, while the Li content decreases. Since each Mn^{2+} replaces $2Li^{+}$ cations, the total number of cations decreases with increasing *x*. This means there would be fewer cross-links between the phosphate chains which would be expected to cause a weakening of the phosphate network. However, the fact that up to $x = 33.3$, T_g increases, suggests that at least some of the Mn acts as a network former, strengthening the glass network. At low Mn concentrations the network forming Mn^{2+} cations would have a coordination number of 4 and form a local tetrahedral arrangement of oxygen neighbours. As the Mn concentration increases above $x = 33.3$, the coordination number increases to 5 or 6. Additionally, as the concentration of Mn increases, the concentration of lithium decreases by twice as much, which allows more oxygen atoms to be closer to Mn to form these higher coordination geometries. At the same time, as discussed above, the decreasing number of cations as *x* increases results in fewer cross-links between the phosphate chains, which also contributes to the decreasing T_g when *x* is above 33.3.

It is helpful at this stage to consider the theoretical speciation in the glass. If it is assumed that only the phosphate units constitute the network and that Li^{+} and Mn^{2+} are network modifiers, then for each composition the total modifying charge is simply the sum of the contributions from Li+ and Mn^{2+}. For example in the case of the $x = 33.3$ composition, the formula may be written as $LiMn(PO_3)_3$**.** In this case the total modifying charge is +3. This must be balanced by the charge on the phosphate network. In a glass, four phosphate species are possible depending on the number of bridging oxygens i.e. Q^0, Q^1, Q^2 and Q^3. These have average formulae of $(PO_4)^{3-}$, $(PO_{3.5})^{2-}$, $(PO_3)^{-}$ and $(PO_{2.5})^0$. For the $x = 33.3$ composition, since there are 3 P atoms per formula unit, the modifying charge can be entirely balanced using only Q^2 phosphate species. The possibility of other species cannot be excluded since for example an equal number of Q^3 and Q^1 species would give the same total network charge. This could occur through disproportionation **Eqn. 3.6**.

$$2(PO_3)^{-} \rightarrow (PO_{2.5})^0 + (PO_{3.5})^{2-} \qquad (3.6)$$

However, if the Mn^{2+} adopts a network forming role (usually 4 coordinate) then other types of species may be present. For example, in the $x = 33.3$ composition if all the manganese was network forming in 4 coordinate geometry then just as with P, a variety of species could form depending on the number of bridging oxygens, such as $(MnO_4)^{6-}$ (Q^0), $(MnO_{3.5})^{5-}$ (Q^1), $(MnO_3)^{4-}$ (Q^2), $(MnO_{2.5})^{3-}$ (Q^3) and $(MnO_2)^{2-}$ (Q^4). In this case, the total modifying charge is

solely from the Li^+ i.e. +1 per formula unit. The total anionic network charge would be the sum of the contributions from the manganate and phosphate species. If it is assumed that the Mn is present as a Q^4 species i.e. $(MnO_2)^{2-}$ then there is too much anionic charge to achieve electroneutrality. If it is assumed that only 3/4 of the Mn are network forming Q^4 species, then the total cation charge is now +1.5 per formula unit. This cation charge is entirely balanced by the manganate Q^4 species meaning that the phosphate species would all have to be Q^3. Thus, it is entirely possible in this glass composition to have a proportion of the manganese in a network forming role, but no more than 75%. Similar calculations can be performed for the other compositions.

From the discussion above, it is highly possible that the x = 33.3 composition may be viewed as a critical composition above which point Mn^{2+} must adopt octahedral geometry.

Table 3.12 Summary of densities of all glass samples in the series (50-x) Li_2O: xMnO: $50P_2O_5$ (x = 10.0, 25.0, 33.3, 40.0 and 50.0) and "Li Type" indicates that samples were standard for naturally abundant Li or "null lithium".

Composition(s)	Li Type	Density (g/cm^3)
$16.7Li_2O$: 33.3MnO: $50P_2O_5$	Null lithium	2.764 (±0.004)
$25Li_2O$: 25MnO: $50P_2O_5$	Null lithium	2.666 (±0.004)
50MnO: $50P_2O_5$	Standard	2.950 (±0.002)
$10Li_2O$: 40MnO: $50P_2O_5$	Standard	2.846 (±0.003)
$16.7Li_2O$: 33.3MnO: $50P_2O_5$	Standard	2.784 (±0.003)
$25Li_2O$: 25MnO: $50P_2O_5$	Standard	2.683 (±0.006)
$40Li_2O$: 10MnO: $50P_2O_5$	Standard	2.493 (±0.003)

Table 3.12 shows the measured densities for synthesised glasses in the series (50−x) Li_2O: xMnO: $50P_2O_5$ (x = 10.0, 25.0, 33.3, 40.0 and 50.0). The compositional variation for the glasses made with naturally abundant Li (standard) is shown in **Fig. 3.8**. The plot shows an increase in density with increasing x-value. This is to be expected since the formula mass increases as the heavier manganese substitutes two lighter lithium atoms as x-increases.

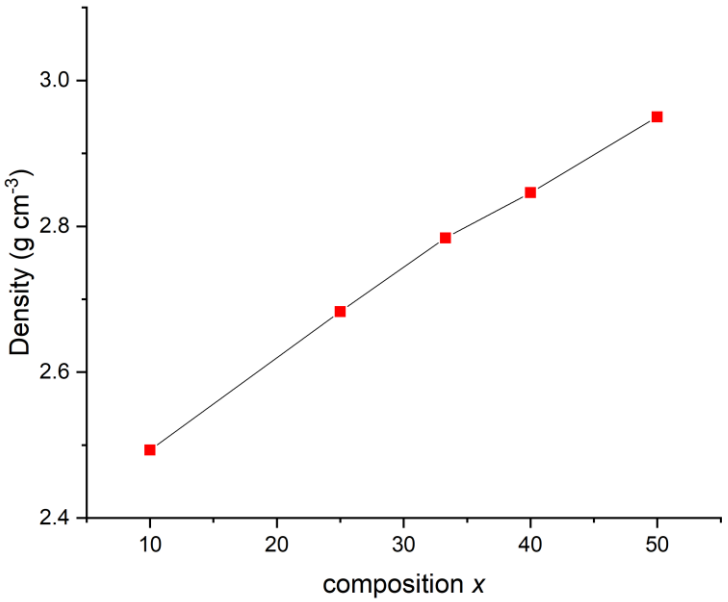

Fig. 3.8 Compositional variation of density for the synthesised standard glasses in series (50−*x*) Li_2O: *x*MnO: 50P_2O_5 (*x* = 10.0, 25.0, 33.3, 40.0 and 50.0). Estimated standard deviations are smaller than the symbols used.

In order to assess the underlying trend in density independent of the formula mass increase it is helpful to examine the change in free volume. The free volume is essentially a measure of how compact the studied glasses are. The percentage free volume (%V_{free}) can be defined as [10]:

$$\%V_{\text{free}} = 100\% \times \frac{V_{FU} - V_{\text{ion}}}{V_{FU}} \tag{3.7}$$

where V_{FU} is the volume per formula unit and V_{ion} is the calculated ionic volume, respectively, as shown by equations

$$V_{FU} = \frac{M_r}{\rho N_A} \tag{3.8}$$

$$V_{\text{ion}} = \sum_i n_i \frac{4}{3}\pi r_i^3 \tag{3.9}$$

in which M_{r} indicates the formula unit mass in g mol^{-1}, ρ stands for the measured density in g cm^{-1}, N_{A} is Avogadro's constant, n_i is the number of ions of type *i* per formula unit and r_i is the ionic radius in Å of ion type *i*. By using the measured density, the %*V* of various compositions

were calculated (the values of ionic radius are taken from Shannon; for Mn^{2+}, a value of 0.75 Å was assumed corresponding to the ion in high spin state coordinate geometry [11]). The compositional variation of the free volume (%V_{free}) is presented in **Fig. 3.9**.

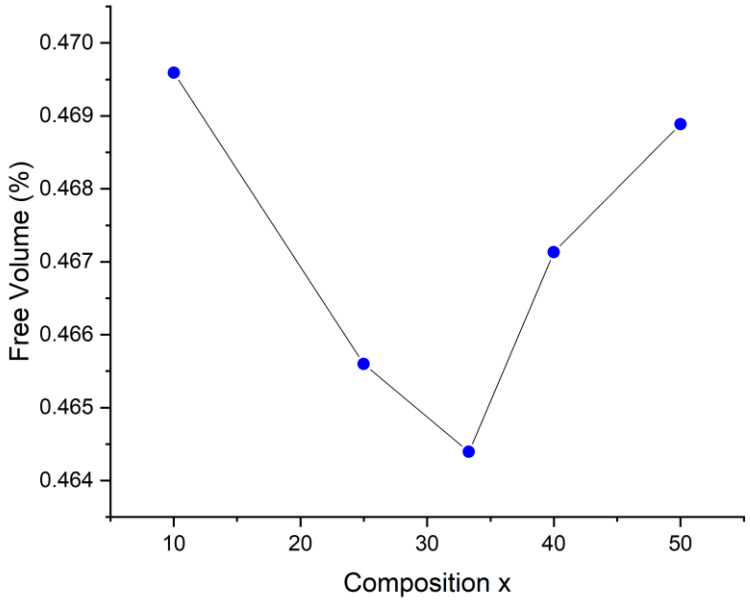

Fig. 3.9 Compositional variation of %V_{free} for the synthesised standard glasses in series (50-*x*) Li_2O: *x*MnO: 50P_2O_5 (*x* = 10.0, 25.0, 33.3, 40.0 and 50.0)

The data show that there is a decrease in %V_{free} with increasing *x*-value from *x* = 10.0 to *x* = 33.3. This indicates that in this range, with increasing *x*-value, the glass becomes more compact through a strengthening of the bonding. This may be attributed to an increase the number of P-O-Mn bridges, as MnO content increases. Above *x* = 33.3, %V_{free} increases with increasing x-value, suggesting a less compact structure and a weakening of bonds. The results are consistent with the compositional variation of T_g shown in **Fig. 3.7**.

It is important to note that the true values of %V_{free} may vary since the ionic radius of Mn^{2+} will vary according to whether it is network forming or network modifying (i.e. its coordination number) and whether it is in high or low spin state. Similarly, the ionic radius of Li^+ ions in coordination numbers 4, 6 and 8, have ionic radii of 0.59, 0.76 and 0.92 Å, respectively [11]. As will be shown later in the molecular dynamics analysis, the coordination numbers vary only by a small amount with composition and the assumption used here of a

constant ionic radius for each ion type appears to be valid. Hence the observed compositional trend in free volume can be considered to be real.

3.2.2.2 Structural analysis

Fig. 3.10 shows the IR spectra of the studied standard glass compositions (50−*x*) Li_2O: *x*MnO: 50P_2O_5 (*x* = 10.0; 25.0; 33.3; 40.0 and 50.0). All peaks are broad, which is typical for a disordered glass system. In this system, several bands are evident and are consistent with metaphosphate chains. All glass compositions show peaks at around 1280 cm^{-1} and 900 cm^{-1}, which are attributed to $(PO_3)^-$ (Q^2 species, metaphosphate) and the P-O-P asymmetric stretch, respectively. In addition, a broad band at around 780 cm^{-1} corresponds to (P-O-P) symmetric vibration of bridging oxygen atoms [12,13]. A weak band characteristic of $(PO_{3.5})^{2-}$ (Q^1 species, pyrophosphate) can be seen at around 1100 cm^{-1}. This may be associated with some of the manganese atoms adopting a network forming role.

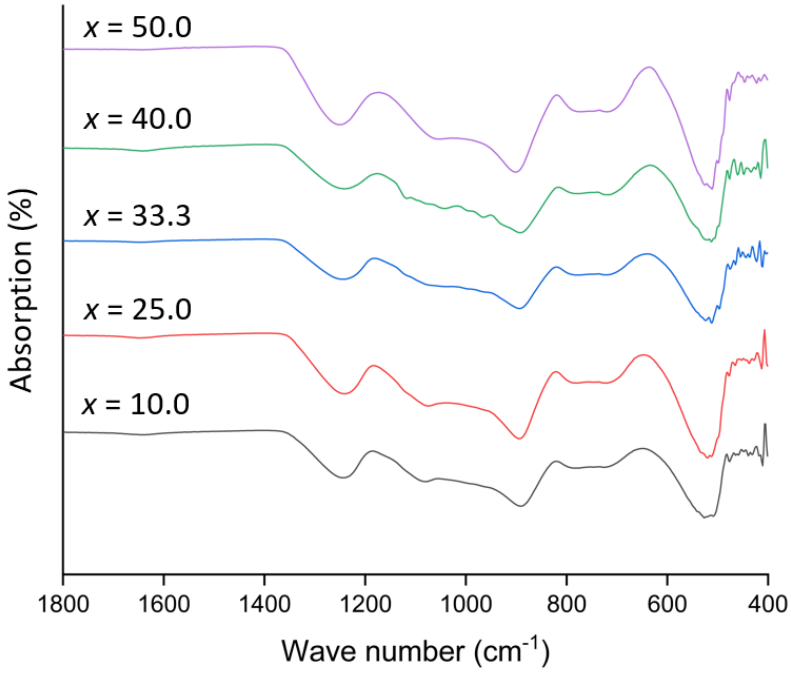

Fig. 3.10 Infrared spectra of standard glass compositions (50-*x*) Li_2O: *x*MnO: 50P_2O_5 (*x* = 10.0; 25.0; 33.3; 40.0 and 50.0).

Fig 3.11 shows the X-ray total pair correlation functions D(r), generated from Ag-Kα radiation (λ = 0.5609 Å) for samples of compositions (50-x) Li_2O: xMnO: 50P_2O_5 (x = 10.0; 25.0; 33.3; 40.0 and 50.0). The profiles are all similar to each other. Each shows a strong broad correlation with a maximum around 1.5 Å, corresponding to the P-O bond in the phosphate tetrahedra [14]. A weaker broad correlation with a maximum around 2.3 Å, is likely attributable to Mn-O, while a stronger peak at around 3.3 Å, corresponds to a combination of P-P, P-Mn and Mn-Mn correlations. The broadness of these profiles makes detailed analysis difficult and therefore further data were collected using synchrotron X-ray radiation at the Diamond facility.

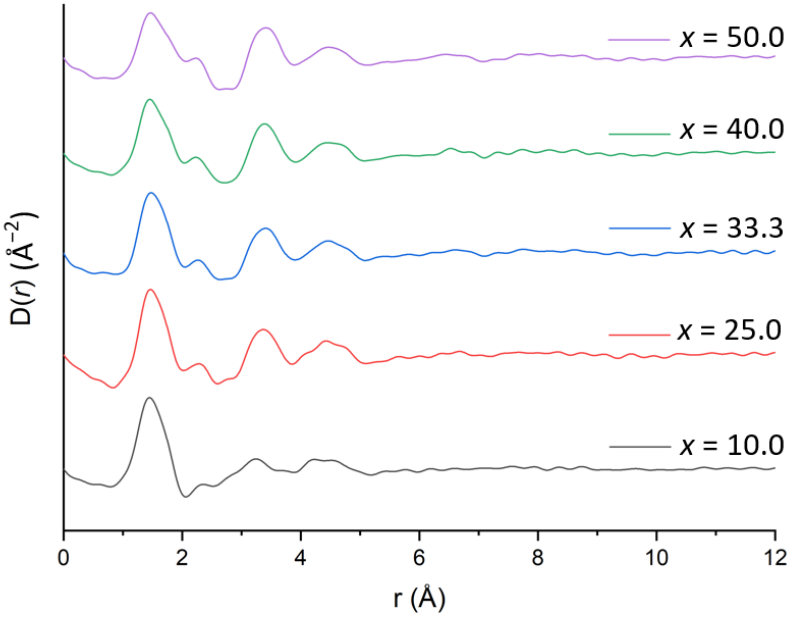

Fig. 3.11 X-ray total pair correlation functions D(r), generated from Ag-Kα radiation (λ = 0.5609 Å) for samples of compositions (50-x) Li_2O: xMnO: 50P_2O_5 (x = 10.0, 25.0, 33.3, 40.0 and 50.0).

Fig. 3.12 shows a comparison of D(r) profiles generated from laboratory and synchrotron radiation sources for the x = 33.3 composition. The resolution of the pair correlations is greatly enhanced in the synchrotron data, due to the larger Q_{max} of 40 $Å^{-1}$.

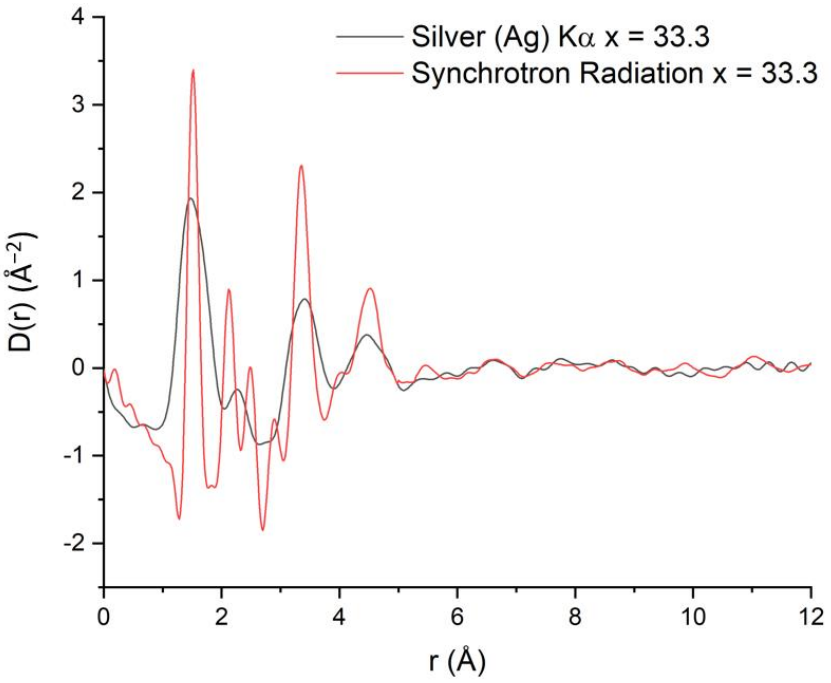

Fig. 3.12 Comparison of D(*r)* profiles for 16.7Li_2O:33.3MnO:50P_2O_5 glass composition from Ag Kα (black) and synchrotron radiation (red).

Fig. 3.13 show the *D*(*r*) profiles derived from synchrotron X-ray diffraction data for glass compositions *x* = 10.0, 33.3 and 50.0. The *D*(*r*) profiles of all glass samples show a strong correlation centred at around 1.52 Å, corresponding the P-O bonds [14]. Unfortunately, the data did not permit separation of the shorter non-bridging P-O bonds from those in P-O-P bridges. The Mn-O correlation is seen here at about 2.11 Å. These peaks are far clearer in the data derived from synchrotron radiation. The intensity of the Mn-O peak compared to that of the P-O peak increases with increasing *x* value, reflecting the increasing Mn content. Li-O correlations (expected at around 2.0 Å) are not readily visible since Li, with only three electrons, makes a relatively small contribution to the X-ray scattering, and the Li-O correlation remains hidden, by the much stronger Mn-O correlation peak nearby. In order to resolve the local structure around lithium atoms, neutron scattering data were collected on the SANDALS diffractometer at the ISIS facility.

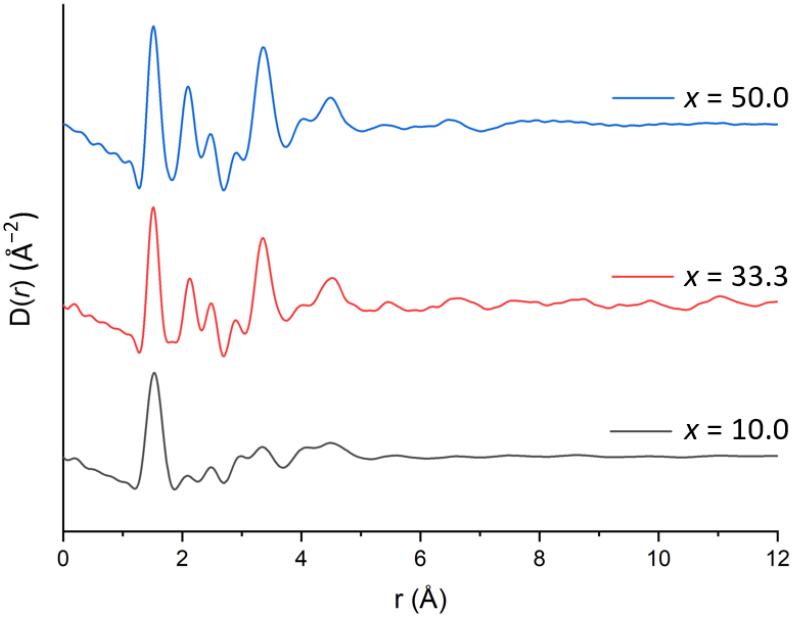

Fig. 3.13 X-ray (collected from Diamond) pair distribution functions *D*(*r*) for (50-*x*) Li_2O: *x*MnO: 50P_2O_5 (*x* = 10.0, 33.3 and 50.0) glass compositions.

D(*r*) total pair functions derived from neutron scattering data for glass compositions *x* = 10.0, 25.0, 33.3, 40.0 and 50.0 are shown in **Fig. 3.14**. As in the X-ray PDFs, all profiles show a strong P-O correlation at about 1.52 Å. Unlike in X-ray scattering, the neutron scattering lengths of lithium and manganese are of the same order of magnitude, −2.22 fm and −3.78 fm, respectively [2] and interestingly both have negative scattering lengths. This means that the impact of correlations involving both these atoms on the data is visible. In the *x* = 50 glass composition (MnO: P_2O_5), the P-O bond correlation is followed by a negative peak with a minimum around 2.10 Å, corresponding to the Mn-O pair correlation. With decreasing value of *x* (increasing Li_2O), the minimum peak gradually shifts to around 2.02 Å, reflecting the larger contribution of Li-O correlations (at around 1.9 Å) to this negative peak. To explore the extent of the Li-O and Mn-O overlap, a set of further measurements were made on samples containing null lithium.

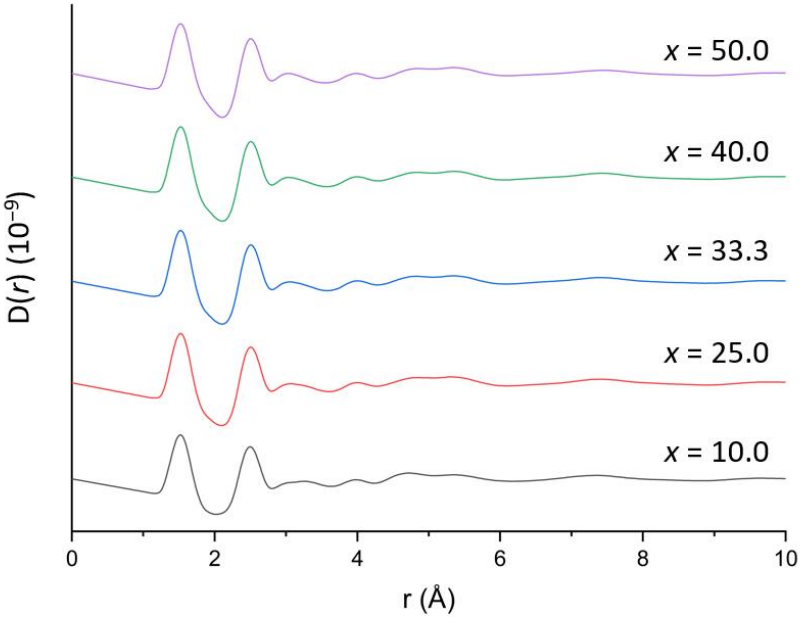

Fig. 3.14 Neutron Scattering Pair Distribution Functions *D*(*r*) for (50-*x*) Li_2O: *x*MnO: 50P_2O_5 (*x* = 10.0, 25.0, 33.3, 40.0 and 50.0) glass compositions.

Comparisons of D(*r*) profiles for the *x* = 25.0 and 33.3 compositions containing natural and null lithium are shown in **Fig. 3.15** and **Fig. 3.16**. Only very small differences are seen between the profiles most noticeably in the large negative peak around 2.1 Å. For null lithium containing samples, this negative peak is shaper, while the corresponding peak is broader and shifted to lower *r*-space at about 2.0 Å in the natural Li sample. The difference in the profiles is more significant in for the *x* = 25 composition reflecting the higher Li content.

(a)

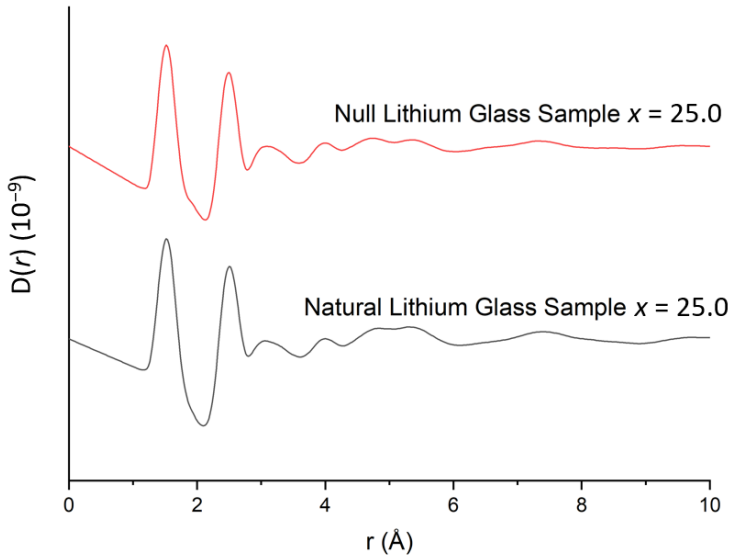

(b)

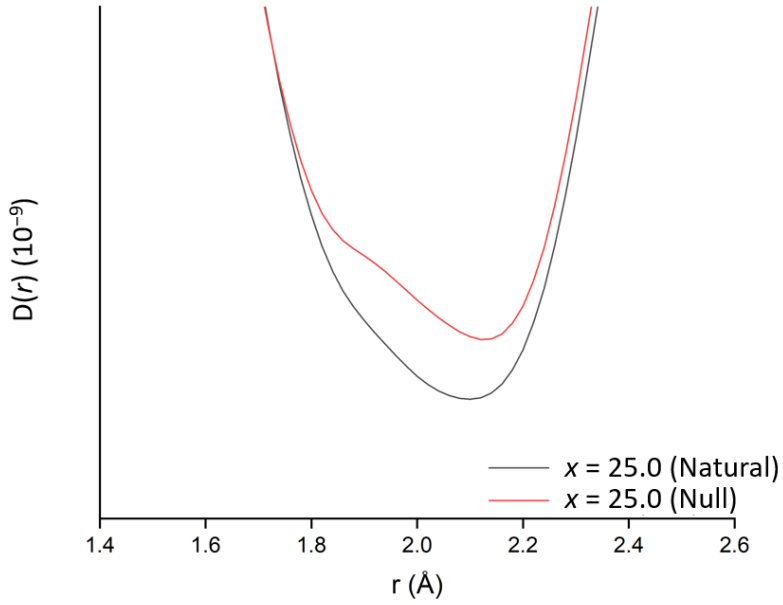

Fig. 3.15 Comparison of D(*r*) profiles for natural and null lithium containing glass samples of $25Li_2O$: 25MnO: $50P_2O_5$ (a), with detail shown in (b).

(a)

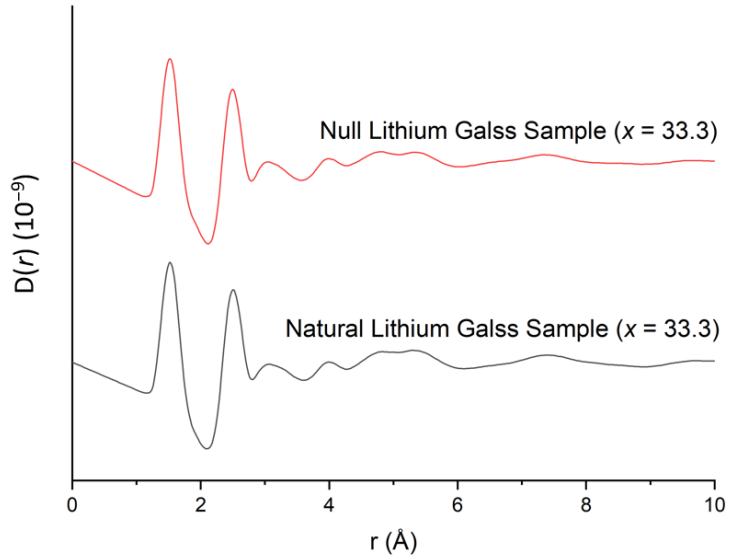

(b)

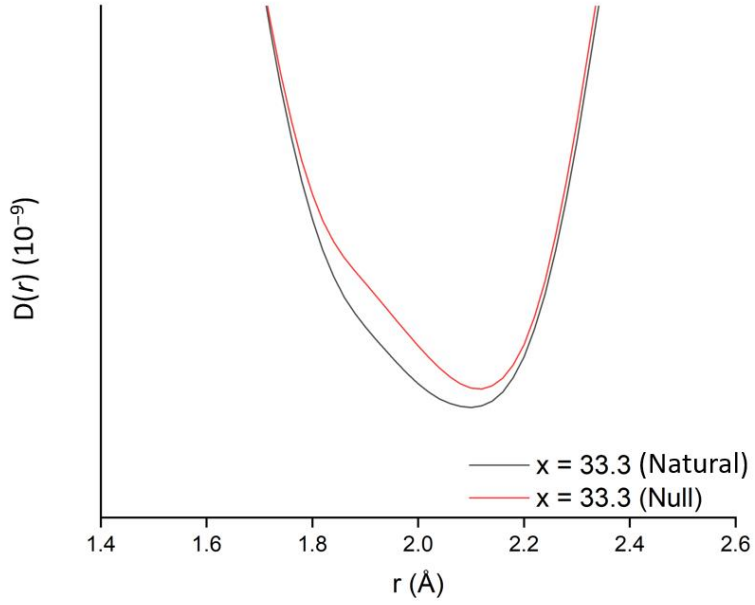

Fig. 3.16 Comparison of D(*r*) profiles for natural and null lithium containing glass samples of 16.7Li_2O: 33.3MnO: 50P_2O_5 (a), with detail shown in (b).

Subtraction of D(*r*) profile for the null Li containing samples from those for the corresponding natural Li samples gives a difference profile dominated by the Li pair correlations (i.e. Li-O, Li-Li, Li-P and Li-Mn) as shown in **Fig. 3.17**. The data show a sharp negative peak at around 1.98 Å for x = 33.3 and 2.00 Å for x = 25.0, corresponding to Li−O pair correlations. This is followed by a positive peak at around 2.6 Å, likely due to Li−Li correlation, overlapping the Li−Mn correlation peak at around 2.8 Å. The Li-P correlations would be expected to result in a negative peak and may be associated with the dip in the profile seen at around 3.1 Å. Among these correlations, the Li−Li distance of 2.6 Å directly indicates the average elementary hopping distance in Li^+ diffusion.

It is very important to choose a suitable melting temperature before the quenching step in the MD simulation. If the melting temperature is not high enough, the simulation process cannot generate the glass and the simulated sample can be partially crystalized. This can be recognised in the D(*r*) profiles as sharper peaks at intermediate and high *r* values, rather than broad distributions for the simulated glass (**Fig. 3.18**). In other words, the D(*r*) profile of the simulated composition can be used to judge whether the melting temperature is high enough to generate a glass when quenched. It should be noted that due to the limits of the simulation, the simulated temperature is significantly higher than observed experimentally. The trend in melting temperature is however similar to the experimental trend, with the x = 33.3 composition requiring the highest simulated melting temperature.

(a)

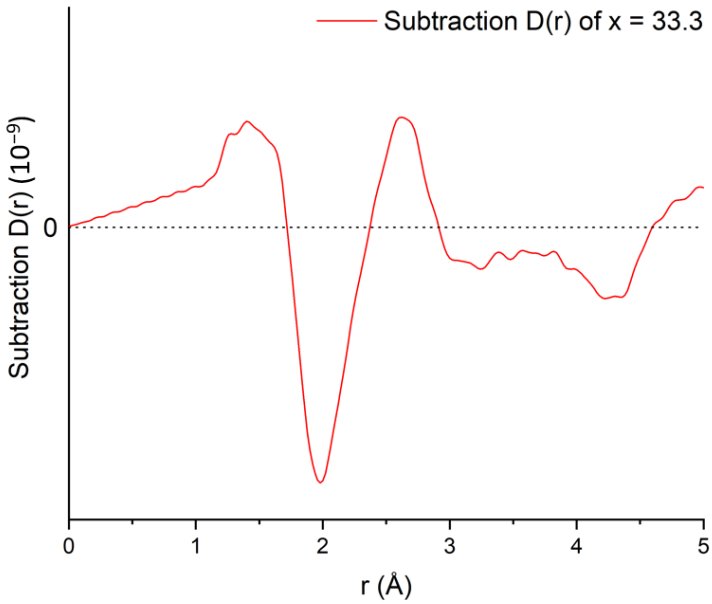

(b)

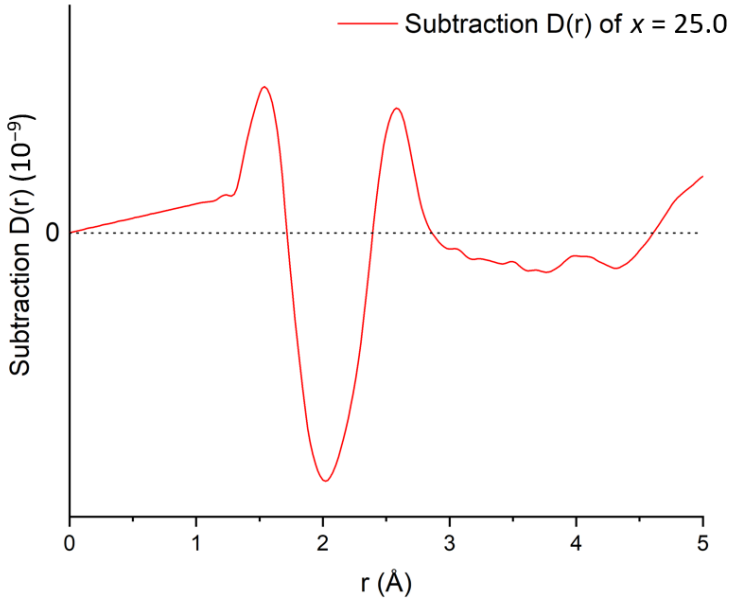

Fig. 3.17 Difference D(*r*) profiles obtained by subtracting the D(r) profile for the null Li containing samples from those for the corresponding natural Li samples (a) composition x = 33.3, (b) composition x = 25.0.

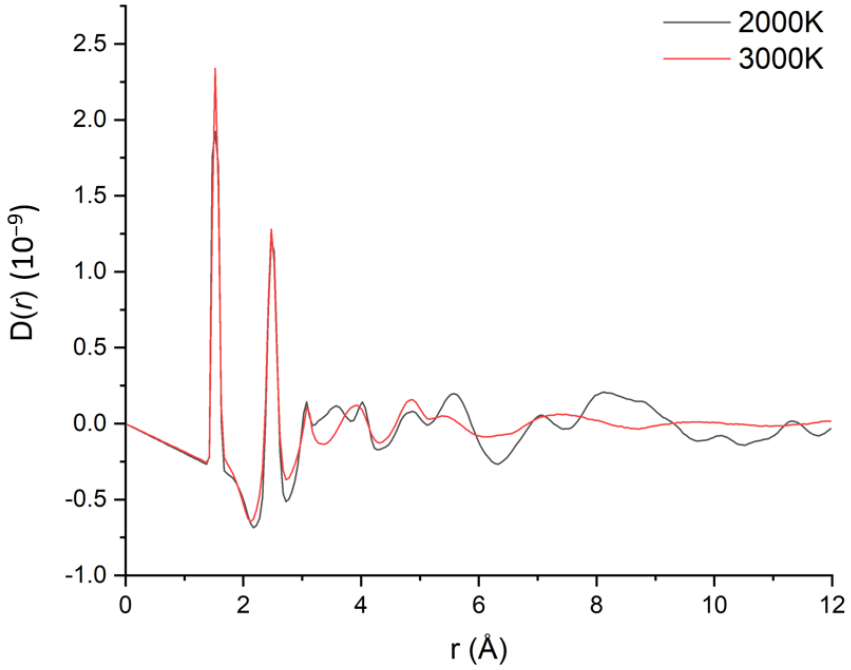

Fig. 3.18 Comparison of simulated neutron scattering D(*r*) profiles for the *x* = 33.3 composition at different simulated melting temperatures (2000 K and 3000 K).

From the figure, we can obviously observe that in the range of 1 Å to 3 Å, the patterns are similar. However, above around 3 Å significant differences are seen, with the higher simulated temperature data generating a much more glass-like profile. The resulting simulated glass compositions show similar neutron scattering D(*r*) profiles patterns (**Fig 3.19**).

While the MD derived neutron *D*(*r*) profiles for glass samples are similar to those for the corresponding compositions found experimentally, including peak location, relative intensity of peak and compositional variations, some differences, such as the shape of peaks, (shaper in the MD derived data, due to the limit of the finite size of the model) are observed. In order to obtain more realistic MD results when compared to the experimental data, a Gaussian convolution was performed on the simulated D(r) profiles:

$$G(x) = \frac{1}{\alpha}\sqrt{\frac{2}{\pi}}\exp\left[-2\left(\frac{x}{\alpha}\right)^2\right] \qquad (3.10)$$

A comparison between the Gaussian broadened simulated D(*r*) profiles with the corresponding experimental data is shown in **Fig. 3.20**.

(a)

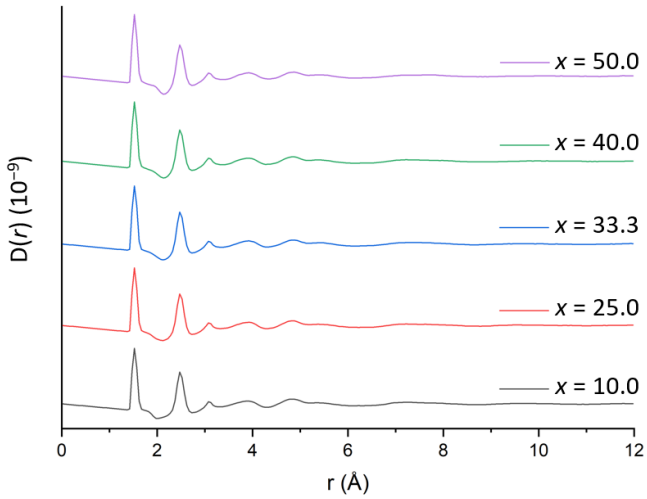

(b)

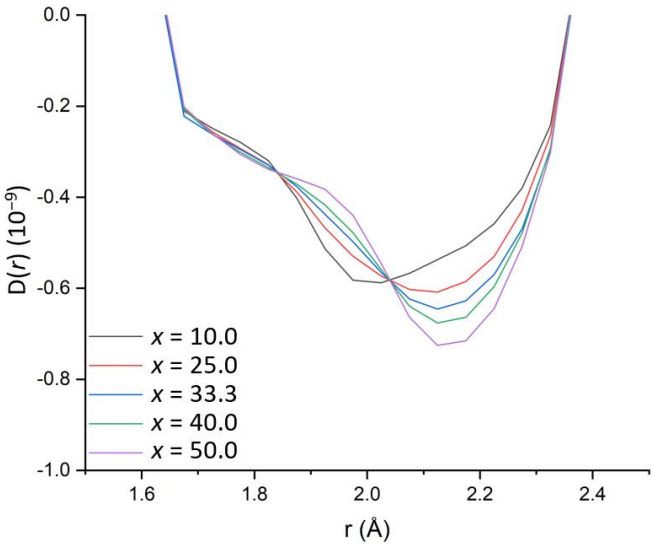

Fig. 3.19 Neutron D(*r*) profiles for glass samples of composition (50−*x*) Li_2O: *x*MnO: 50P_2O_5 (*x* =10.0, 25.0, 33.3, 40.0 and 50.0) generated from MD simulations showing (a) full profile and (b) detail at low *r*-values.

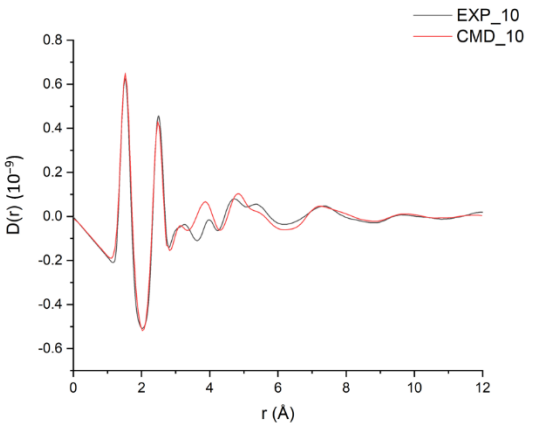
EXP_10
CMD_10
D(r) (10⁻⁹)
r (Å)

(a)

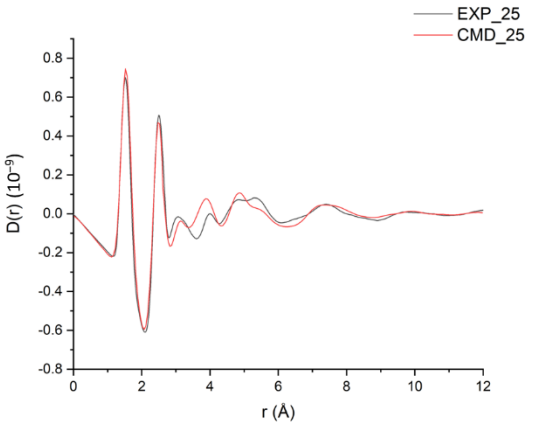
EXP_25
CMD_25
D(r) (10⁻⁹)
r (Å)

(b)

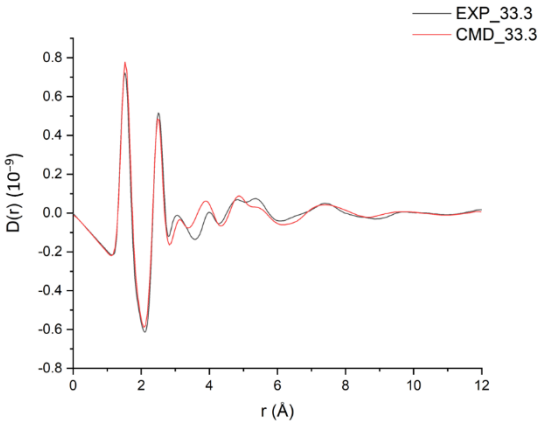
EXP_33.3
CMD_33.3
D(r) (10⁻⁹)
r (Å)

(c)

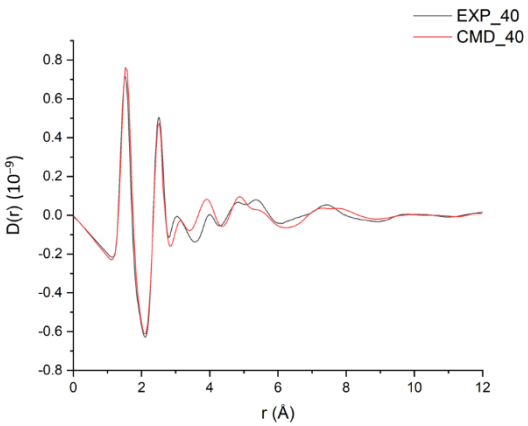
EXP_40
CMD_40
D(r) (10⁻⁹)
r (Å)

(d)

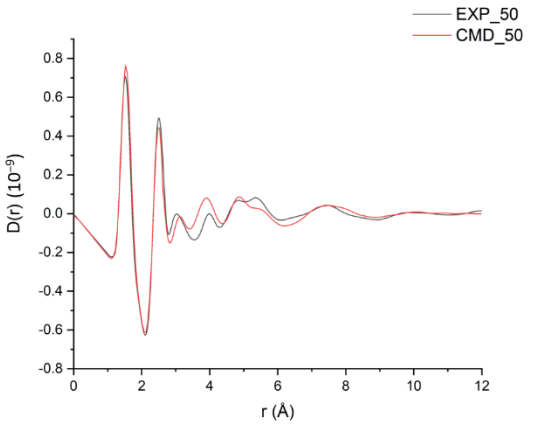
EXP_50
CMD_50
D(r) (10⁻⁹)
r (Å)

(e)

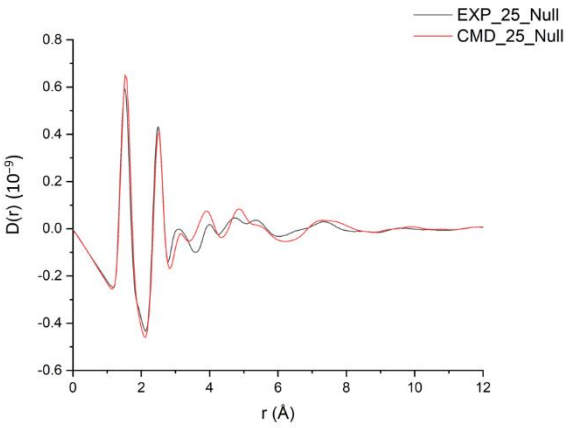
EXP_25_Null
CMD_25_Null
D(r) (10⁻⁹)
r (Å)

(f)

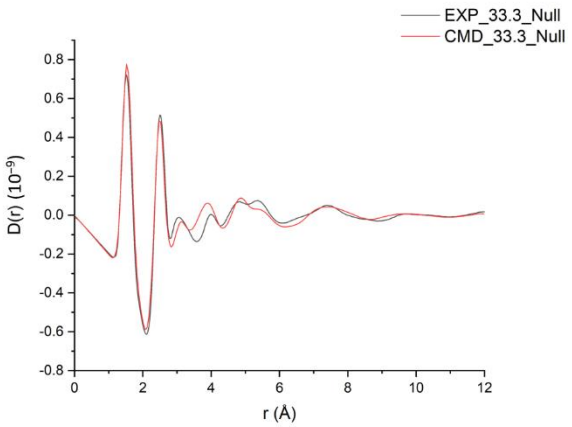

(g)

Fig. 3.20 Comparison of simulated (Gaussian broadened, CMD, red lines) and experimental (EXP, black lines) neutron D(*r*) profiles for glass samples of composition (50−*x*) Li_2O: *x*MnO: 50P_2O_5 (*x* =10.0, 25.0, 33.3, 40.0 and 50.0).

Over the short range up to 3 Å, experimental and simulated patterns are very similar to each other, but above 3 Å some differences appear. In the range 3 to 12 Å, differences in the shape and relative intensity of peaks are observed, but the peak locations roughly match each other. Thus, from the comparison, it can be concluded that the simulated structures reflect the short-range structure of each composition accurately but are less accurate at the intermediate and long range. Nevertheless, very important structural information is contained in the short-range structure, such as coordination number and correlation distances. Selected partial pair correlation functions $g_{ij}(r)$ derived from the MD simulations are shown in **Fig. 3.22**, with the derived coordination numbers and average contact distances given in **Table 3.13**. **Fig. 3.23** shows the selected pair correlation distance distribution for the glass composition 16.7 Li_2O: 33.3MnO: 50P_2O_5. The Li-O, Li-Li, Li-P and Li-Mn partial pair correlations $g_{ij}(r)$ for the *x* = 25.0 composition are shown in **Fig. 3.21**. The correlations show good agreement with the experimental D(*r*) derived by subtracting the null Li data from that of natural Li. It confirms the assignment of the correlations discussed above.

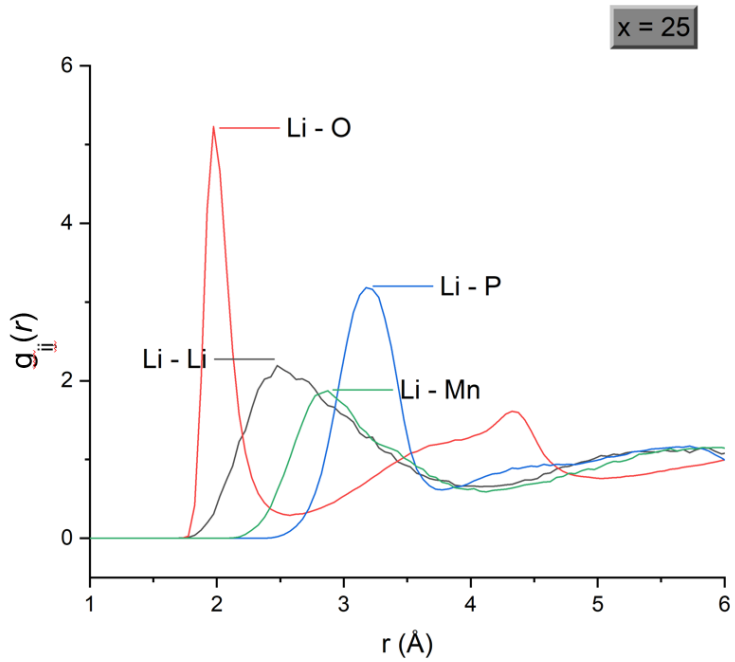

Fig. 3.21 Li-Li, Li-O, Li-P and Li-Mn pair correlations $g_{ij}(r)$ generated from MD simulations for glass samples of composition $25Li_2O$: $25MnO$: $50P_2O_5$ (x = 25.0).

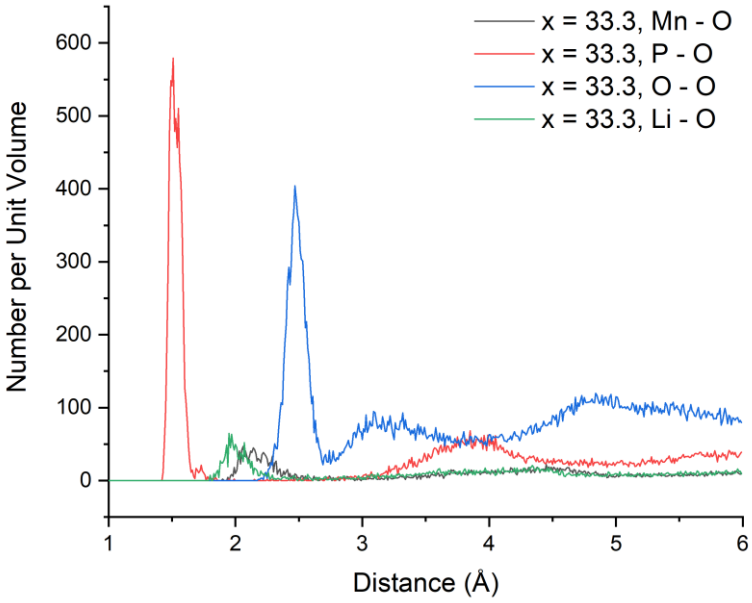

Fig. 3.23 Selected pair correlation distance distribution for the glass composition 16.7 Li_2O: 33.3MnO: $50P_2O_5$

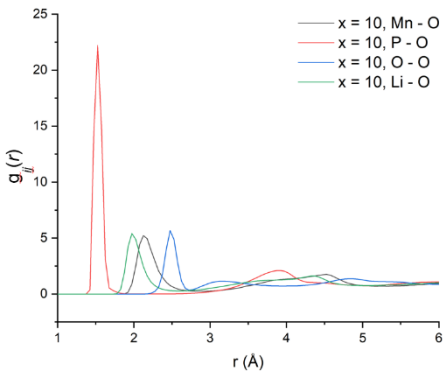

(a)

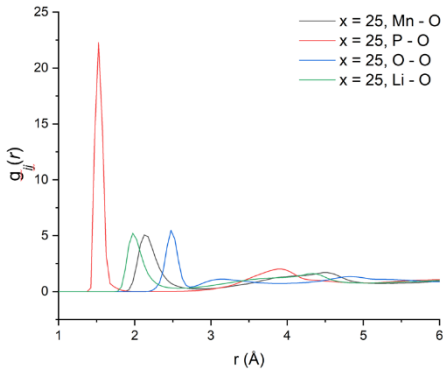

(b)

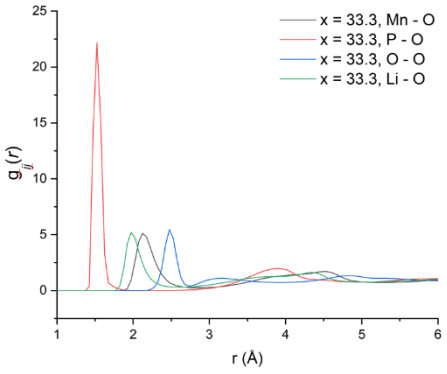

(c)

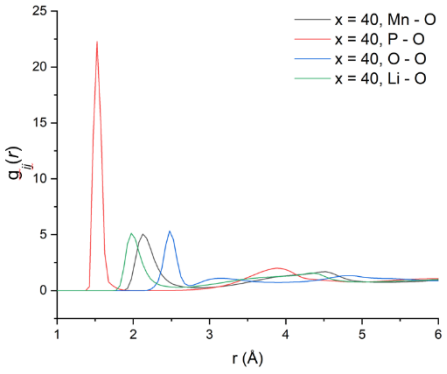

(d)

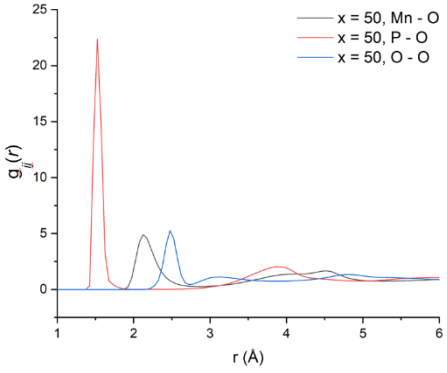

(e)

Fig. 3.22 selected partial pair correlations $g_{ij}(r)$ generated from MD simulations for glass samples of composition (50-*x*) Li_2O: *x*MnO: $50P_2O_5$ (a) *x* = 10.0, (b) *x* = 25.0 (c) *x* = 33.3 (d) *x* = 40.0 and (e) *x* = 50.0.

From the results in **Table 3.13**, we can see that the P-O bond length vary little with composition and combined with the coordination number of around 4, confirms that the simulation models the phosphate tetrahedra reasonably well. The Li-O coordination numbers of around 3.8 suggest predominantly tetrahedral coordination for Li, with a distance range of around 1.96 to 1.99 Å, in good agreement with the data in **Fig. 3.17** (subtracted D(*r*)). The Mn-O distance is seen to decrease up to x = 33.3 and then increase above this. Similarly, the manganese coordination number reaches a minimum at x = 33.3. These trends (**Fig. 3.24**) reflect the changes in free volume and T_g, where the x = 33.3 composition was the most compact structure with the highest T_g.

Table 3.13 Coordination numbers (CN) and selected correlation distances *d* (Å) derived from MD simulations for glasses of compositions (50-*x*) Li_2O: *x*MnO: 50P_2O_5. Uncertainties are estimated at ±0.5%.

Composition *x*	10	25	33.3	40	50
Li−O CN	3.83	3.83	3.78	3.77	/
Li−O *d* (Å)	1.98	1.98	1.96	1.99	/
Mn−O CN	4.80	4.72	4.68	4.69	4.71
Mn−O *d* (Å)	2.16	2.14	2.13	2.14	2.17
P−O CN	4.07	4.10	4.09	4.10	4.11
P−O *d* (Å)	1.50	1.49	1.51	1.50	1.50
O−O CN	/	/	/	/	/
O−O *d* (Å)	2.46	2.47	2.47	2.46	2.44

(a)

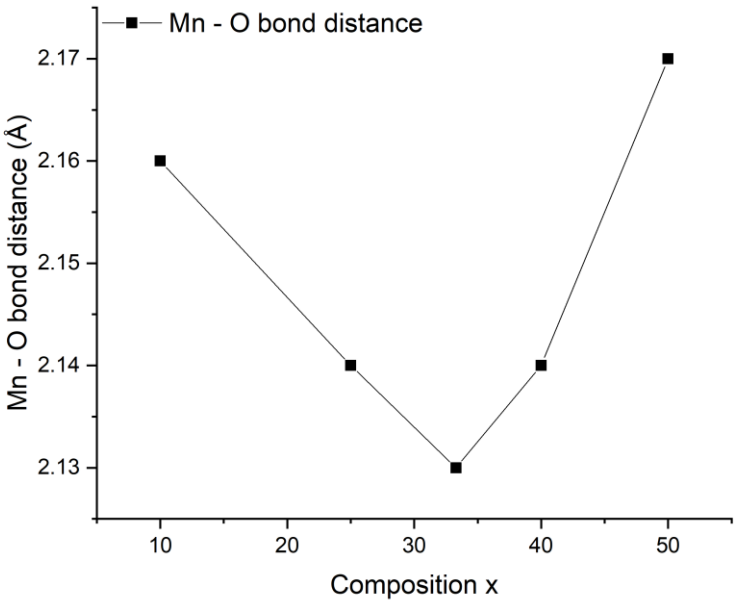

(b)

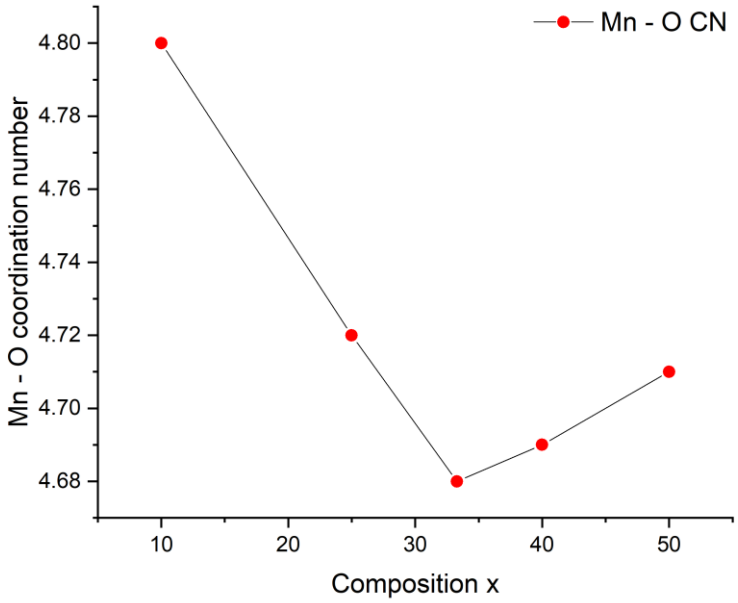

Fig. 3.24 Compositional variation of Mn-O bond distance (a) and coordination number CN (b) for glasses of composition (50-*x*) Li_2O: *x*MnO: 50P_2O_5.

Table 3.14 Manganese coordination number (CN) distributions for studied glass composition (50−*x*) Li_2O: *x*MnO: 50P_2O_5 (*x* =10.0, 25.0, 33.3, 40.0 and 50.0) derived from MD models.

x	CN 2	CN 3	CN 4	CN 5	CN 6	CN 7
10.0	0	0	0.3217	0.5566	0.1217	0
25.0	0	0.0104	0.3576	0.5156	0.1164	0
33.3	0	0.0082	0.3982	0.4976	0.0938	0.0012
40.0	0	0.0097	0.3973	0.4835	0.1085	0.0010
50.0	0	0.0139	0.3655	0.5191	0.1007	0.0008

The coordination numbers for manganese suggest a mixture of 4 and 5 coordinate and possibly 6 coordinate manganese. **Table 3.14** summarises the distribution of manganese coordination numbers for the studied compositions, derived from MD simulations. The data confirm mainly 4, 5 and 6 coordinate manganese.

From the data in **Table 3.14** it is then possible to calculate the phosphate speciation based on the arguments discussed above for the theoretical speciation (**Section 3.2.2.1**). For example, for composition *x* = 33.3 the percentage of manganese in network forming 4 coordinate geometry (**Fig. 3.25**) is approximately 40%. This leaves approximately 60% of the manganese in network modifying 5 and 6 coordination. The total modifying charge would be the sum of the charge from Li^+ and the remaining network modifying Mn^{2+} ions i.e. 1+ 0.6 × 2 = 2.2. If the 4-coordinate manganese is considered to be Q^4 i.e. $(MnO_2)^{2-}$ then it will contribute 0.4 × (−2) = −0.8 to the network charge. The remaining phosphate network would have a total negative charge of − (2.2 − 0.8) = −1.4. This could be achieved with 47% Q^2 and 53% Q^3 phosphate species, $(PO_3)^{1-}$ and $(PO_{2.5})^0$ respectively. Similar calculations can be performed for the other compositions.

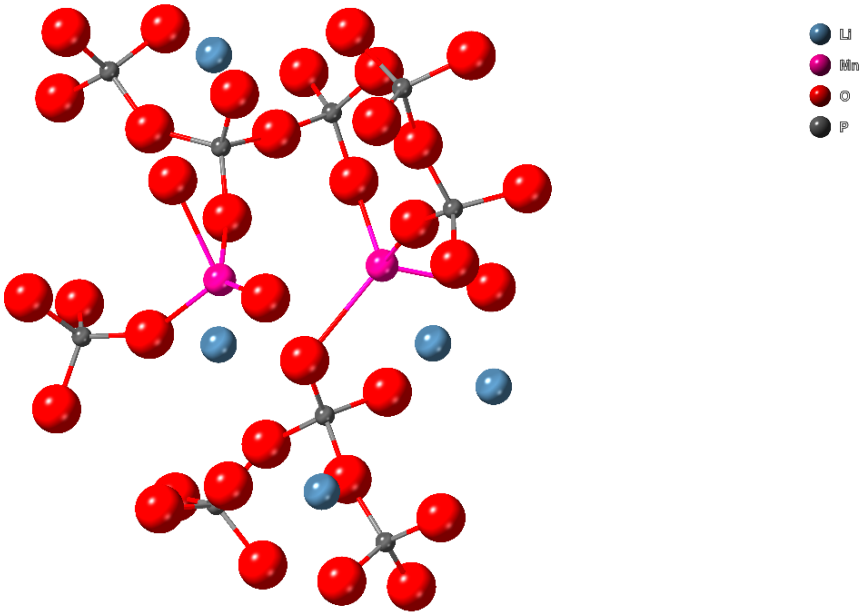

Fig. 3.25 Selected regions of the glass composition x = 33.3 illustrating the Mn 4-coordination geometries.

3.2.2.3 Electrical behaviour

Electrical characterisation of the studied glass compositions was carried out using a.c. impedance spectroscopy. Typical impedance spectra (for x = 25.0 glass composition) are shown in **Fig. 3.26** for three representative temperatures, 434 K (161 °C), 503 K (230 °C) and 573 K (300 °C).

(a)

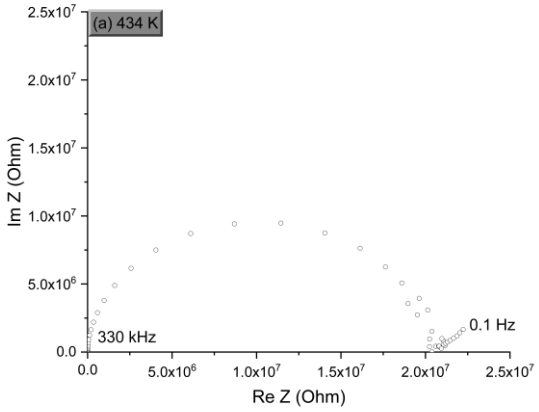

(b)

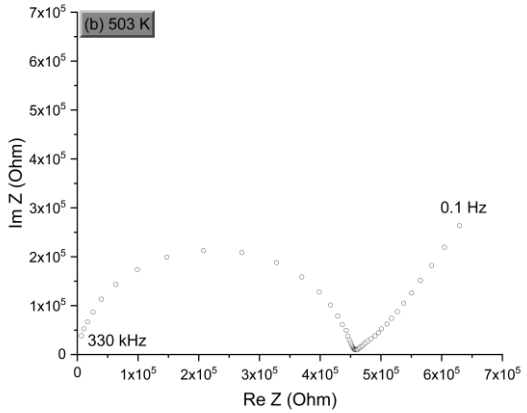

(c)

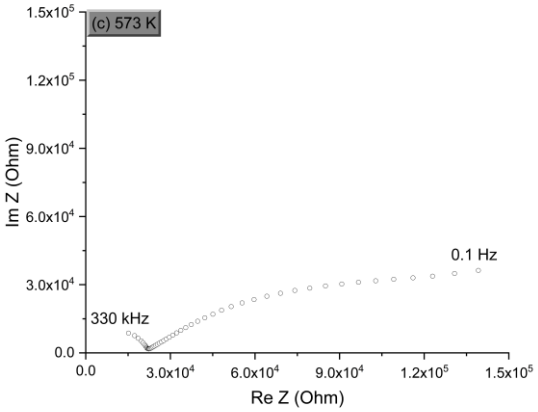

Fig. 3.26 A.C. impedance spectra for $25Li_2O$: 25MnO: $50P_2O_5$ at (a) low, (b) intermediate and (c) high temperatures, 434 K (161°C), 503 K (230°C) and 573 K (300°C), respectively.

At these three temperatures a semicircle or part semicircle is observed at high frequencies corresponding to the bulk resistance of the sample. This is followed by a capacitive spike at lower frequencies due to the blocking electrodes, which is consistent with conductivity being predominantly ionic in nature in this system. At higher temperatures the bulk semi-circle starts to move out of the frequency window and only a part semi-circle is observed. Curvature in the blocking spike may be attributed to surface roughness effects. At all temperatures for all studied samples in the (50−x) Li_2O: xMnO: $50P_2O_5$ (x = 10.0, 25.0, 33.3, 40.0 and 50.0) system, the a.c. impedance spectra are similar, with the exception of the x = 50.0 composition, due to the lack of lithium ion carriers. Thus, the spectra of this composition were poorly resolved with very high resistances and it was not possible to extract reliable value.

Arrhenius plots of conductivity for the x = 10.0, 25.0, 33.3, 40.0 compositions, are shown in **Fig 3.27.** The reported data correspond to the first cooling cycle.

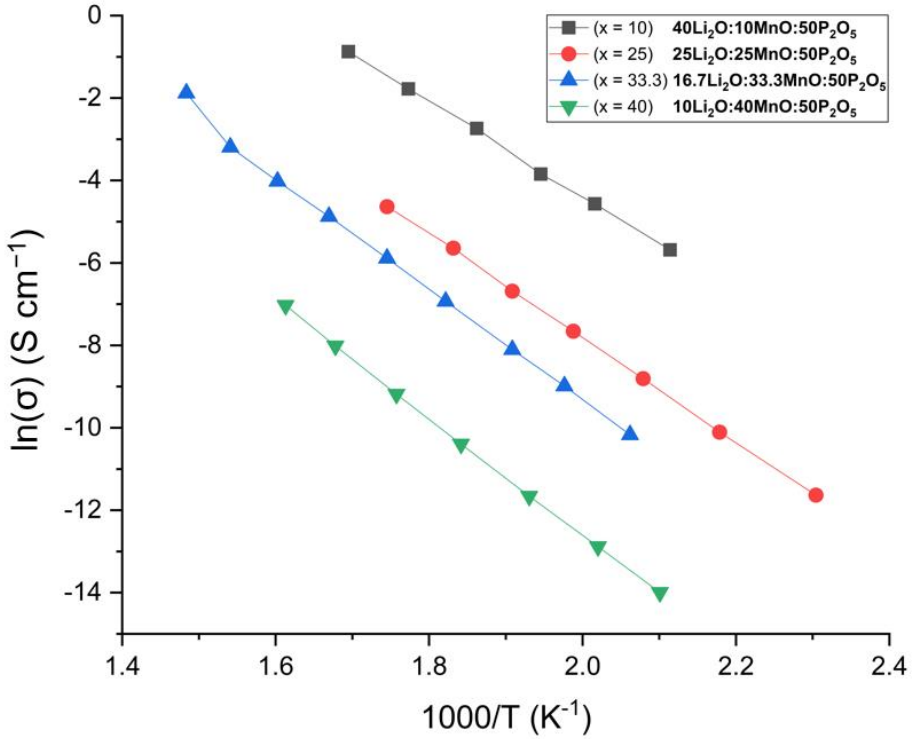

Fig. 3.27. Arrhenius plots of total conductivity for selected glass compositions (x = 10.0, 25.0, 33.3, and 40.0) in the (50-x) Li_2O: xMnO: $50P_2O_5$ system

Linear Arrhenius behaviour is seen for all compositions. Out of all compositions investigated, the sample with the lowest level of substitution (x = 10.0) and the highest lithium ion concentration exhibits the highest conductivities over the whole temperature range studied. This shows that the carrier density plays an essential role in the conductivity of the studied glasses.

Table 3.15 summarises the derived electrical parameters for the studied compositions, with the compositional variation at 200 °C and 300 °C shown in **Fig. 3.28**. Conductivity σ at both 200 °C and 300 °C decreases with increasing substitution level (x). In fact, this trend exists in all the temperature regions.

Table 3.15 Derived electrical parameters for selected glass compositions in the (50−x) Li_2O: xMnO: 50P_2O_5 system in (x = 10.0, 25.0, 33.3, and 40.0) (Estimated uncertainty is ±5%).

Composition (x)	$\sigma_{200°C}$ / σ_{473K} (S cm^{-1})	$\sigma_{300°C}$ / σ_{573K} (S cm^{-1})	Activation Energy E_a (eV)
10	7.20×10^{-6}	4.08×10^{-4}	1.00
25	2.02×10^{-7}	1.69×10^{-5}	1.09
33.3	3.71×10^{-8}	4.84×10^{-6}	1.28
40	1.39×10^{-9}	2.21×10^{-7}	1.25

As shown in **Fig. 3.29**, the activation energy E_a of the studied composition increases with increasing x value before it reaches a maximum (at x = 33.3) and starts to decrease. The trend of E_a follows that of T_g and of free volume and Mn-O coordination number and bond length as discussed above. All of them reflect that the glass composition x = 33.3 has the most compact structure.

(a)

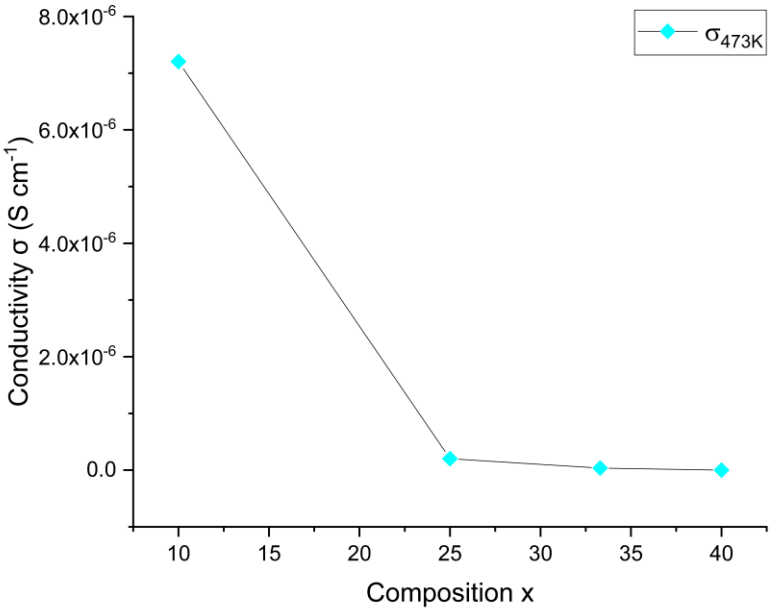

(b)

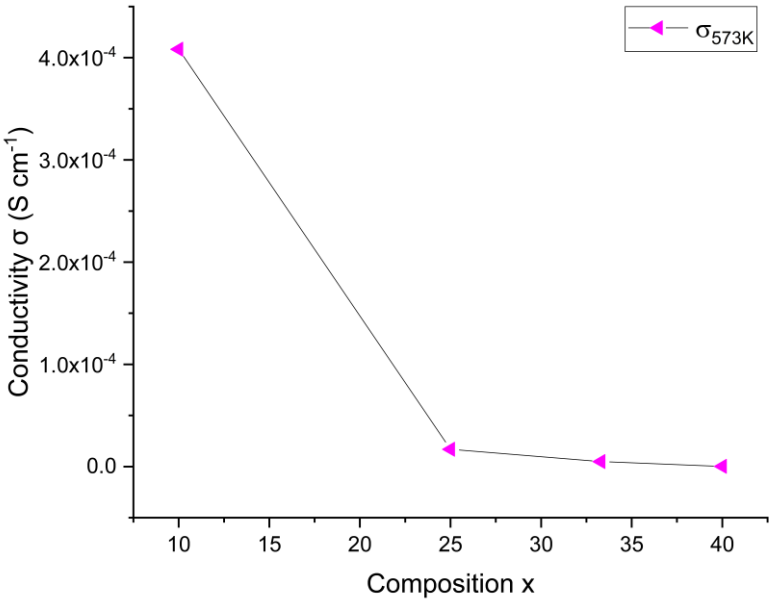

Fig. 3.28 Compositional variation of total conductivity at (a) 473K (200 °C) and (b) 573K (300 °C) for compositions in the (50-*x*) Li_2O: *x*MnO: 50P_2O_5 glass system.

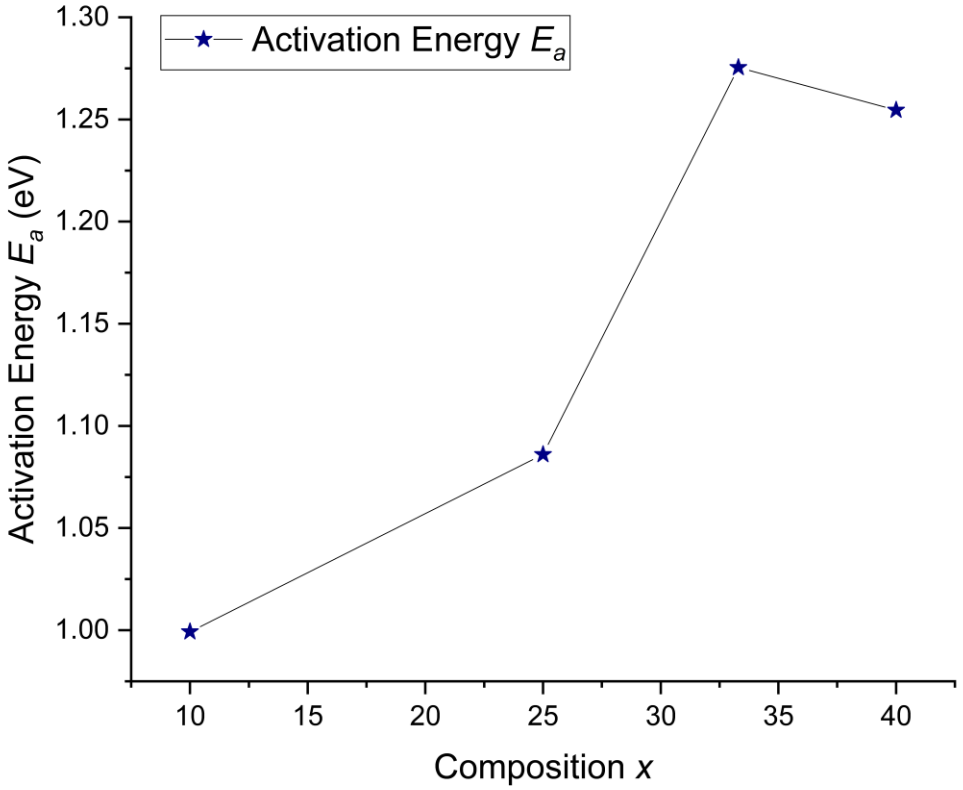

Fig. 3.29 Compositional variation of activation energy in in (50-*x*) Li_2O: *x*MnO: 50P_2O_5 system.

3.3 Conclusions

Glasses were readily formed in the (50-*x*) Li_2O: *x*MnO: 50P_2O_5 system between *x* = 10.0 and *x* =50.0. These glasses show a maximum in T_g and a minimum in free volume at *x* = 33.3 indicative of a change in the role of manganese in this system as a function of composition. From MD simulations of neutron pair distribution functions of the studied glass compositions, manganese was found to mainly adopt 4, 5 and 6 coordinate geometries, with the average coordination number showing a minimum corresponding to the maximum in T_g and the minimum in free volume. The results show an increase in the percentage of network forming manganese species with increasing *x*-value up to *x* = 33.3, with higher *x*-value compositions showing increasingly greater network modifying behaviour for Mn. Thus, although these glasses are technically metaphosphates in terms of their stoichiometry in reality, the phosphate species are likely to be a mixture of Q^2 and neutral Q^3 species to maintain electroneutrality.

Since the glass formula involves the substitution of 2 Li^+ ions by a single Mn^{2+} cations, fewer cross-links between the phosphate chains occur as *x* increases and would be expected to cause a weakening of the phosphate network, throughout the compositional range. This only becomes evident at higher *x*-values. Thus, the system involves two competing mechanisms, one which increases T_g and the other that decreases T_g, leading to a transition at $x = 33.3$, where the structure is most compact. The ionic conductivity of the glasses decreases with increasing *x*-value due to the decrease in the total Li content.

3.4 References

1 Laeter, J. R. D. *et al.* Atomic Weights of the Elements: Review 2000 (IUPAC Technical Report). *Pure and Applied Chemistry* **75**, 683–800 (2003).

2 Sears, V. F. Neutron scattering lengths and cross sections. *Neutron News* **3**, 26 (1992).

3 Larson, A. C. & Dreele, R. B. V. General Structure Analysis System (GSAS). 86-748 (Los Alamos National Laboratory, 2004).

4 Soper, A. K. Report RAL-TR-2011-013. (Rutherford Appleton Laboratory Technical, 2011).

5 Todorov, I., Smith, W., Trachenko, K. & Dove, M. DL_POLY_3: new dimensions in molecular dynamics simulations via massive parallelism. *Journal of Materials Chemistry* **16**, 1911–1918 (2006).

6 Todorov, I. & Smith, W. *THE DL_POLY_ 4 USER MANUALS*. (STFC Daresbury Laboratory, 2015).

7 Pedone, A., Malavasi, G., Menziani, M. C., Cormack, A. N. & Segre, U. A new self-consistent empirical interatomic potential mode for oxides, silicates and silica-based glasses. *The Journal of Physical Chemistry B* **110**, 11780-11795 (2006).

8 Nadarajah, A. BSc thesis, Queen Mary University of London, (2013).

9 Moutataouia, M., Lamire, M., Saadi, M. & Ammari, L. E. Dilithium manganese(II) catena-tetrakis(polyphosphate), $Li_2Mn(PO_3)_4$. *Acta Cryst.* **E70**, i1 (2014).

10 Kanwal, N. *et al.* Structure and solubility behaviour of zinc containing phosphate glasses. *journal of Materials Chemistry B* **3**, 8842-8855 (2015).

11 Shannon, R. D. New relation between ionic radii, bond length, and bond strength. *Acta Crystallogr.* **A32**, 751-767 (1976).

12 Muresan, D. *et al.* Structural investigation of calcium-soda-phosphate glasses with small content of silver oxide. *Journal of Optoelectronics and Advanced Materials* **8**, 558-560 (2006).

13 Schwarz, J., Ticha, H., Tichy, L. & Mertens, R. Physical properties of PbO-ZnO-P_2O_5 glasses. I. Infrared and Raman spectra. *Journal of Optoelectronics and Advanced Materials* **6**, 737-746 (2004).

14 Gamoke, B., Neff, D. & Simons, J. Nature of PO Bonds in Phosphates. *The Journal of Physical Chemistry A* **19**, 5677-5684 (2009).

Chapter 4 Structure and Conductivity in Composition (60-*x*) Li_2O: *x*MnO: 40P_2O_5

4.0 Introduction

The results from Chapter 3 suggested that manganese acts as a network intermediate in the Li_2O-MnO-P_2O_5 system, with the role of manganese changing with composition. However, total conductivity decreased with decreasing Li_2O content. In this chapter compositions with higher Li_2O content are investigated. Compositions of general formula (60 − *x*) Li_2O: *x*MnO: 40P_2O_5 (*x* = 10, 15, and 20), were synthesised and studied. These glasses compositions were based on a previous study [1] in the Abrahams group. In that work conductivities of around 10^{-3} S cm^{-1} were attained at 300 °C, but detailed structural characterisation was not performed. Here the structure and thermal behaviour of these glass compositions are characterised for the first time and the electrical measurements repeated.

4.1 Experimental

4.1.1 Synthesis

Glass samples of general composition (60−*x*) Li_2O: *x*MnO: 40P_2O_5 (**Table 4.1**) were prepared using appropriate amounts of reagent-grade Li_2CO_3 (BDH, 99.9%), MnO (BDH, 99.6%), and $NH_4H_2PO_4$ (May & Baker, 98.0%). For the neutron scattering PDF analysis Li_2CO_3 isotopically enriched in ^{6}Li (American Elements, $^6Li_2CO_3$, 94.61%; $^7Li_2CO_3$, 5.39%) was mixed with naturally abundant Li_2CO_3 (^{7}Li 92.41%; ^{6}Li, 7.59% [2]) to obtain “null lithium” glasses. The glass synthesis was carried out as previously described in Chapter 3 as summarised in **Table 4.2**.

Table 4.1 Synthesised glass compositions in the system (60−*x*) Li_2O: *x*MnO: 40P_2O_5.

Composition of (60−*x*) Li_2O: *x*MnO: 40P_2O_5	Values of *x*
60Li_2O: 40P_2O_5	0
50Li_2O: 10MnO: 40P_2O_5	10
45Li_2O: 15MnO: 40P_2O_5	15
40Li_2O: 20MnO: 40P_2O_5	20
35Li_2O: 25MnO: 40P_2O_5	25
30Li_2O: 30MnO: 40P_2O_5	30

Table 4.2 Summary of preparation parameters for all glass samples of the composition (60−*x*) Li_2O: *x*MnO: 40P_2O_5 described in this work, where "Li Type" indicates whether the samples contained naturally abundant Li ("natural") or "null lithium". "Quenched" indicates that the melts were quenched in air onto stainless steel.

Value of *x*	Li Type	Reaction 1		Reaction 2		Reaction 3		
		T (°C)	**Time (h)**	**T (°C)**	**Time (h)**	**T (°C)**	**Time (h)**	**Cooling Procedure**
15	null	300	0.5	650	1	1100	1	quenched
30	natural	300	0.5	650	1	1100	1	quenched
25	natural	300	0.5	650	1	1100	1	quenched
20	natural	300	0.5	650	1	1100	1	quenched
15	natural	300	0.5	650	1	1100	1	quenched
10	natural	300	0.5	650	1	1100	1	quenched
0	natural	300	0.5	650	1	1100	1	quenched

X-ray powder diffraction showed that only compositions (*x* = 10, 15 and 20) were synthesised successfully as glasses, with composition *x* = 20 showing a small degree of crystallisation. Thus, the *x* = 15 composition was selected to be synthesised using "null lithium" for neutron studies, as it was the highest *x*-value composition that showed no crystallisation.

4.1.2 Density measurements

Density measurements were performed by helium gas displacement (AccuPyc 1330 Pycnometer). Measurements were repeated at least five times and average values used. Density values are required for the calculation of free volume which is an essential measure of the structure compactness which can influence Li^+ mobility. In addition, density values are required for accurate data correction for PDF measurements and for the MD simulations.

4.1.3 Infrared spectroscopy

Infrared spectroscopy was carried out on a Perkin Elmer: Spectrum 65 FT-IR Spectrometer in the range 600-1500 cm^{-1} with a resolution of 32 cm^{-1}. The measurements were made on powdered samples and all spectra were measured at room temperature. This measurement was used to detect the approximate distribution of phosphate Q-species in the studied glasses and can be compared to the results of the glass systems in Chapter 3.

4.1.4 Thermal analysis

Differential scanning calorimetry (DSC) was used to investigate the thermal behaviour of glass and crystalline compositions, using a Perkin Elmer DSC-7. Samples of approximate mass 30 mg were subjected to controlled heating and cooling cycles. Thermograms were collected in air over the temperature range 20 °C to 1000 °C with heating and cooling rates of 20 °C min^{-1}. DSC was applied to obtain the key temperatures of T_g, T_c and T_m, which give information on the network strength and the workability of the glass.

4.1.5 X-ray diffraction

Standard X-ray powder diffraction data were collected on a PANalytical X'Pert Pro diffractometer in flat plat θ/θ geometry using Ni filtered Cu-Kα radiation (λ = 1.5418 Å), in the 2θ range 5-70°, in steps of 0.033° with an effective count rate of 100 s per step. In the case of glass samples these measurements were used to confirm the amorphous nature. For X-ray scattering analysis, data were collected on PANalytical Empyrean diffractometer using Rh-filtered Ag-Kα radiation (λ = 0.5609 Å). Data were collected from 3-148° 2θ in θ/θ geometry

with samples mounted in 1 mm diameter Kapton capillaries. Data were collected in steps of 0.033° 2θ, with a scan time of 440 s per step. For each sample, five scans were summed to give the final data. Data sets for an empty Kapton capillary and the empty instrument were collected under the same conditions for data correction purposes, which was carried out using the GudrunX software [3]. In addition, further X-ray diffraction data were collected on the XPDF I51-1 diffractometer at the Diamond facility, Rutherford Appleton Laboratory. For these experiments, samples were loaded into 1 mm diameter silica glass capillaries. A wavelength of 0.1617 Å (E = 76.69 keV) was used with a large area detector (Q_{max} = 40 Å^{-1}) with count times of 10 min for each sample. Data were analysed in the same way as the laboratory X-ray data using GudrunX [3]. Combined with results from GudrunN, PDFs generated from X-ray data can provide some basic information, such as bond lengths.

4.1.6 Neutron scattering

Neutron scattering data were collected on SANDALS diffractometer at the ISIS facility, Rutherford Appleton Laboratory. Samples were loaded as large glass chunks into thin walled 11 mm diameter vanadium cans. Total data collections of around 1800 μA h were made for each sample. Data sets for an empty can and empty instrument were collected for data correction purposes and data for a vanadium/niobium rod used for normalisation. Data correction was carried out using the Gudrun software [3]. Dimensions of the loaded sample cans are given in **Table 4.3**. Like the results of X-ray PDFs, neutron PDFs can offer experimental information about the structure of studied glasses, with the added advantage of greater Q-range yielding more accurate PDFs compared to those from X-ray scattering and the enhanced contribution of lithium to the neutron data.

Table 4.3 Dimensions of the loaded cans used to collect neutron data on compositions in the (60−*x*) Li_2O: *x*MnO: 40P_2O_5 (*x* = 10, 15, and 20) system. "Li Type" indicates whether the samples contained naturally abundant Li ("natural") or "null lithium".

Composition (*x*)	Li Type	Diameter (mm)	Height(mm)	Weight (g)
15	null	11	54	6.21
20	natural	11	53	6.70
15	natural	11	52	6.11
10	natural	11	54	6.94

4.1.7 Molecular dynamics (MD) simulations

MD simulations were performed using DL_POLY version 4.08 [4,5] on Apocrita (a part of the MidPlus consortium) for selected compositions *x* = 10, 15 and 20. Morse type pair potentials were used to calculate the potential energy and its derivative. The size of the model was around 11000 atoms. MD simulations were performed with a constant temperature (NPT) ensemble. The equations of motion were integrated using the Nosé-Hoover algorithm [6]. Simulations were carried out in steps of 0.01 ps over a total of 20000 ps. A final simulated melting temperature of 2000 K was used for all the selected compositions. After 20000 ps a simulated quench to 300 K was performed to obtain the glasses.

4.1.8 Electrical measurements

Conductivity and related activation energy are very important properties for electrode materials, which can be obtained through electrical measurements. Only one glass sample and one partial crystalized sample (**Table 4.3**) were selected as typical examples. For these sample, pellets were produced by pouring the melt into a stainless-steel cylindrical mould. The resulting pellet was polished using a selection of abrasive papers (1200 to 4000 grit). Finally, silver film electrodes were applied to the polished faces of sample pellets.

Table 4.4 Parameters for pellets used in electrical measurements.

Composition	x	Bottom Area (mm^2)	Height (mm)	T_{max} (°C)	T_{min} (°C)
$45Li_2O$: 15MnO: $40P_2O_5$	15	33.05	0.83	293	212
$60Li_2O$: $40P_2O_5$	0	77.95	0.82	282	197

Electrical measurements were carried out using a computer controlled Autolab PGSTAT302N frequency response analyser in the frequency range from 0.1 to 330 kHz in air with an ac signal amplitude of 100 mV. Experiments were carried out at stabilised temperatures during controlled heating and cooling cycles. The measurements on cooling were performed to investigate possible thermal hysteresis. To avoid sample softening, the highest measurement temperature was about 30 to 60 °C below the corresponding glass transition temperature. The lowest measurement temperature was around 160 to 200 °C. **Table 4.4** summarises the pellet parameters and corresponding measurement conditions of the studied samples.

4.2 Results & discussion

4.2.1 General results

After several synthesis experiments, only two compositions (x = 10 and 15) were found to produce pure glasses. The x = 20 composition, although visibly glass-like, was found to show partial crystallisation, while the x = 25 and x = 30 compositions were visibly crystalline. The x = 0 composition also showed partial crystallisation. The results are summarised in **Table 4.5**.

As seen in the (50−x) Li_2O: xMnO: $50P_2O_5$ in **Chapter 3**, the glass samples in the (60−x) Li_2O: xMnO: $40P_2O_5$ system were transparent and purple in colour. After grinding samples to fine powders, the samples had a light pink colouration. The partial crystalized glass $60Li_2O$: $40P_2O_5$ was transparent and colourless. However subsequent X-ray analysis (see below) revealed partial crystallisation. The results are consistent with those of Kontor [1], who also found a glass forming limit of x = 15 in this system. **Fig. 4.1**. shows images of the crystallised glasses. There is a striking comparison between these and typical pure glass samples.

Table 4.5 Synthesis results for all the compositions, where G, PCG and C represent glass, partially crystalized glass and crystallised respectively, and "Li Type" indicates whether the samples contained naturally abundant Li ("natural") or "null lithium".

Composition of $(60-x)$ Li_2O: xMnO: $40P_2O_5$	Values of x	Li Type	G/PCG/F
$60Li_2O$: $40P_2O_5$	0	natural	PCG
$50Li_2O$: $10MnO$: $40P_2O_5$	10	natural	G
$45Li_2O$: $15MnO$: $40P_2O_5$	15	natural	G
$40Li_2O$: $20MnO$: $40P_2O_5$	20	natural	PCG
$35Li_2O$: $25MnO$: $40P_2O_5$	25	natural	C
$30Li_2O$: $30MnO$: $40P_2O_5$	30	natural	C
$45Li_2O$: $15MnO$: $40P_2O_5$	15	null	G

X-ray powder diffraction patterns for the synthesised compositions in the system $(60-x)$ Li_2O: xMnO: $40P_2O_5$ (x = 0 10, 15 and 20) are shown in **Fig. 4.2**. The patterns of the x = 10 and 15 compositions each show a single broad halo centred at approximately 25° 2θ, characteristic of an amorphous solid with no indication crystallisation as shown by the absence of Bragg peaks. The results confirm that glass formation was successful for these two compositions. The diffraction pattern of the x = 20 composition shows a similar pattern to those of x = 10 and x = 15, except that some weak Bragg peaks are also observed indicating a small degree of crystallisation occurred.

For the x = 0 composition many sharp Bragg peaks are observed in the diffraction pattern confirming partial crystallisation. From the synthesis results, we can conclude that under the quenching conditions used in this project, only compositions in the range $10 \leq x \leq 15$, in the system $(60-x)$ Li_2O: xMnO: $40P_2O_5$ can be successfully prepared as pure glasses, although even at x = 20 the majority of the sample is glassy.

(a) **(b)**

Fig. 4.1 Crystallised samples (a) x = 30 and (b) x = 25 in the system (60−x) Li_2O: xMnO: $40P_2O_5$

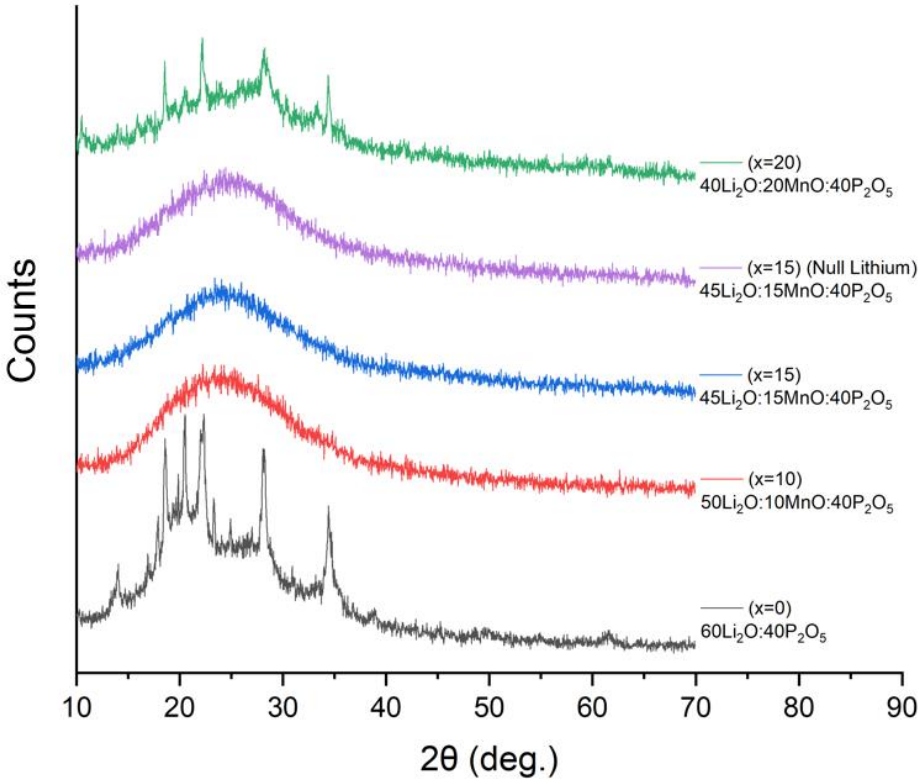

Fig. 4.2 XRD patterns for synthesised compositions (60−x) Li_2O: xMnO: $40P_2O_5$ (x = 0, 10, 15, 20).

The thermal event temperatures for the $x = 10$ to $x = 20$ compositions are listed in **Table 4.6**, with the compositional variation of T_g, T_c, $T_c - T_g$ and T_m shown in **Fig. 4.3**. It is evident that as the concentration of manganese increases, T_g increases. T_c also increases with increasing Mn content while the melting temperature (T_m) remains fairly constant with composition. $T_c - T_g$, a measure of the stability of the glass to crystallisation, increases with increasing Mn content, but values are significantly smaller than those with higher phosphate content discussed in **Chapter 3**. Interestingly, the values differ in absolute terms from those reported by Kontor [1], but the trends appear the same.

Table 4.6 Summary of thermal parameters for selected glass samples of general composition $(60-x)$ Li_2O: xMnO: $40P_2O_5$. Estimated uncertainties in temperatures is ±5%

Composition(s) (x)	T_g (°C)	T_c (°C)	$T_c - T_g$ (°C)	T_m (°C)
50Li_2O: 10MnO: 40P_2O_5, $x = 10$	331	412	81	583
45Li_2O: 15MnO: 40P_2O_5, $x = 15$	340	418	78	584
40Li_2O: 20MnO: 40P_2O_5, $x = 20$	342	445	103	585

Table 4.7 shows the measured densities for synthesised glasses in the series $(60 - x)$ Li_2O: xMnO: $40P_2O_5$ ($x = 10$, 15 and 20). The compositional variation for the glasses made with naturally abundant Li is shown in **Fig. 4.4**. As expected, the plot shows an increase in density with increasing x-value as the heavier manganese substitutes two lighter lithium atoms.

As mentioned in chapter 3, the free volume ($\%V_{free}$) can be used to confirm how compact the studied glasses are. The compositional variation of free volume ($\%V_{free}$) in the $(60 - x)$ Li_2O: xMnO: $40P_2O_5$ glasses is presented in **Fig. 4.5**. The data show that there is a decrease in $\%V_{free}$ with increasing x-value from $x = 10$ to $x = 20$. This indicates that in this range, with increasing x-value, the glass becomes more compact through a strengthening of the bonding. This may be attributed to an increase the number of P-O-Mn bridges, as MnO content increases. The results are consistent with the compositional variation of T_g shown in **Fig. 4.3**. As discussed in **Chapter 3**, this effect competes with a reduction in the extent of cross-linking due to the reduction in the total number of cations, which would result in a decrease in T_g. In the $(60-x)$ Li_2O: xMnO: $40P_2O_5$ system, this latter effect is not evident.

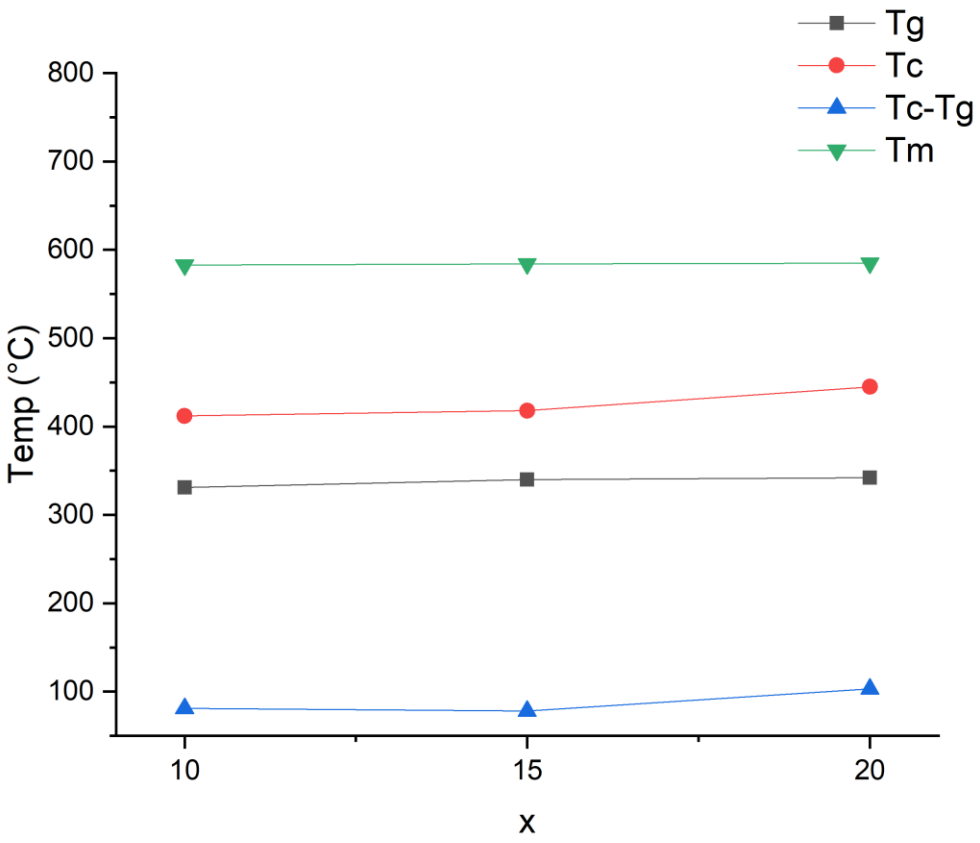

Fig. 4.3 Compositional variation of T_g, T_c, $T_c - T_g$ and T_m in glasses of composition $(60 - x)$ Li_2O: xMnO: $40P_2O_5$ (x = 10, 15 and 20).

Table 4.7 Summary of densities of glass samples in the series (60-x) Li_2O: xMnO: $40P_2O_5$ (x = 10, 15 and 20).

Composition(s) (x)	Li Type	Density (g/cm^3)
45Li_2O: 15MnO: 40P_2O_5, x = 15	Null	2.592 (±0.003)
50Li_2O: 10MnO: 40P_2O_5, x = 10	Normal	2.514 (±0.003)
45Li_2O: 15MnO: 40P_2O_5, x = 15	Normal	2.600 (±0.002)
40Li_2O: 20MnO: 40P_2O_5, x = 20	Normal	2.678 (±0.005)

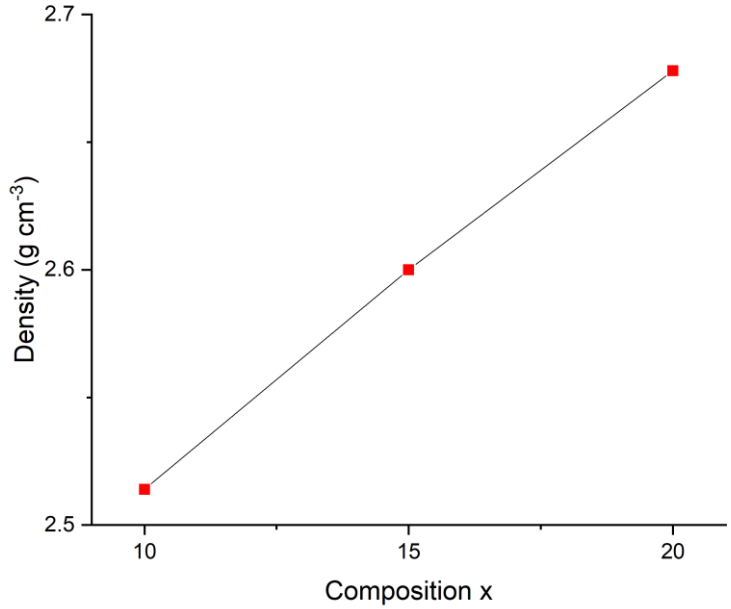

Fig. 4.4 Compositional variation of density for the synthesised "natural" glass samples in series (60-*x*) Li_2O: *x*MnO: 40P_2O_5 (*x* = 10, 15, and 20). Estimated standard deviations are smaller than the symbols used.

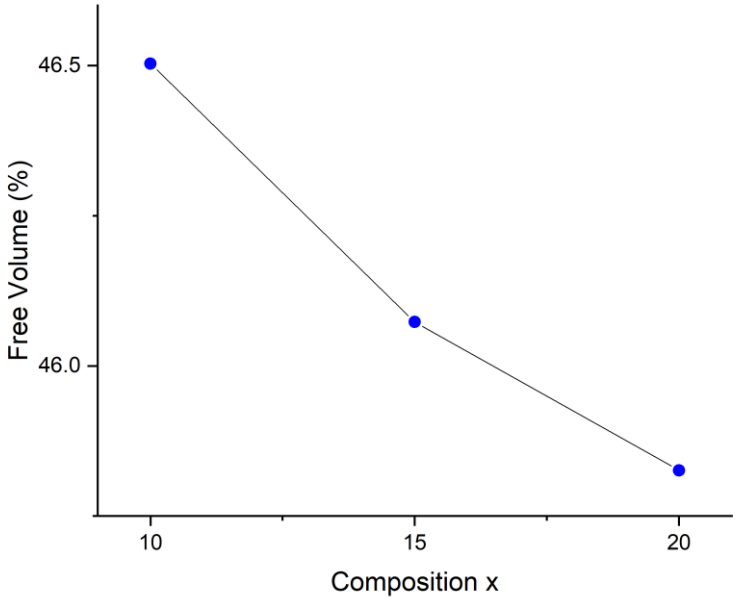

Fig. 4.5 Compositional variation of %V_{free} for the synthesised "natural" glasses in series (60-*x*) Li_2O: *x*MnO: 40P_2O_5 (*x* = 10, 15 and 20)

4.2.2 Structural analysis

Fig. 4.6 shows the IR spectra of the studied glass compositions, (60 − *x*) Li_2O: *x*MnO: 40P_2O_5 (*x* = 10, 15 and 20). As seen in the compositions studied in **Chapter 3**, all peaks are broad, typical for a disordered glass system. In this system, several bands are evident and are consistent with metaphosphate chains. All glass compositions show peaks at around 900 cm^{-1}, which are attributed to the P-O-P asymmetric stretch. A weak band characteristic of $(PO_3)^-$ (Q^2 species, metaphosphate) can be seen at around 1280 cm^{-1}. In addition, a broad band at around 780 cm^{-1} corresponds to (P-O-P) symmetric vibration of bridging oxygen atoms [7,8]. An obvious peak characteristic of $(PO_{3.5})^{2-}$ (Q^1 species, pyrophosphate) can be seen at around 1100 cm^{-1}. This is expected in this system since the glasses now lie in the polyphosphate region i.e., they would be expected to contain mixtures of Q^1 and Q^2 phosphate species. When the IR spectra of glass compositions, (60-*x*) Li_2O: *x*MnO: 40P_2O_5 are compared to those of glass compositions, (50-*x*) Li_2O: *x*MnO: 50P_2O_5 discussed in **Chapter 3**, we can observe that peaks at around 1280 cm^{-1} (corresponding to $(PO_3)^-$, Q^2 species, metaphosphate) are commonly weaker, while peaks at around 1100 cm^{-1} (corresponding to $(PO_{3.5})^{2-}$, Q^1 species, pyrophosphate) are of relatively higher intensity (**Fig. 4.7**). Thus, we can conclude that in the composition (60-*x*) Li_2O: *x*MnO: 40P_2O_5 (*x* = 10, 15 and 20), there are less $(PO_3)^-$ (Q^2) and more $(PO_{3.5})^{2-}$ (Q^1).

As discussed in **Chapter 3** it is possible to calculate the theoretical phosphate speciation in the synthesised glasses. Assuming manganese and lithium are exclusively network modifying glasses in the (60-*x*) Li_2O: *x*MnO: 40P_2O_5 system should show equal amounts of Q^1 and Q^2 phosphate species (i.e. total network modifying charge = 120). This would be expected to change if manganese adopted a network forming role.

Fig 4.8 shows the X-ray total pair correlation functions, D(*r*), generated from Ag-Kα radiation (λ = 0.5609 Å) for samples of composition (60-*x*) Li_2O: *x*MnO: 40P_2O_5 (*x* = 10, 15 and 20). The profiles are all similar to each other. Each shows a strong broad correlation with a maximum around 1.46 Å, corresponding to the P-O bond in the phosphate tetrahedra [9]. Similar to those profiles seen in Chapter 3, a weaker broad correlation with a maximum around 2.3 Å, is attributable to Mn-O, while, a stronger peak at around 3.3 Å, corresponds to a combination of P-P, P-Mn and Mn-Mn correlations. Synchrotron X-ray radiation data were subsequently collected on the Diamond facility to provide further detail (**Fig. 4.9** and **Fig. 4.10**).

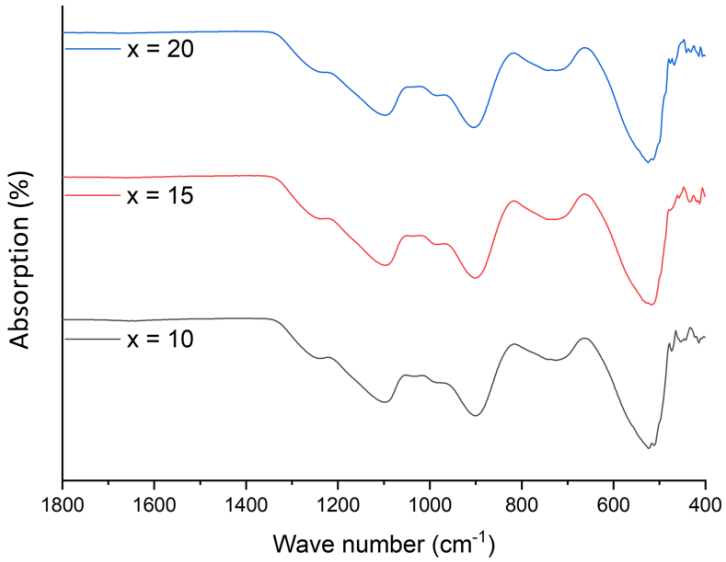

Fig. 4.6 Infrared spectra of the studied glass compositions, (60 − *x*) Li_2O: *x*MnO: 40P_2O_5 (*x* = 10, 15 and 20).

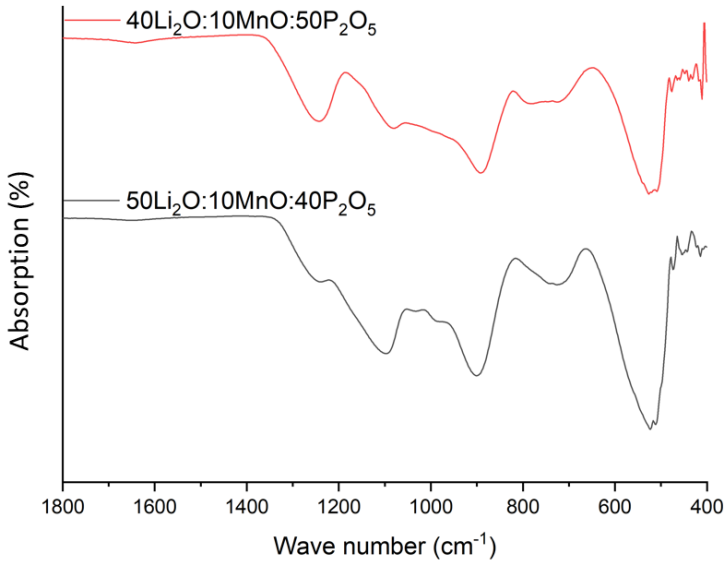

Fig. 4.7 Infrared spectra of the glass composition 50Li_2O:10MnO:40P_2O_5, compared to that of the glass composition 40Li_2O:10MnO:50P_2O_5.

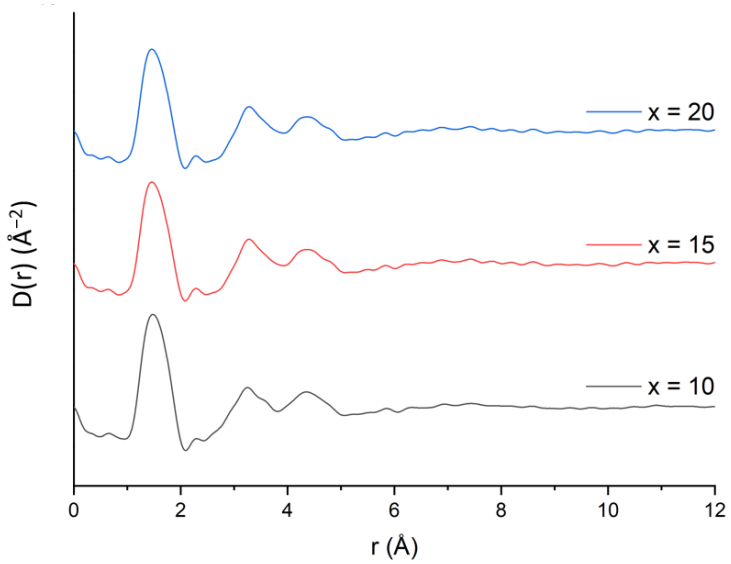

Fig. 4.8 X-ray total pair correlation functions, D(*r*), generated from Ag-Kα radiation (λ = 0.5609 Å) for samples of composition (60 − *x*) Li_2O: *x*MnO: 40P_2O_5 (*x* = 10, 15 and 20).

.

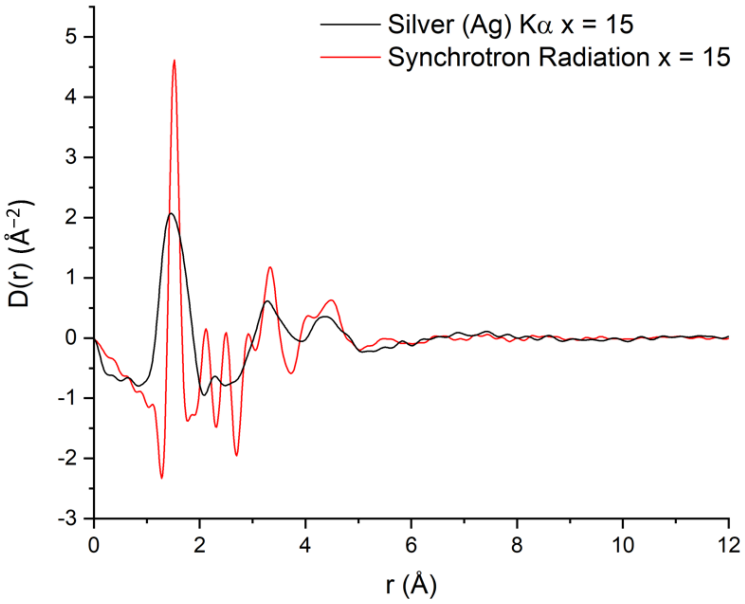

Fig. 4.9 Comparison of D(*r*) profiles for 50Li_2O:10MnO:60P_2O_5 glass composition from Ag Kα (black) and synchrotron radiation (red).

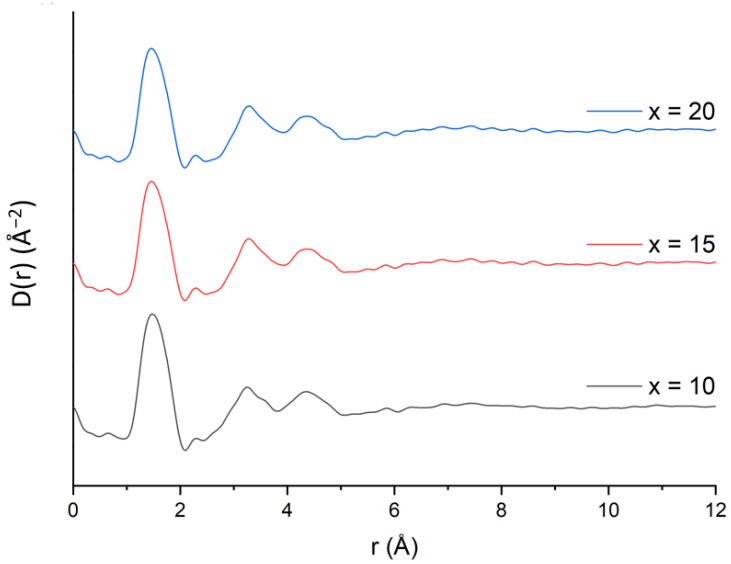

Fig. 4.10 Synchrotron X-ray diffraction pair distribution functions D(*r*) for (60 − *x*) Li_2O: *x*MnO: 40P_2O_5 (*x* = 10, 15 and 20) glass compositions.

Fig. 4.10 show the D(*r*) profiles derived from synchrotron X-ray diffraction data for glass compositions *x* = 10, 15 and 20. The D(*r*) profiles of all glass samples show a strong correlation centred at around 1.53 Å, corresponding the P-O bonds, with Mn-O correlation at about 2.13 Å. The intensity of the Mn-O peak compared to that of the O-O peak (at around 2.5 Å) increases with increasing *x* value, reflecting the increasing Mn content. As discussed in Chapter 3, the Li-O correlations (expected at around 1.9 Å) are absent due to the relatively small contribution of Li to the X-ray scattering.

D(*r*) total pair functions derived from neutron scattering data for glass compositions *x* = 10, 15 and 20, are shown in **Fig. 4.11**, with details shown in **Fig 4.12**. The P-O bond correlation is clearly visible at around 1.5 Å, followed by the combined Mn-O/Li-O negative peak with a minimum around 2.00 Å, with increasing value of *x*, the minimum peak gradually shifts to around 2.05 Å (**Fig 4.12**), reflecting the greater contribution of Mn-O correlations (at around 2.1 Å) to this peak. For the *x* = 15 composition, measurements were performed on an additional null-Li sample to isolate the correlations involving Li.

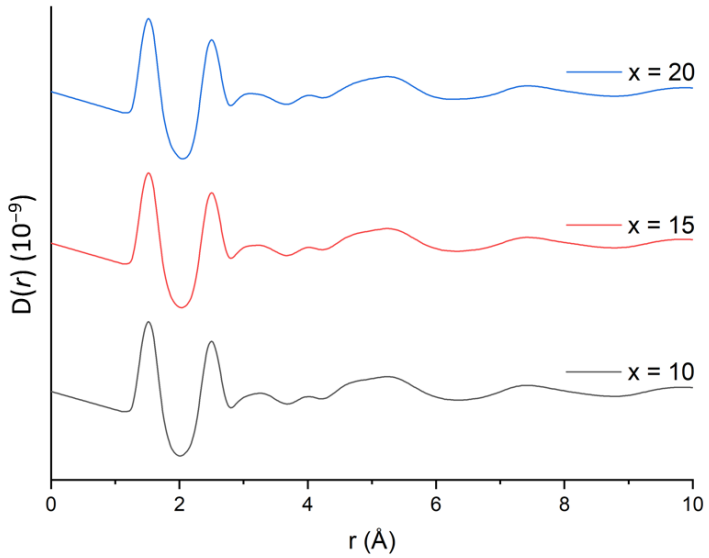

Fig. 4.11 Neutron scattering pair distribution functions D(*r*) for (60 − *x*) Li_2O: *x*MnO: 40P_2O_5 (*x* = 10, 15 and 20) glass compositions.

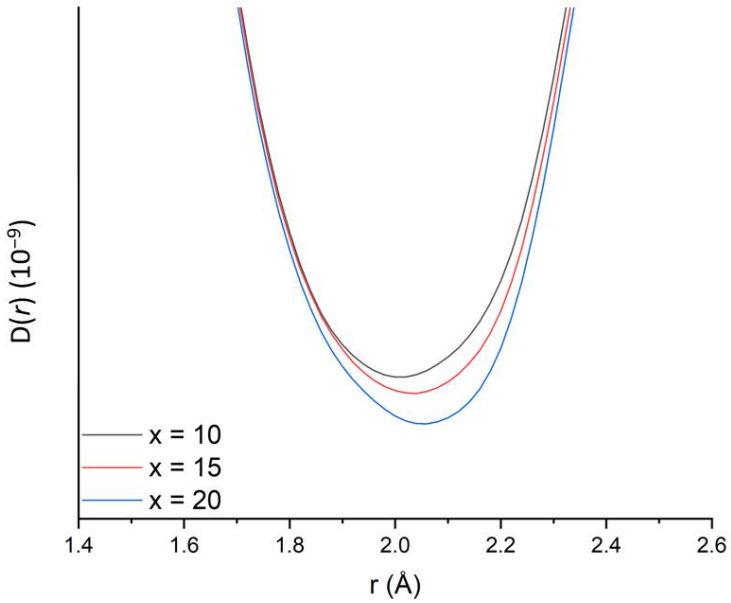

Fig. 4.12 Details (at the range of 1.4 to 2.6 Å) for neutron scattering pair distribution functions D(*r*) for (60 − *x*) Li_2O: *x*MnO: 40P_2O_5 (*x* = 10, 15 and 20) glass compositions.

A comparison of the D(r) profiles for the x = 15 compositions containing natural and null Li are shown in **Fig. 4.13.** A significant difference is seen in the Li-O/Mn-O negative peak around 2.1 Å. For the null Li containing sample, the peak has more structure, while for the natural Li sample the corresponding peak is broader and centred at about 2.0 Å.

(a)

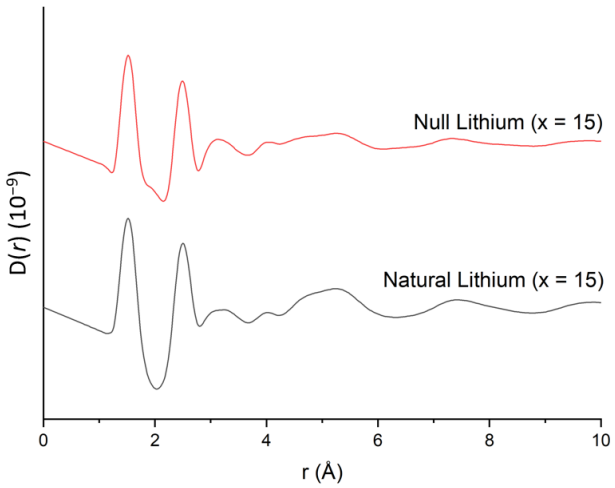

(b)

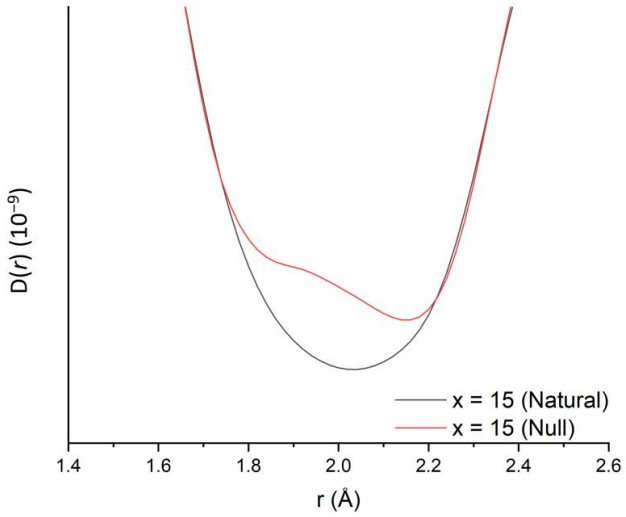

Fig. 4.13 Comparison of D(r) profiles for natural and null lithium containing glass samples of $45Li_2O$: 15MnO: $40P_2O_5$ (a), with detail shown in (b).

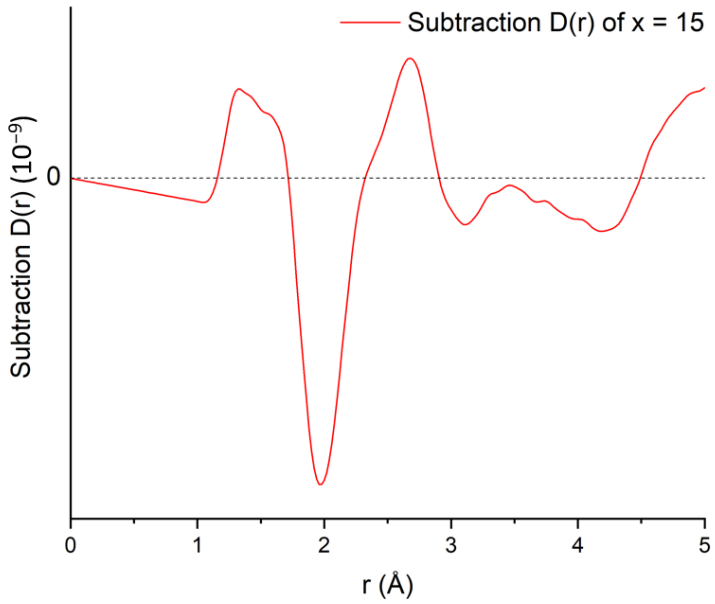

Fig. 4.14 D(*r*) profile derived by subtracting that of the null Li containing sample from the natural Li containing sample (*x* = 15).

The result of subtracting the D(*r*) profile for the null Li containing sample from that of the corresponding natural Li sample is shown in **Fig. 4.14.** The data show a sharp negative peak at around 1.98 Å, corresponding to Li-O pair correlations. This is followed by a positive peak at around 2.7 Å, likely due to Li-Li and Li-Mn correlations and the Li-P at around 3.1 Å (negative peak). The results are even clearer than those seen in Chapter 3 due to the greater Li content.

The experimental melting temperatures T_m of compositions (60 − *x*) Li_2O: *x*MnO: 40P_2O_5 (*x* = 10, 15 and 20) are relatively lower than most T_m values of compositions discussed in **Chapter 3**. Thus, lower simulated T_m values for these compositions were applied to the MD simulation. **Fig. 4.15** shows the neutron scattering pair correlation function D(*r*) derived from the MD simulation, for (60 − *x*) Li_2O: *x*MnO: 40P_2O_5 (*x* = 10, 15 and 20) glass compositions.

(a)

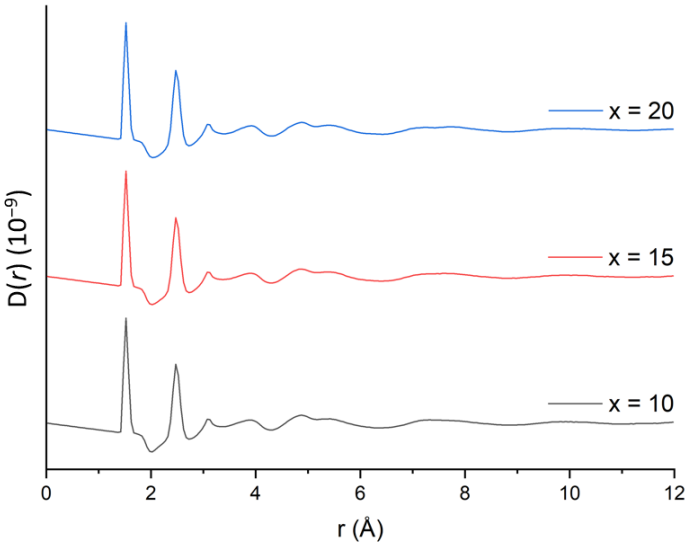

(b)

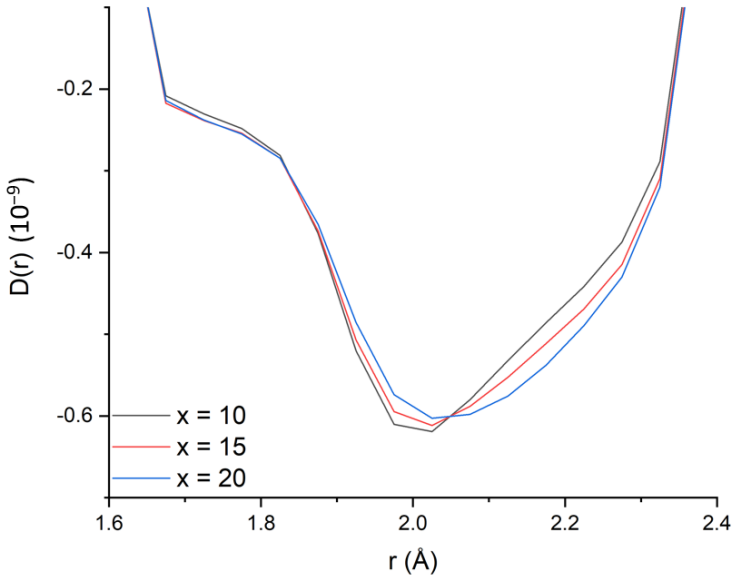

Fig. 4.15 Neutron D(*r*) profiles for glass samples of composition (60-*x*) Li_2O: *x*MnO: 40P_2O_5 (*x* =10, 15 and 20) generated from MD simulations showing (a) full profile and (b) detail at low *r*-values.

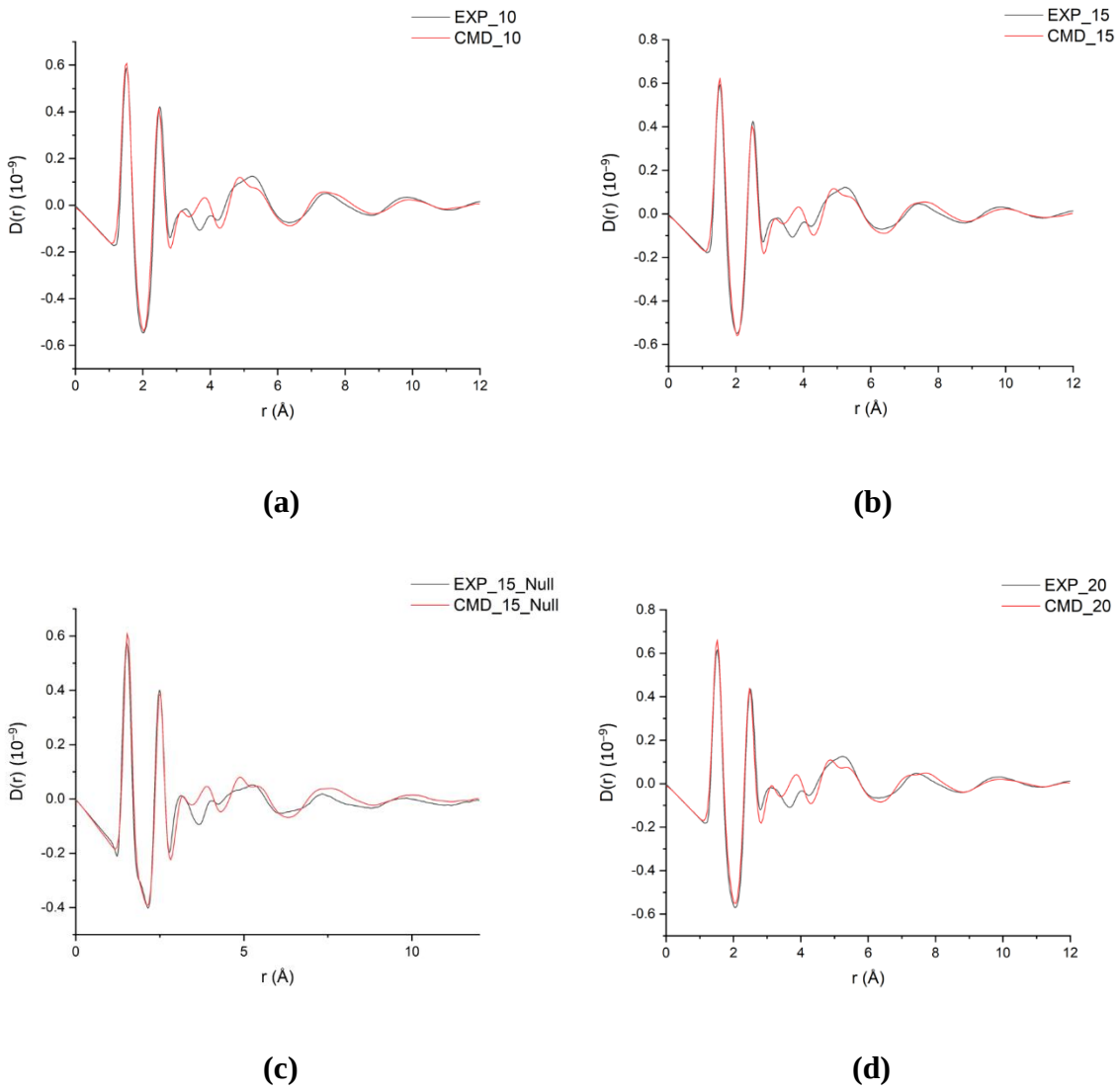

Fig. 4.16 Comparison of simulated (Gaussian broadened) and experimental neutron D(*r*) profiles for glass samples of composition (60-*x*) Li_2O: *x*MnO: 40P_2O_5 (*x* =10, 15 and 20).

As for the compositions discussed in **Chapter 3**, while the MD derived D(*r*) profiles for glass samples are similar to those for the corresponding compositions found experimentally, in the MD derived data peaks are sharper, due to the limit of the finite size of the model and were therefore broadened using a Gaussian convolution (**Eqn. 3.10**). Comparisons between the Gaussian broadened simulated D(*r*) profiles with the corresponding experimental data are shown in **Fig. 4.16**.

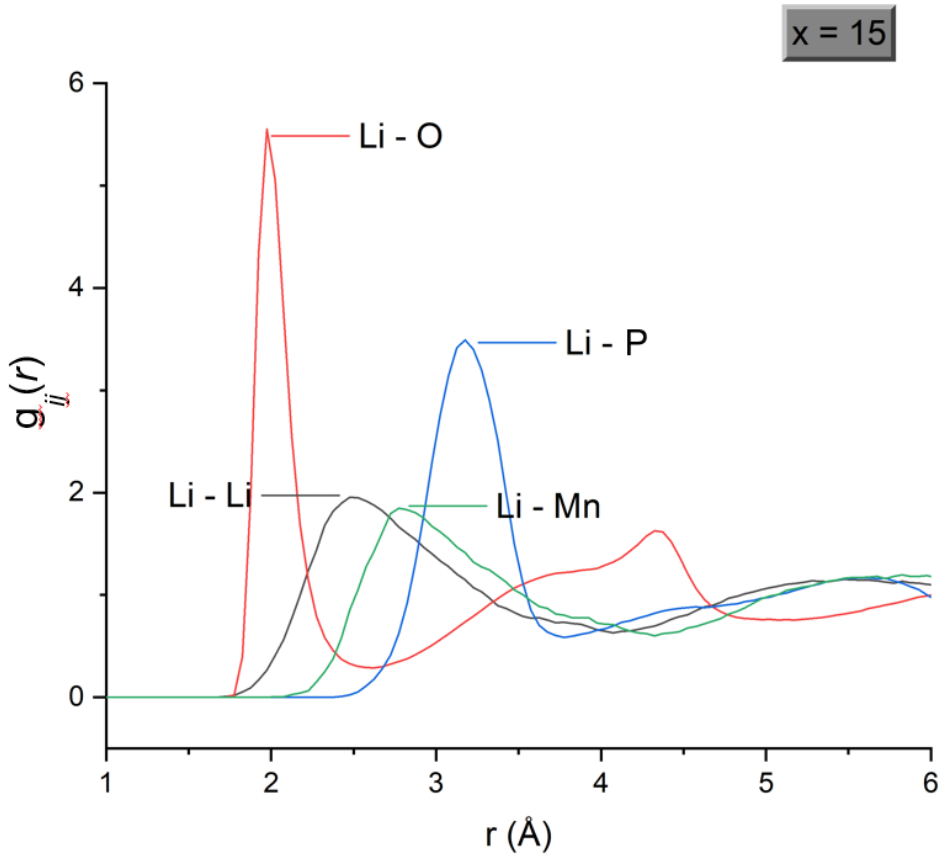

Fig. 4.17 Li-Li, Li-O, Li-P and Li-Mn pair correlations $g_{ij}(r)$ generated from MD simulations for glass samples of composition $45Li_2O$: 15MnO: $60P_2O_5$ (x = 15).

As seen in **Chapter 3**, while the MD simulations show good agreement with the experimental data up to 3 Å, differences appear above 3 Å. These differences are mainly in the intermediate range from 3 to 6 Å. Thus, it can be concluded that the simulated structures reflect the short-range structure of each composition accurately but are less accurate at the intermediate range. Selected partial pair correlation functions $g_{ij}(r)$ derived from the MD simulations are shown in **Fig. 4.18**, with the derived coordination numbers and average contact distances given in **Table 4.8**. The Li-O, Li-Li, Li-P and Li-Mn partial pair correlations $g_{ij}(r)$ for the x = 15 composition are shown in **Fig. 4.17**. The correlations show good agreement with the experimental D(r) derived by subtracting the null Li data from that of natural Li. This confirms the assignment of the correlations discussed above.

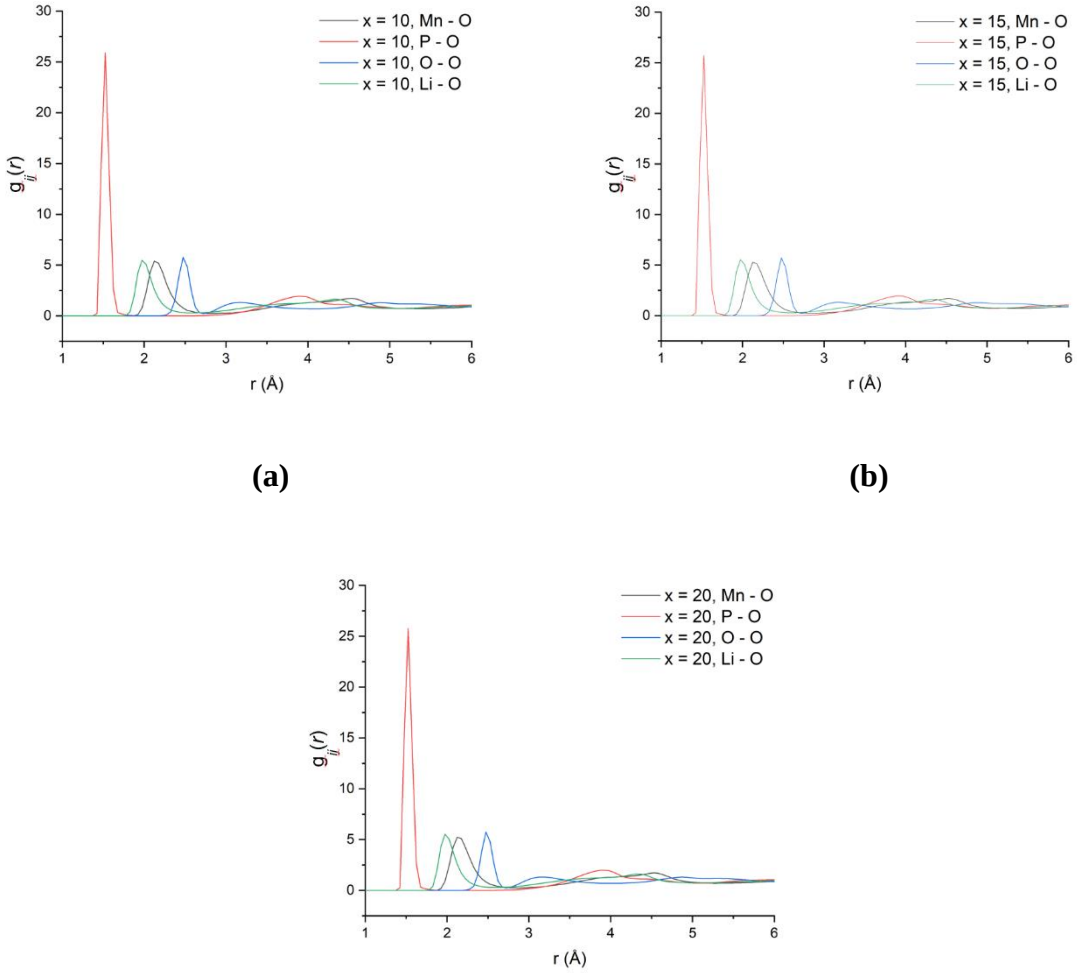

Fig. 4.18 Selected partial pair correlations $g_{ij}(r)$ generated from MD simulations for glass samples of composition (60-*x*) Li_2O: *x*MnO: $40P_2O_5$ (*x* =10, 15 and 20).

From the results in **Table 4.8**, we can see that the P-O bond length vary little with composition, with a P-O coordination number of around 4. The Li-O coordination numbers of around 3.9 confirm predominantly tetrahedral coordination for Li, Li-O distances ranging from 1.96 Å to 1.99 Å, in good agreement with the value obtained from subtracting the D(*r*) profile of the null lithium containing sample from that of the sample containing natural Li (**Fig. 4.14**).

Table 4.8 Coordination numbers (CN) and selected correlation distances *d* (Å) derived from MD simulations for glasses of composition (60-*x*) Li_2O: *x*MnO: 40P_2O_5. Uncertainties are estimated at ±0.5%.

Composition *x*	10	15	20
Li - O CN	3.90	3.87	3.88
Li - O *d* (Å)	1.99	1.96	1.96
Mn - O CN	4.79	4.87	4.86
Mn - O *d* (Å)	2.16	2.15	2.13
P - O CN	4.04	4.03	4.04
P - O *d* (Å)	1.49	1.49	1.49
O – O CN	/	/	/
O – O *d* (Å)	2.47	2.49	2.44

Table 4.9 Manganese coordination number (CN) distributions for studied glass composition (60-*x*) Li_2O: *x*MnO: 40P_2O_5 (*x* =10, 15, and 20) derived from MD models.

x	CN 2	CN 3	CN 4	CN 5	CN 6	CN 7
10	0	0	0.3195	0.5714	0.1090	0
15	0	0.0075	0.2481	0.6140	0.1278	0
20	0	0.0019	0.2594	0.6109	0.1278	0

The Mn-O distance is around 2.15 Å and decreases slightly with increasing Mn content. The Mn-O coordination number is around 4.8 in all compositions. It increases slightly from *x* = 10 to *x* = 15 but shows little change between *x* = 15 and 20. The observed values are consistent with a mixture of predominantly 4 and 5 coordinate manganese i.e. network forming and network modifying, respectively. The Mn-O coordination number distributions are summarised in **Table 4.9** and confirm that the fraction of 4 coordinate network modifying manganese decreases from *x* = 10 to *x* = 15 but is fairly constant from *x* = 15 to *x* = 20. Remembering that the *x* = 20 composition was partially crystallised, this indicates that the residual glass phase is close in composition to *x* = 15.

Based on the distributions shown in **Table 4.9** it is evident that at *x* = 15 approximately 25% of the manganese content is network forming. If it is assumed that this is in the Q^4 state

i.e. $[MnO_2]^{2-}$ then there are 3.75 $[MnO_2]^{2-}$ units contributing to the network charge per formula unit and the remaining 11.25 Mn^{2+} ions per formula unit along with the 90 Li^+ ions, make up the total network modifying charge of 112.5 per formula unit. Subtracting the network charge from the Q^4 manganate units leaves a modifying charge of 105 per formula unit that needs to be balanced by the phosphate species. If x is the number of Q^1 phosphate species and y is the number of Q^2 phosphate species, then:

$$105 = 2x + y \tag{4.1}$$

and

$$80 = x + y \tag{4.2}$$

Therefore x = 25 and y = 55 corresponding to 31.25% Q^1 and 68.75% Q^2 phosphate species. Thus, the structural formula of the glass can be written as:

$$Li^+_{90}\, Mn^{2+}_{11.25}\, [(MnO_2)^{2-}_{3.75}\, (PO_{3.5})^{2-}_{25}\, (PO_3)^-_{55}]$$

Of course, other phosphate species are possible such as Q^4 and Q^0 through disproportionation.

4.2.3 Electrical characterisation

Electrical characterisation of compositions of $60Li_2O$: $40P_2O_5$ (x = 0) and $45Li_2O$: $15MnO$: $40P_2O_5$ (x = 15) was carried out using a.c. impedance spectroscopy. At each measured temperature, a semicircle or part of semicircle was observed corresponding to the bulk resistance of the sample, followed by a low frequency tail corresponding to the blocking electrode. Arrhenius plots of conductivity for these two compositions are shown in **Fig. 4.19**. The data correspond to the first cooling cycle.

The unsubstituted sample (x = 0) with the highest lithium ion concentration exhibits the highest conductivities over the whole temperature range studied. This sample was partially crystallised, but the conductivity of the glassy and crystalline components could not be separated. **Table 4.10** summarises the derived electrical parameters at 200 °C and 300 °C for the studied compositions. The conductivity, of the unsubstituted sample is significantly higher at both temperatures and has a lower activation energy. For the x = 15 composition the value

of conductivity at 300 °C is appreciably high in the order of 10^{-3} S cm^{-1} typical of the best solid-state Li^+ ion conductors and in good agreement with the data reported by Kontor [1]. The activation energy of the x = 15 sample is higher than at x = 0 reflecting a more compact structure with less free volume, resulting in lower ion mobility.

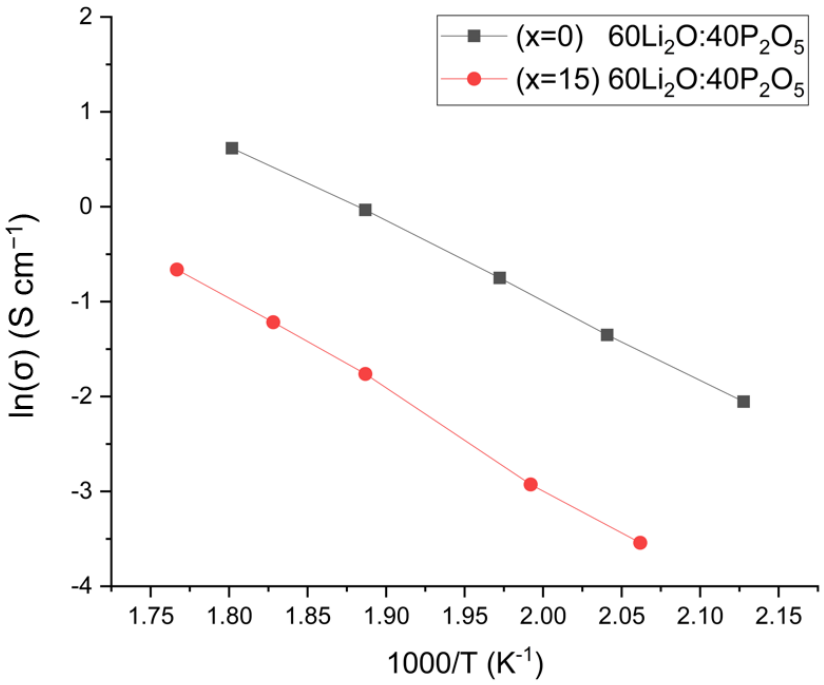

Fig. 4.19 Arrhenius plots of conductivity for selected compositions (x = 0 and 15) in the (60 − x) Li_2O: xMnO: 40P_2O_5 system.

Table 4.10 Derived electrical parameters for selected compositions in the (60 − x) Li_2O: xMnO: 40P_2O_5 system. (Estimated uncertainty is ±5%).

Composition (x)	$\sigma_{200°C}$ / σ_{473K} (S cm^{-1})	$\sigma_{300°C}$ / σ_{573K} (S cm^{-1})	Activation Energy E_a (eV)
0	3.04×10^{-4}	5.28×10^{-3}	0.71
15	3.57×10^{-5}	1.156×10^{-3}	0.86

4.3 Conclusions

The lower phosphate content of the composition (60−*x*) Li_2O: *x*MnO: 40P_2O_5 make the glass forming region narrower compared to the (50−*x*) Li_2O: *x*MnO: 50P_2O_5 system in **Chapter 3**. However, the conductivities are higher in these glasses compared to those in **Chapter 3**, due to the higher Li_2O content. While the conductivity decreases with respect to that of the unsubstituted composition, due to the decrease in carrier concentration, the $x = 15$ composition shows appreciably high conductivity at 300 °C. The activation energy is seen to rise from $x = 0$ to $x = 15$ reflecting the greater compactness of the structure resulting in poorer ion mobility. Manganese again shows a mixture of predominantly 4 and 5 coordination geometries with some 6 coordinates. In contrast to the (50−*x*) Li_2O: *x*MnO: 50P_2O_5 compositions, the fraction of network forming manganese decreases with increasing *x*-value up to $x = 15$, resulting in an increase in T_g, and also due to the decrease in the total number of cations resulting in fewer cross links. Li adopts mainly four coordinate geometry but is still considered to be essentially network modifying due to the ionicity of the Li-O interaction.

4.4 References

1 Kontor, M. *Lithium ion conducting glass-based batteries* MSc thesis, Queen Mary University of London, (2004).

2 Laeter, J. R. D. *et al.* Atomic Weights of the Elements: Review 2000 (IUPAC Technical Report). *Pure and Applied Chemistry* **75**, 683–800 (2003).

3 Soper, A. K. Report RAL-TR-2011-013. (Rutherford Appleton Laboratory Technical, 2011).

4 Todorov, I., Smith, W., Trachenko, K. & Dove, M. DL_POLY_3: new dimensions in molecular dynamics simulations via massive parallelism. *Journal of Materials Chemistry* **16**, 1911–1918 (2006).

5 Todorov, I. & Smith, W. *THE DL_POLY_ 4 USER MANUALS*. (STFC Daresbury Laboratory, 2015).

6 Nosé, S. A unified formulation of the constant temperature molecular dynamics methods. *J. Chem. Phys.* **81**, 511 (1984).

7 Muresan, D. *et al.* Structural investigation of calcium-soda-phosphate glasses with small content of silver oxide. *Journal of Optoelectronics and Advanced Materials* **8**, 558-560 (2006).

8 Schwarz, J., Ticha, H., Tichy, L. & Mertens, R. Physical properties of PbO-ZnO-P_2O_5 glasses. I. Infrared and Raman spectra. *Journal of Optoelectronics and Advanced Materials* **6**, 737-746 (2004).

9 Gamoke, B., Neff, D. & Simons, J. Nature of P−O Bonds in Phosphates. *The Journal of Physical Chemistry A* **19**, 5677-5684 (2009).

Chapter 5 Overall Conclusions and Future Work

5.1 Conclusions

The structures and conductivities of lithium manganese glasses of different compositions, (50 − *x*) Li_2O: *x*MnO: 50P_2O_5 (*x* = 10.0, 25.0, 33.3, 40.0 and 50.0) and (60 − *x*) Li_2O: *x*MnO: 40P_2O_5 (*x* = 10, 15, and 20) have been discussed. The work presented in this thesis has shown that structural information can be obtained by molecular dynamics simulations of the results of X-ray and neutron scattering experiments.

Theoretically, the system (50 − *x*) Li_2O: *x*MnO: 50P_2O_5 are metaphosphate glasses, with an [O] / [P] ratio of 3.0, and the phosphate speciation should be Q^2, i.e. it should contain chains and/or rings of $(PO_3)_n^{n-}$ with Li^+ and Mn^{2+} cations cross-linking them. Similarly, the system (60 − *x*) Li_2O: *x*MnO: 40P_2O_5 are polyphosphate glasses with an [O] / [P] > 3.0, in which there should be there should be Q^2 species, $(PO_3)^-$ and Q^1 species, $(PO_{3.5})^{2-}$, which act as the chain ends. The IR results confirm this speciation. In the (50 − *x*) Li_2O: *x*MnO: 50P_2O_5 system, glasses are readily achieved over a wide compositional range ($10 \leq x \leq 50$). However, the conductivity of these glasses is relatively low due to the decreasing charge carrier concentration with increasing level of substitution. Therefore, a set of compositions with higher lithium ion concentration was chosen for further study. Unfortunately, due to the lower phosphate content, in the (60 − *x*) Li_2O: *x*MnO: 40P_2O_5 system, the glass forming compositional region is limited to approximately $10 \leq x \leq 15$ and at *x* = 20 partial crystallisation occurs, with the residual glass phase close in structure to that at *x* = 15, consistent with a previous study [1] in the Abrahams group. While, more rapid quenching techniques such as using rollers might yield glasses at a higher level of substitution, this conductivity is likely to be lower due to the reduced lithia content and consequently this was not pursued.

The structural results show that Mn plays a very important role in the structure of both systems. Mn^{2+} cations can act as both network modifiers and network formers in oxide glasses. The MD simulations show that in all the compositions studied most of Mn^{2+} cations have 5 or 6 coordination geometries i.e. network modifying cations, but a significant proportion of the Mn^{2+} show network forming character with coordination number of 4. Based on electroneutrality consideration, these network forming species, are likely to be Q^4 manganate

species i.e. $[MnO_2]^{2-}$ units. This means that in the system $(50 - x)$ Li_2O: xMnO: $50P_2O_5$, the presence of $[MnO_2]^{2-}$ units in the network causes the generation of some neutral Q^3 phosphate species, $(PO_{2.5})$ to maintain electroneutrality. Similarly, in the system $(60 - x)$ Li_2O: xMnO: $40P_2O_5$, the presence of $[MnO_2]^{2-}$ units reduces the amount of Q^1 species, $(PO_{3.5})^{2-}$ and increases that of Q^2 species, $(PO_3)^-$.

The stronger more covalent Mn-O interactions of the $[MnO_2]^{2-}$ units within the network make the structure stronger and more compact. This causes T_g to increase, free volume to decrease and activation energy for ionic conductivity to increase; the latter due to reduced mobility of the Li^+ ions. One must also consider the case when cations act as network modifiers. As Hudgens *et al.* [2] reported, on addition of Li_2O to metaphosphate glass P_2O_5 above 20 mol %, T_g increases, although the fraction of non-bridging oxygen still increases. In this case the network modifying cations act as chain cross-linkers, which also make the structure more compact. Thus, both these mechanisms would cause T_g to increase. However, in the present systems the total number of cations decreases with increasing level of substitution as one Mn^{2+} cation replaces two Li^+ cations. In this case, one would expect T_g to decrease and free volume to increase as the number of cross links decreases and the structure becomes more open. Thus, the system involves two competing mechanisms, the extent of which depends on the level of substitution and the proportion of manganese in network forming roles i.e. $[MnO_2]^{2-}$. **Table 5.1** and **Table 5.2** show the total numbers of modifying cations (Li^+ and Mn^{2+}) and network forming $[MnO_2]^{2-}$ units per formula unit in the studied systems, derived from the MD simulations.

Table 5.1 Numbers of network forming $[MnO_2]^{2-}$ units and modifying cations (Mn^{2+} and Li^{+}) numbers per formula unit for glass compositions (50 − *x*) Li_2O: *x*MnO: 50P_2O_5 (*x* = 10, 25, 33.3, 40 and 50) derived from MD simulations.

unit	10	25	33.3	40	50
cations	86.8	65.8	53.0	43.7	31.0
$[MnO_2]^{2-}$	3.2	9.2	13.5	16.3	19. 0

Table 5.2 Numbers of network forming $[MnO_2]^{2-}$ units and modifying cations (Mn^{2+} and Li^{+}) numbers per formula unit for glass compositions (60 − *x*) Li_2O: *x*MnO: 40P_2O_5 (*x* = 10, 15, and 20) derived from MD simulations.

unit	10	15	20
cations	106.8	101.2	94.8
$[MnO_2]^{2-}$	3.2	3.8	5.2

The data in **Table 5.1** and **5.2** are illustrated graphically in **Fig. 5.1** and **5.2**, respectively. It is evident from these that the concentration of modifying cations and hence the cross-link density decreases with increasing *x* value which would cause a weakning of the network, while the number of network-forming Q^4 manganate units increases which would strengthen the network. In other words, on addition of MnO, there are two competing mechanisms, one strengthening the network and another weakening the network. In the case of the (50 − *x*) Li_2O: *x*MnO: 50P_2O_5 system the structure becomes most compact when *x* = 33.3, which leads to a maximum in T_g, a minimum in free volume and a maximum in activation energy.

In the case of the (60 − *x*) Li_2O: *x*MnO: 40P_2O_5 (*x* = 10, 15, and 20) system, T_g rises and free volume decrease across the glass forming region as *x* increases. From this it may be concluded that the main factor dominating the strength and openness of the network is the increase in the number of Q^4 manganate species with increasing *x*-value.

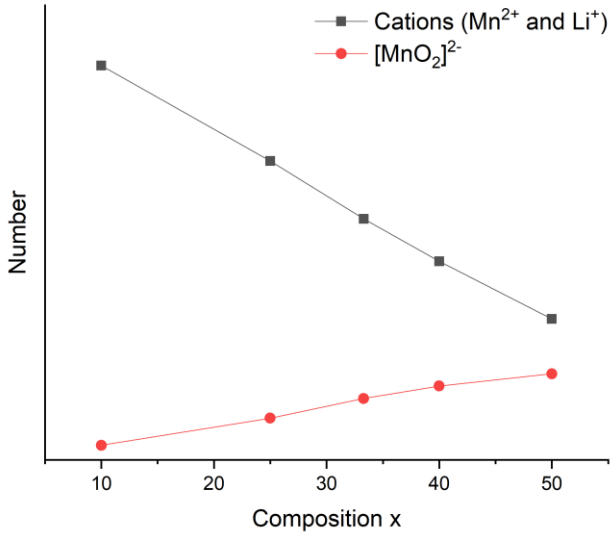

Fig. 5.1 Compositional variation of $[MnO_2]^{2-}$ and total modifying cation (Mn^{2+} and Li^{+}) numbers per formula unit for glass compositions $(50 - x)$ Li_2O: xMnO: $50P_2O_5$ (x = 10, 25, 33.3, 40 and 50) derived from MD simulations.

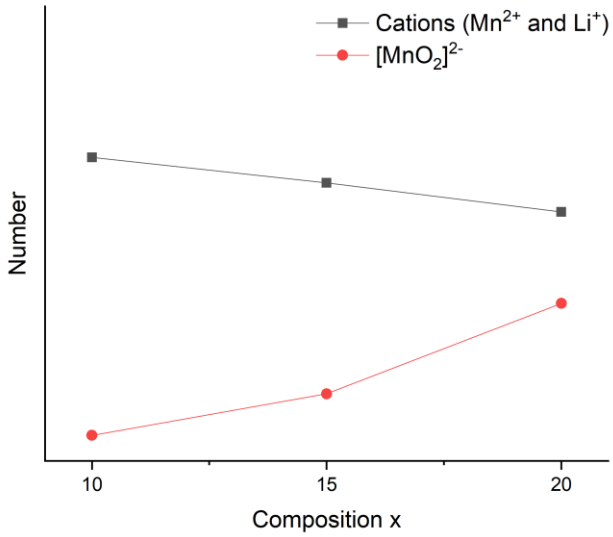

Fig. 5.2 Compositional variation of $[MnO_2]^{2-}$ and total modifying cation (Mn^{2+} and Li^{+}) numbers per formula unit for glass compositions $(60 - x)$ Li_2O: xMnO: $40P_2O_5$ (x = 10, 15, and 20) derived from MD simulations.

Table 5.3 Li^+ concentration, conductivities at 473 K and 573 K, free volume, numbers of network forming $[MnO_2]^{2-}$ units per formula unit and activation energy for conductivity for glass compositions $(50 - x)$ Li_2O: xMnO: $50P_2O_5$ (x = 10, 25, 33.3 and 40)

Composition	10	25	33.3	40
Li+ Concentration (nm^{-3})	13.34	8.40	5.62	3.35
Conductivity at 473 K ($\times 10^{-6}$ S cm^{-1})	408	16.9	4.84	0.22
Conductivity at 573 K ($\times 10^{-8}$ S cm^{-1})	720	20.2	3.71	0.14
Free Volume (%)	46.96	46.56	46.44	46.71
$[MnO_2]^{2-}$ units per formula unit	3.22	9.20	13.53	18.97
Activation energy for conductivity (eV)	1.00	1.09	1.28	1.25

From the electrical results the strategy of increasing the carrier concentration to improve conductivity was effective, with the conductivity of glass compositions $(60 - x)$ Li_2O: xMnO: $40P_2O_5$ more than 10 times higher than that of glass compositions $(50 - x)$ Li_2O: xMnO: $50P_2O_5$ due to the higher Li^+ concentration. In addition, the activation energy E_a is comparatively lower. However, the increase in the [O] / [P] ratio limits the glass forming region making synthesis more difficult. More details can be revealed by further analysis of the collected conductivity data. Some aspects of glass composition $(50 - x)$ Li_2O: xMnO: $50P_2O_5$ will be briefly discussed as follows and some relevant parameters for this composition in the range of x = 10, 25, 33.3 and 40, are listed in **Table 5.3**. As mentioned in **Section 1.4.1**, we can obtain the relation between the conductivity σ and the mobility μ through **Eqn. 5.11**:

$$\sigma = q^2 c \mu \tag{5.1}$$

Thus, conductivity, σ, is dependent on the charge carrier concentration c and its mobility μ, since the charge of ion q is constant. In addition, the percentage free volume $\%V_{free}$ changes little across the glass forming region as x increases, with values between 46% and 47%. The main influence of free volume is on mobility and is evident in the activation energy, with a maximum in activation energy corresponding to a minimum in $\%V_{free}$. The relation between σ and the charge carrier concentration, c, would be expected to be linear if mobility was constant. However, there is a clear deviation away from a linear relationship between these two quantities evident in **Fig. 5.3**. While $\%V_{free}$ has a direct effect on ion mobility and hence conductivity other factors also need to be taken into account.

(a)

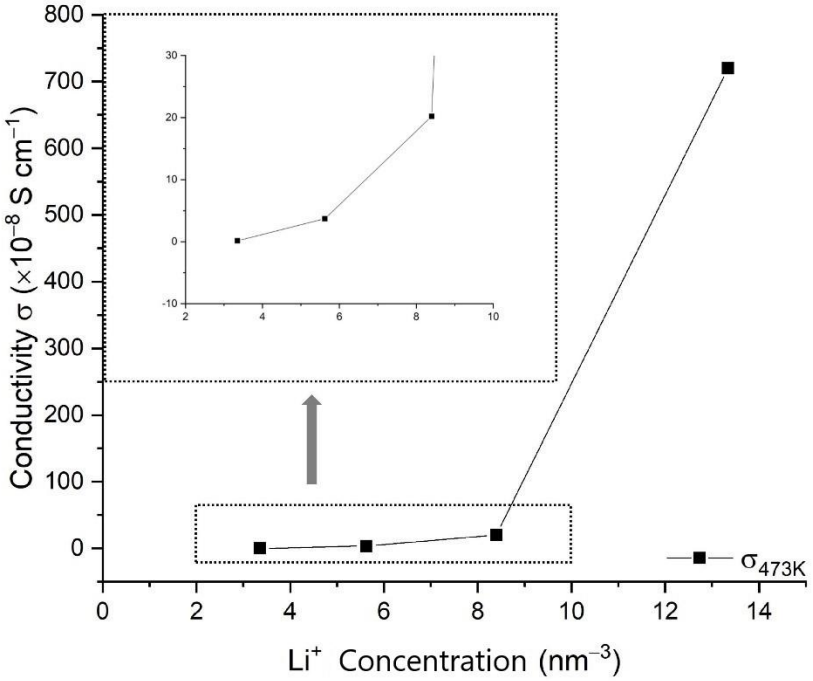

(b)

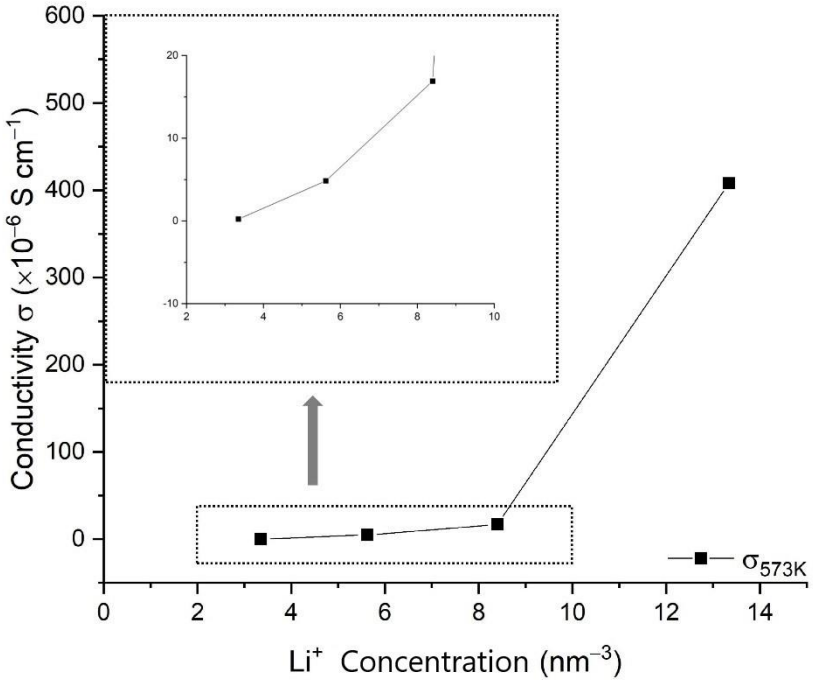

Fig. 5.3 The relation between conductivity σ and Li^+ concentration for glass compositions (50 − x) Li_2O: xMnO: 40P_2O_5 (x = 10, 25, 33.3 and 40) (a) at 473 K, and (b) 573 K.

A helpful idea can be taken from the Anderson-Stuart strong electrolyte model presented in **Section 1.4.3**, which describes that N_i (the effective carrier density of ion *i*), not the theoretical charge carrier concentration, *c*, determines the conductivity, σ, with the charge of ion *q* and the mobility μ. If *P* indicates the fraction of charge carrier concentration, *c*, that are mobile, the relation is given by:

$$N_i = Pc \tag{5.1}$$

Thus, we can obtain:

$$\sigma = q^2 c\mu = q^2 N_i \mu = q^2 Pc\mu \tag{5.2}$$

P values less than 1, indicate that some of the Li^+ ions lose their ability to move through the network. In the glass compositions $(50 - x)$ Li_2O: xMnO: $50P_2O_5$, the Q species of main network former is Q^2 i.e. $(PO_3)^-$. As discussed above, some of the Mn cations act in a network forming role and becomes the Q^4 manganate species i.e. $[MnO_2]^{2-}$ units. Since $[MnO_2]^{2-}$ has a greater nominal network charge than $(PO_3)^-$, it can trap Li^+ ions more easily, resulting in a reduction of effective carrier density N_i.

Thus, the conductivities of the studied glasses are dependent on three parameters:

1. The lithium ion concentration, *c*, as dictated by the stoichiometry.

2. The effective carrier density N_i.

3. The charge carrier mobility μ.

In summary, Mn plays a complicated role in the studied glass systems. As a network intermediate Mn^{2+} cations can act as both network modifier and former and significant concentrations of both types are present in these systems. While the conductivities of both systems are relatively low at room temperature, the $(60 - x)$ Li_2O: xMnO: $40P_2O_5$ system shows appreciable conductivity at 300 °C.

5.2 Future work

Further study of structures of the glass compositions is needed to determine the intermediate and long-range structures. For example, using the simulated structures as starting models the D(*r*) distributions can be fitted using Reverse Monte Carlo (RMC) methods. This would enable a more accurate description of the intermediate and long-range structure in these

systems, since this is a fitting method rather than a simulation method. The RMC results would make an interesting comparison with those from the MD simulation and could help to improve the MD methodology.

Armed with an accurate model describing the structure it will then be possible to monitor the lithium ion diffusion in these glasses through MD simulations at temperatures corresponding to the solid system. From these diffusion coefficients and activation energies can be calculated and compared to the experimental values.

The glasses described in the present system are being developed as possible cathodes for all glass solid state cells. Compositions in the $(60 - x)$ Li_2O: xMnO: $40P_2O_5$ system show reasonable Li^+ ion conductivities at 300 °C. While further optimisation of composition would be desirable with conductivity values in the order of 10^{-3} S cm^{-1} the system can now be investigated in a real device. This would first involve fusing the glass with a suitable electrolyte glass such as glasses in the system Li_2O-TiO_2-Al_2O_3-P_2O_5 [3] and cycling of the cell against a Li metal anode, to see if Li intercalation/deintercalation occurred at the cathode. A major remaining problem is the electronic conductivity of the glass. If this can be improved, for example by inclusion of carbon black in the melt, then the system could be quite effective. If so then an all solid cell involving both glass anodes and cathodes could be envisaged using a rocking chair type construction.

The Mn^{2+}/Mn^{3+} redox couple is one of many that could be suitable for the cathode of an all glass Li battery. Other transition metal couples, such as Fe^{2+}/Fe^{3+}, Ni^{2+}/Ni^{3+}, and Co^{2+}/Co^{3+} are also possible and might exhibit better performance when incorporated into a glass system. The present study represents one of the first steps in the development of all glass monolithic battery systems and there is a huge unexplored compositional space in which new high-performance materials could be developed.

5.3 References

1 Kontor, M. *Lithium ion conducting glass-based batteries* MSc thesis, Queen Mary University of London, (2004).

2 Hudgens, J. J. & Martin, S. W. Glass Transition and Infrared Spectra of Low-Alkali, Anhydrous Lithium Phosphate Glasses. *Journal of the American Ceramic Society* **76**, 1691-1696 (1993).

3 Abrahams, I. & Hadzifejzovic, E. Lithium ion Conductivity and thermal behaviour of glasses and crystallised glasses in the in the system Li_2O-TiO_2-Al_2O_3-P_2O_5. *Solid State Ionics* **134**, 249-257 (2000).